Structure, Mechanism and Regulation of Homocitrate Synthase

by

Stacie Lynne Bulfer

A dissertation submitted in partial fulfillment
Of the requirements for the degree of
Doctor of Philosophy
(Biological Chemistry)
in The University of Michigan
2010

Doctoral Committee:

Associate Professor Raymond C. Trievel, Chair
Professor David R. Engelke
Professor Janet L. Smith
Assistant Professor Daniel A. Bochar
Assistant Professor Gabrielle Rudenko

To Mom and Dad

ACKNOWLEDGEMENTS

I would like to first thank my advisor Ray Trievel. I wasn't sure what to expect when I first joined the lab, but am proud to be able to claim the distinction of being the first graduate student to come out of your lab. Your dedication and passion for science never ceases to amaze me. I have really appreciated all of your honest and useful advice throughout my graduate school career. You have made me the scientist that I am, and for that I am thankful.

I am also thankful for the members of the Trievel Lab, both past and present, who have made this a great place to work. Jeff, thank you for sharing your love of science and your wealth of advice. I greatly appreciate all of your work in getting my thesis project started. Evys, thank you for your patience and knowledge while training me as a naive rotation student, for always making the lab run smoothly and for the Indian lunch buffets. Patty, thank you for your friendship, enthusiasm for science, and for bubble tea runs. Thank you Paul for the great conversations both scientific and otherwise. Also thank you to Swathi and Scott and Roberta.

I would also like to thank my thesis committee members: Dan Bochar, Dave Engelke, Gabrielle Rudenko and Janet Smith. Your support and helpful advice over the years has been deeply appreciated. I would like to thank the Department of Biological Chemistry, particularly Beth Goodwin for all of her assistance. I would like to thank our collaborators Lorraine Pillus and Erin Scott for their contributions to this work. For providing assistance in the HTS studies, I would like to acknowledge the University of Michigan's Center for Chemical Genomics staff, specifically Tom McQuade, Martha Larsen and Paul Kirchoff.

I would like to thank the program director Joel Swanson, the program administrator Margaret Allan, and all of the other participants for making the Cellular Biotechnology Training Program what it is. Not only did this program fund my graduate school studies for 2.5 years, but it also provided me the opportunity to experience science

in a non-academic setting. Additionally I would like to thank Rackham Graduate School for funding through a Graduate Student Research Grant and a Predoctoral Fellowship Award.

Finally, I would like to thank my family and friends. I thank my parents for their love and support. Your sacrifices have meant so much to me, and I am truly grateful. I would also like to thank my sisters Emily and Heidi. It was great to have two fellow nerds to grow up with. I would like to thank my friends, whom have provided great reasons to take a break from lab. Last of all, Mike, thank you for being my best friend, for reminding me what is important and for supporting me throughout the process. I'm excited to see where life will take us next.

Publication note: Research described in Chapters 2 and 3 were originally published in The Journal of Biological Chemistry. Bulfer S.L., Scott E.M., Couture J-F, Pillus L., Trievel R.C. (2009) Crystal structure and functional analysis of homocitrate synthase, an essential enzyme in lysine biosynthesis. *J Biol Chem* 284 (51), 35769-80 and Bulfer, S.L., Scott, E.M., Pillus, L., Trievel, R.C. (2010) Structural Basis for L-Lysine Feedback Inhibition of Homocitrate Synthase. *J Biol Chem*. Epub *doi:10.1074/jbc.M109.094383*, respectively.

TABLE OF CONTENTS

LIST OF FIGURES

LIST OF TABLES

LIST OF SCHEMES

LIST OF APPENDICIES

LIST OF ABBREVIATIONS

2-OG, 2-oxoglutarate

2-OIV, 2-oxoisovalerate

AAA, α-aminoadipate

AAR, 2-aminoadipate reductase

AAT, 2-aminoadipate aminotransferase

AcCoA, acetyl-Coenzyme A

AEC, S-aminoethyl-L-cysteine

α-IPMS, α-isopropylmalate synthase

AMP, ampicillin

β-me, β-mercaptoethanol

CaHCS *Candida albicans* homocitrate synthase

CCG, Center for Chemical Genomics

CHLOR, chloramphenicol

CoA, coenzyme A

CPM, 7-diethylamino-3-(4-maleimidylphenyl)-4-methylcoumarin

CV, coefficient of variation

DAP, diaminopimelate

DMSO, dimethyl sulfoxide

EDTA, ethylenediaminetetraacetic acid

GFP, green fluorescent protein

GLV, glyoxylate

HABA hydroxy-azophenyl-benzoic acid

HAc, homoaniconitase

HIDH, homoisocitrate dehydrogenase

HCS, homocitrate synthase

HTS, high-throughput screening

IC50, apparent inhibitor constant

ICP-HRMS, inductively coupled plasma-high resolution mass spectroscopy

IMAC, immobilized metal affinity chromatography

IPTG, isopropyl β-D-1-thiogalactopyranoside

R.M.S.D., root mean square deviation

PcHCS, *Penicillium chrysogenum* homocitrate synthase

SAD, single wavelength anomalous dispersion

ScHCS, *Saccharomyces cerevisiae* homocitrate synthase

SDH, saccharopine dehydrogenase

SDS-PAGE, sodium dodecylsulfate polyacrylamide gel electrophoresis

SeMet, selenomethionyl

SLIM, site-directed, ligase-independent mutagenesis

SpHCS, *Schizosaccharomyces pombe* homocitrate synthase

SR, saccharopine reductase

TCEP, tris(2-carboxyethyl)phosphine

TEV, tobacco etch virus

Thiostar, 10-(2,5-dihydro-2, 5-di-oxo-1H-pyrrol-1-yl)-9-methoxy-3-oxo-, methyl ester 3*H*-naphthol(2,1-b) pyran-*S*-carboxylic acid

TtHCS, *Thermus thermophilus* homocitrate synthase

WT, wild type

Z´, Z-factor

ABSTRACT

The amino acid lysine is synthesized via two distinct pathways with the α-aminoadipate (AAA) pathway being utilized by fungi and certain archaebacteria. The first and committed step of this pathway is catalyzed by homocitrate synthase (HCS), which transfers an acetyl group from acetyl-Coenzyme A to 2-oxoglutarate (2-OG) to yield homocitrate and Coenzyme A. Additionally, HCS plays a role in the regulation of the AAA pathway, as it is feedback inhibited by the end product, L-lysine. Due to the absence of HCS in humans and its importance in the AAA pathway, this enzyme represents a potential target for small molecule inhibitors that may be used as broad-spectrum antifungal therapies to treat fungal infections, which occur frequently in immuno-compromised individuals. To better understand the mechanism of HCS, we determined the first crystal structure of a fungal HCS from *Schizosaccharomyces pombe*, along with two different structures of enzyme in complex with 2-OG. The structure reveals that 2-OG binds in the active site within the $(\alpha/\beta)_8$ TIM barrel domain via hydrogen bonds and coordination to the active site divalent metal ion. Steady state kinetic analysis and *in vivo* growth studies of mutations of residues involved in 2-OG binding or implicated in acid-base catalysis impair or abolish activity revealing the roles of these amino acids in substrate binding or the catalytic mechanism of HCS. Similar studies were completed to elucidate the mechanism of feedback regulation of HCS by L-lysine. The structure of an HCS/L-lysine complex illustrates that the inhibitor binds in the same binding site as the substrate 2-OG. *In vitro* and *in vivo* assays on mutants that interact with L-lysine impair feedback inhibition, as do previously identified substitutions of residues outside of the active site that render HCS insensitive to L-lysine. Finally, we utilized a high-throughput screening (HTS) approach to identify small molecule inhibitors of HCS. Collectively, these structural and functional studies elucidate the catalytic and regulatory mechanisms of HCS. Furthermore, they provide a framework for

discovery of inhibitors to HCS either through HTS or structure-based design, which may be developed into drugs to treat fungal infections.

CHAPTER 1
HOMOCITRATE SYNTHASE, AN ESSENTIAL ENZYME IN LYSINE BIOSYNTHESIS

Biosynthesis of L-Lysine

In complex eukaryotes, including mammals, lysine is an essential amino acid and must be obtained through dietary sources (1-3). However, many organisms including bacteria, fungi, and plants can synthesize L-lysine from metabolic precursors. Two diverse pathways have evolved for the biosynthesis of lysine in these organisms, which is unique to lysine among the common twenty amino acids. The diaminopimelate (DAP) pathway belongs to the aspartate family of amino acid biosynthesis and is utilized in most bacteria, some lower fungi (zygomycota) and green plants and (4-8). There are four variants of this pathway, with most bacteria utilizing the pathway involving succinyl intermediates (6, 9). In addition to producing lysine, the DAP pathway is also the source of meso-diminopimelic acid, an important component of peptidoglycan which makes up the bacterial cell wall (10). Higher fungi (ascomycetes and basidiomycetes), euglenoids and certain archaebacteria use the α-aminoadipate (AAA) pathway to synthesize lysine, which is a member of the glutamate family of amino acid biosynthesis (11-14). There are two variants of the AAA pathway with the second half of the pathway diverging in archaebacteria and fungi (15).

The AAA Pathway of Lysine Biosynthesis in Fungi

The AAA pathway has been identified in many fungal species including *Saccharomyces cerevisiae* (16), *Schizosaccharomyces pombe* (17), *Yarrowia* (formally *Saccharomycopsis*) *lipolytica* (18), *Neurospora crassa* (19), *Penicillium chrysogenum* (20), *Pichia guilliermondii* (21), *Candida maltosa* (22), and in the human pathogenic fungi *Candida albicans*, *Cryptococcus neoformans* and *Aspergillus fumigatus* (23). Biosynthesis of lysine via the AAA pathway in fungi consists of eight enzymatic steps

catalyzed by seven enzymes (Scheme 1.1) (14, 24). The first half of the AAA pathway, up to the generation α-aminoadipic acid, is similar to the tricarboxylic acid cycle,with the tricarboxylic acid cycle substrates being only one carbon shorter, and to the reactions involved in leucine biosynthesis (25). Studies in *S. cerevisiae* determined that synthesis of the intermediates in the first half of the AAA pathway is catalyzed in the mitochondria with the exception of homocitrate formation, which may take place in the nucleus (26, 27), whereas the second half of the pathway occurs in the cytoplasm (26).

Homocitrate synthase (HCS) catalyzes the first step in the AAA pathway by transferring an acetyl group from Acetyl-CoA (AcCoA) to 2-oxoglutarate (2-OG) to yield homocitrate and Coenzyme A (CoA) (Scheme 1.1). A two-step isomerization of homocitrate is then carried out by homoaniconitase (HAc) to form homoisocitrate via the intermediate cis-homoaconitate. Oxidation of homoisocitrate by homoisocitrate dehydrogenase (HIDH) yields the transient intermediate oxaloglutarate, which is then decarboxylated to produce 2-oxoadipate. Transamination of 2-oxoadipate by the pyridoxal 5'-phosphate-dependent 2-aminoadipate aminotransferase (AAT) using the amino donor L-glutamate generates 2-aminoadipate, which is subsequently reduced by 2-aminoadipate reductase (AAR) to form 2-aminoadipate semialdehyde in a reaction that requires both ATP and NADPH. Next, saccharopine reductase (SR) catalyzes the condensation of 2-aminoadipate semialdehyde with L-glutamate and the reduction of the imine by NADPH to generate saccharopine. Finally, oxidation and hydrolysis at the imine catalyzed by saccharopine dehydrogenase (SDH) generates the pathway's final products lysine and 2-OG (14, 24). Enzymes in the AAA pathway of lysine biosynthesis are important to study for several reasons. First, several pathway intermediates as well as lysine are used as precursors for other fungal metabolites (24). For example, in *P. chrysogenum*, α-aminoadipate is a precursor of the antibiotic penicillin (28). Additionally, the AAA pathway biosynthesis enzymes, particularly HCS because it catalyzes the initial step in the pathway, are important enzymes to study in part because they represent excellent targets for developing inhibitors that may act as anti-fungal therapeutics (29) (discussed below).

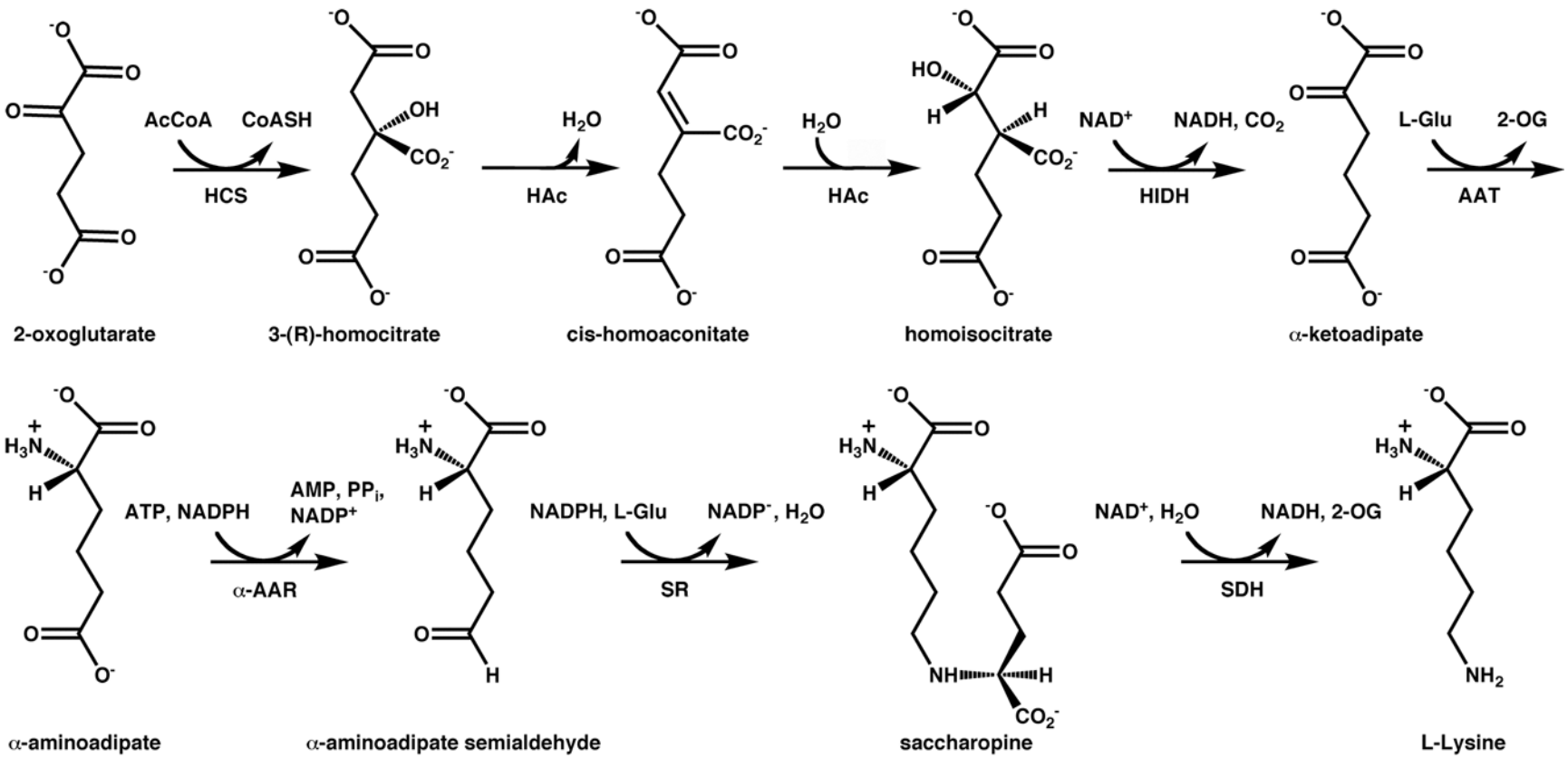

Scheme 1.1 The AAA pathway of lysine biosynthesis in fungi. The enzymes that catalyze the steps in the pathway are as follows. 1. Homocitrate synthase (HCS, EC 4.1.3.21). 2. Homoaconitase (HAc, EC 4.2.1.36). 3. Homoisocitrate dehydrogenase (HIDH, EC 1.1.1.87). 4. 2-aminoadipate aminotransferase (AAT, EC 2.6.1.39). 5. 2-aminoadipate reductase (AAR, EC 1.2.1.31). 6. Saccharopine reductase (SR, EC 1.5.1.10). 7. Saccharopine dehydrogenase (SDH, EC 1.5.1.7).

Regulation of the AAA pathway

The AAA lysine biosynthesis pathway is known to be highly regulated both at the levels of enzyme activity and gene expression. The most thoroughly studied example of regulation of enzyme activity in this pathway is the control of HCS through feedback inhibition by the end product L-lysine (discussed below). Additionally, the expression of many AAA pathway enzymes is controlled by two different mechanisms. In *S. cerevisiae*, several amino acid biosynthesis pathways, including the pathway for lysine biosynthesis, are regulated by the general control of amino acid biosynthesis. This mechanism functions by depressing the transcription of enzymes in several amino acid biosynthesis pathways when the organism is starved for one of several amino acids (30, 31). Experiments using leaky auxotrophic mutations grown on minimal media identified HCS, along with enzymes in the second half of the AAA pathway (AAR, SR and SD) (Scheme 1.1), as being governed by the general control mechanism (32). Although this mechanism has been most extensively studied in *S. cerevisiae*, it is also known to occur in the AAA pathway-utilizing fungus *Neurospora crassa* (33). In *S. cerevisiae,* the transcription of most of the AAA pathway enzymes, with the exception of HIDH and SDH, is also specifically regulated by the transcriptional factor Lys14p in the presence of the pathway intermediate 2-aminoadipate semialdehyde (34-36). Lys14p was identified as nuclear protein that contains a $Zn(II)_2Cys_6$ cluster DNA binding domain. This domain functions to up-regulate transcription by binding to a nonameric core motif that is present in the promoter region of the lysine biosynthesis genes, with the exception of HIDH and AAT (35-37). Once Lys14p is bound to the promoter, it is believed to be activated by the co-inducer 2-aminoadipate semialdehyde to induce gene expression (36).

In addition to general and specific control of gene expression of the enzymes in the AAA pathway, transcription of these genes also appears to be influenced by the end product of the pathway, L-lysine. Six of the seven *S. cerevisiae* AAA pathway enzymes, including HCS are susceptible to repression when grown in media supplemented with excess lysine (38). However, L-lysine regulation of the five enzymes downstream of HCS has been attributed to L-lysine feedback inhibition of HCS. Inhibition of HCS activity causes a reduced metabolic flux through the pathway, resulting in a diminished production of 2-aminoadipate semialdehyde and inactivation of the transcriptional factor

Lys14p (35, 36). These findings implicate feedback inhibition of HCS activity to be vital in the control of lysine biosynthesis at both the levels of HCS enzymatic activity and gene expression.

Homocitrate Synthase

HCS has been characterized both genetically and biochemically in *S. cerevisiae*, which contains two isozymes of this enzyme: Lys20 and Lys21 (11, 14, 24). Biochemical studies of HCS from the fungal species *P. chrysogenum* (39, 40) *P. guilliermondii* (21), *Y. lipolytica* (18) *C. maltosa* (22), and from the archaebacteria *Thermus thermophilus* have also been published (15). The protein sequence among fungal HCS is highly homologous with many fungal species having 70-91 % identity and *T. thermophilus* HCS sharing 54 % identity to *S. cerevisiae* HCS (ScHCS) Lys20 (Figure 1.1) (14, 15). Although the high sequence homology among HCS suggests that they function with a similar catalytic mechanism, HCSs also appear to have properties contingent on the species.

Different subcellular localization of HCS in fungal species has been reported and may be species dependent. Early cell fractionation studies demonstrated ScHCS activity to be mostly localized in the mitochondria (41). Because most proteins located in the mitochondria of *S. cerevisiae* contain a localization signal that ScHCS Lys20 lacks, it was later suggested that 70% of HCS activity is cytosolic with ScHCS Lys20 and Lys21 being localized to the cytosol and mitochondria, respectively (42). More recent studies using monoclonal antibodies and immunofluroescence demonstrate that ScHCSs Lys20 and Lys21 are mostly localized to the nucleus, with studies utilizing green fluorescent protein (GFP) fusions of ScHCS Lys20 and Lys21 proteins confirming a nuclear localization (27, 43). The localization of HCS from *S. pombe* (SpHCS) (encoded by the *lys4*$^{+}$ gene) was also examined using SpHCS-GFP fusions and immunoblotting (44). SpHCS-GFP fusions were dispersed throughout the cell, whereas SpHCS was found to have a non-cytosolic localization when detected by immunoblotting. The GFP fusion protein may disturb the subcellular localization of SpHCS resulting in conflicting localization patterns between the two techniques. Further studies to determine the exact localization of SpHCS are still required. In contrast, subcellular fractionation experiments

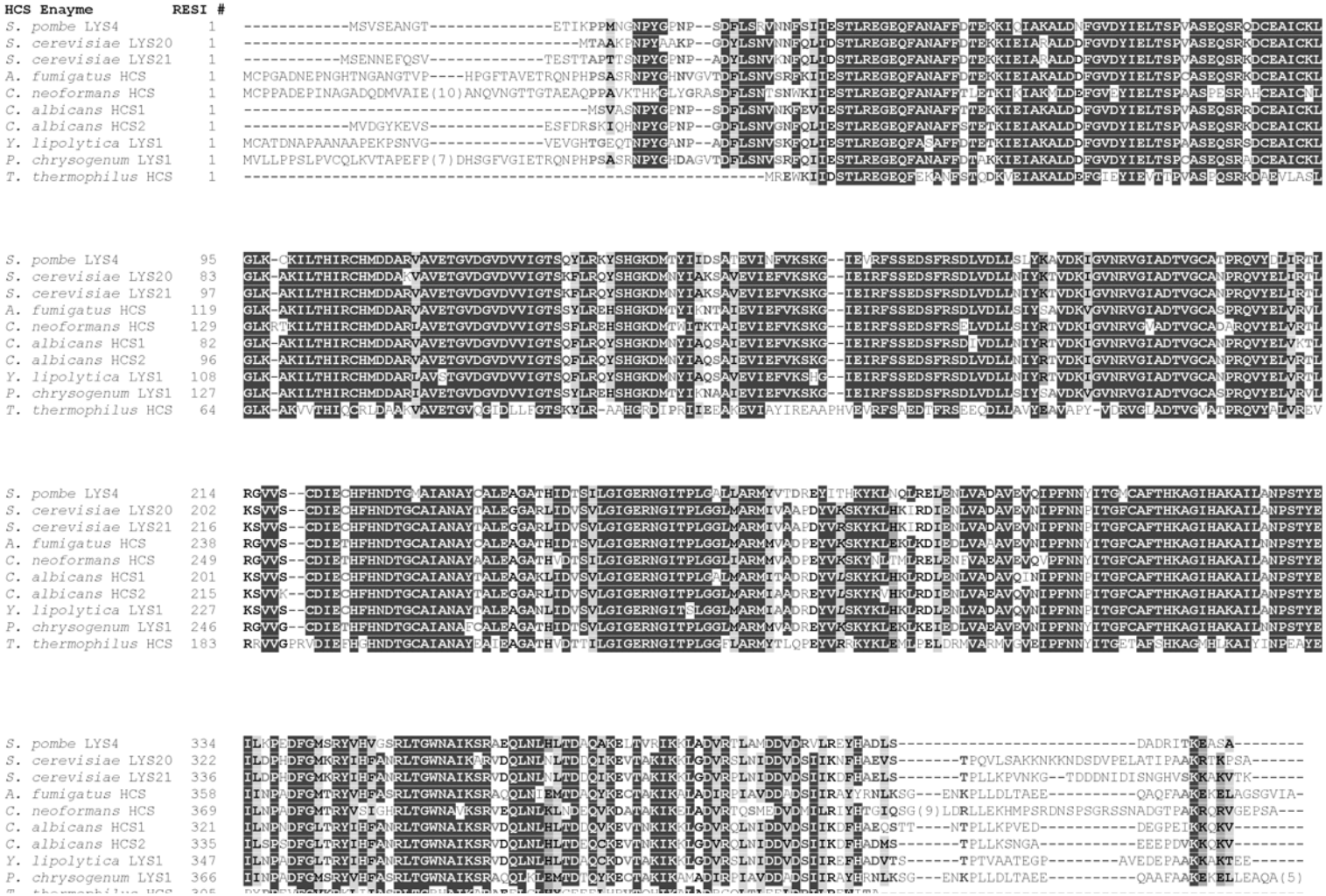

Figure 1.1 Protein sequence alignment of HCS enzymes. Sequences are from various fungi and the archaebacteria *T. thermophilus.*

on *P. chrysogenum* HCS (PcHCS) (encoded by the *Lys1* gene) show 75 % of activity to be localized in the cytosol with the remaining activity present in the mitochondria (40). Studies using a GFP fusion of PcHCS confirm a mostly cytosolic localization of the enzyme (39). The cytosolic location of PcHCS my be due to its role in penicillinbiosynthesis. The nuclear/non-cytosolic localization ScHCS and SpHCS raises the question of whether these enzymes may have a nuclear/non-cytosolic function in addition to lysine synthesis.

The oligomerization of HCS may also vary depending on the species. HCS was originally believed to function as a monomer in *T. thermophilus* (15), but recently released structures of the enzyme reveals that it functions as a homodimer (45). PcHCS also functions and as a multi-subunit enzyme, most likely a dimer or trimer (40). Although the native subunit composition of ScHCS Lys20 has yet to be determined, recombinant ScHCS Lys20 exists as a monomer, dimer, tetramer and higher weight aggregates with most of the activity being associated with the lower molecular weight species (46). A more complex subunit composition of HCS may have evolved to regulate enzymatic activity and thus the metabolic flux through the biosynthetic pathway.

Although HCS has generally been studied as an enzyme in the AAA lysine biosynthesis pathway, it also plays an important biological role in organisms that do not utilize this pathway. Diazotrophic bacteria, including the species *Azotobacter vinelandii* HCS (encoded by the *NifV* gene), produce homocitrate as a constituent of the iron-molybdenum (FeMo) cofactor in nitrogenase, which is used for nitrogen fixation (47, 48). Additionally, a recent study identified HCS (*FEN1* gene) in the legume *Lotus japonicus*, which has a symbiotic relationship with rhizobic soil bacteria that lack a HCS gene (49). Homocitrate generated by the plant *FEN1* gene is subsequently used by the soil bacteria to generate nitrogen used by both organisms providing a molecular explanation for the necessity of this symbiotic partnership. In summary, the diversity in biological functions of HCS compels further characterization of this enzyme in both fungal and non-fungal species.

Activity and Kinetic Mechanism of HCS

The activity of HCS purified from cell extracts has been measured from *Y. lipolytica* (18), *P. guillermondii* (21), *C. maltosa* (22) and *P. chrysogenum* (40), whereas more recent activity studies have been performed on recombinantly purified HCS from *S. cerevisiae* (50), *T. thermophilus* (15) and *A. vinelandii* (47). The large differences in the steady state kinetic parameters these HCS enzymes (Table 1.1) may be do to a variety of reasons, including how the enzyme was purified and the type of assay used. However, the most recent analysis of the activities of recombinant *T. thermophilus* HCS (TtHCS) and ScHCS Lys20 resulted in similar kinetic values (k_{cat} = 63-92 min^{-1}, $K_{M(2\text{-}OG)}$ = 0.044-0.140 mM and $K_{M(AcCoA)}$ = 32-42 μM) and may represent more accurate measurements of HCS activity.

In addition to determining the activity of HCS from several species, the kinetic mechanism of HCS was also investigated. This mechanism was first studied in *Y. lipolytica* (18). A double reciprocal plot of velocity versus 2-OG concentration at various fixed values of AcCoA resulted in intersecting lines suggesting HCS follows a sequential mechanism. Limited product inhibition studies were also performed on *Y. lipolytica* HCS using the inhibitor CoA. CoA did not affect the initial velocities at various fixed 2-OG concentrations, but was found to be a strong competitive inhibitor of AcCoA, although it does not obey Michaelis-Menten kinetics. Together these results suggest that the binding of substrates is ordered with 2-OG binding before AcCoA. More resent studies of ScHCS Lys20, confirm an ordered sequential mechanism for HCS. Additionally, results from more extensive product and dead-end inhibition studies show that HCS obeys a Bi-Bi sequential mechanism with 2-OG binding before AcCoA followed by the ordered release of CoA before homocitrate with the hydrolysis of the homocitryl-CoA intermediate being essentially irreversible (51) (Scheme 1.2).

Enzymes that Catalyze Claisen Condensation Reactions

The mechanism of HCS has been proposed to obey a mixed Claisen condensation reaction (14). In this type of mechanism, there is a base-catalyzed abstraction of a carbon α-proton from a ketone or aldehyde to form an enol (or enolate). Next, the carbonyl carbon of the second substrate is nucleophilically attacked by the enolate ion to form a β-

Table 1.1 Steady state kinetic parameters for HCS from different species.

Species	K_M 2-OG (mM)	K_M AcCoA (μM)	k_{cat} (min^{-1})
P. chrysogenum	2.2	sigmoidal	N.R.
Y. lipolytica	1.7	sigmoidal	N.R.
C. maltosa	0.03	33	N.R.
P. guillermondii	0.02	6	N.R.
A. vinelandii	2.2	60	N.R.
T. thermophilus	0.05	32	92
S. cerevisiae Lys20	0.14	42	63

N.R. not reported.

.

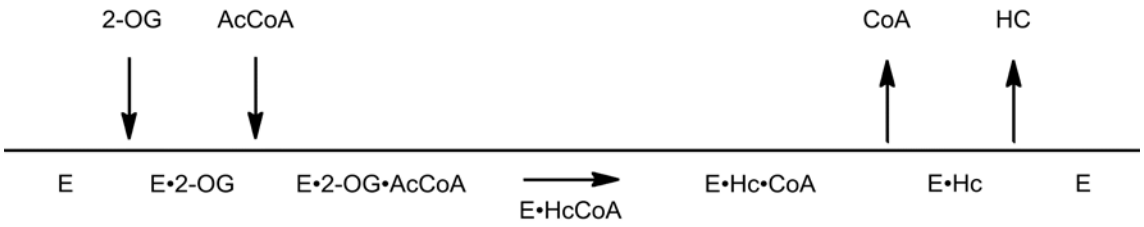

Scheme 1.2. Kinetic mechanism of HCS.

hydroxy ester (Scheme 1.3) (52). Although this mechanism is reversible, many enzymes that proceed via this mechanism, including, HCS (53), α-isopropylmalate synthase (α-IPMS) (54, 55), malate synthase (56, 57), and citrate synthase (58, 59), catalyze the irreversible hydrolysis of the resulting β-hydroxy ester to produce the final reaction product. These enzymes catalyze similar reactions using AcCoA as the acetyl donor (Scheme 1.4), however the structures and details of their mechanism are quite different.

Of the enzymes mentioned above, citrate synthase is the most extensively studied and catalyzes the condensation of oxaloacetate and AcCoA to form citrate and CoA as the first step in the tricarboxylic acid cycle (Scheme 1.4A). Citrate synthase forms a dimer with each monomer consisting of 20 α-helices and one small β-sheet. Each monomer is composed of a large domain and a small domain, with the active site located in the cleft between the two domains (Figure 1.2A). In addition, citrate synthase is known to adopt two different conformations, a closed form and an open form. The closed form appears to be the active form of the enzyme and possesses binding sites for both the oxaloacetate and AcCoA substrates (59). The active site of citrate synthase is mostly polar with the substrate oxaloacetate forming hydrogen bonds or salt bridge interactions to three arginines and two histidines (Figure 1.2B) (60). Based on several binary and ternary structures of citrate synthase from *Escherichia coli*, the first step of the reaction has been proposed to occur via a general acid–base catalyzed step to abstract a proton from the methyl group of AcCoA. An aspartate residue (Asp375) is thought to function as the catalytic base in deprotonation of the methyl group of AcCoA while a histidine residue (His274) simultaneously protonates the carbonyl oxygen of the acetyl group to form a neutral enol intermediate. The enol intermediate then nucleophilically attacks the oxaloacetate to form an alkoxide intermediate that is then protonated by His320, which acts as a catalytic acid to form citryl-CoA. Finally, the resulting citryl-CoA is hydrolyzed to form citrate and CoA (58, 59).

Malate synthase catalyzes the condensation and hydrolysis of glyoxylate and AcCoA to form malate and CoA in the glyoxylate pathway (Scheme 1.4B). Although the reaction mechanism of malate synthase is analogous to citrate synthase, the structures and details of the mechanism of these two enzymes differ substantially. The structure of *E.*

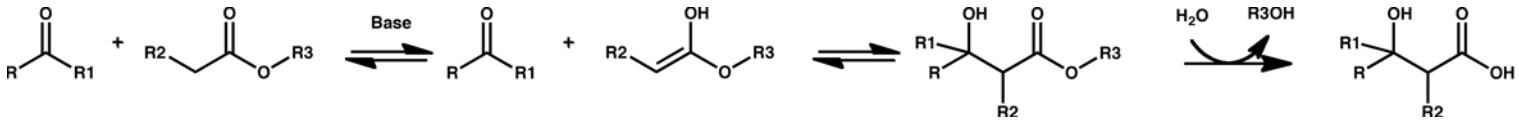

Scheme 1.3 General mechanism for a mixed Claisen condensation reaction and subsequent hydrolysis.

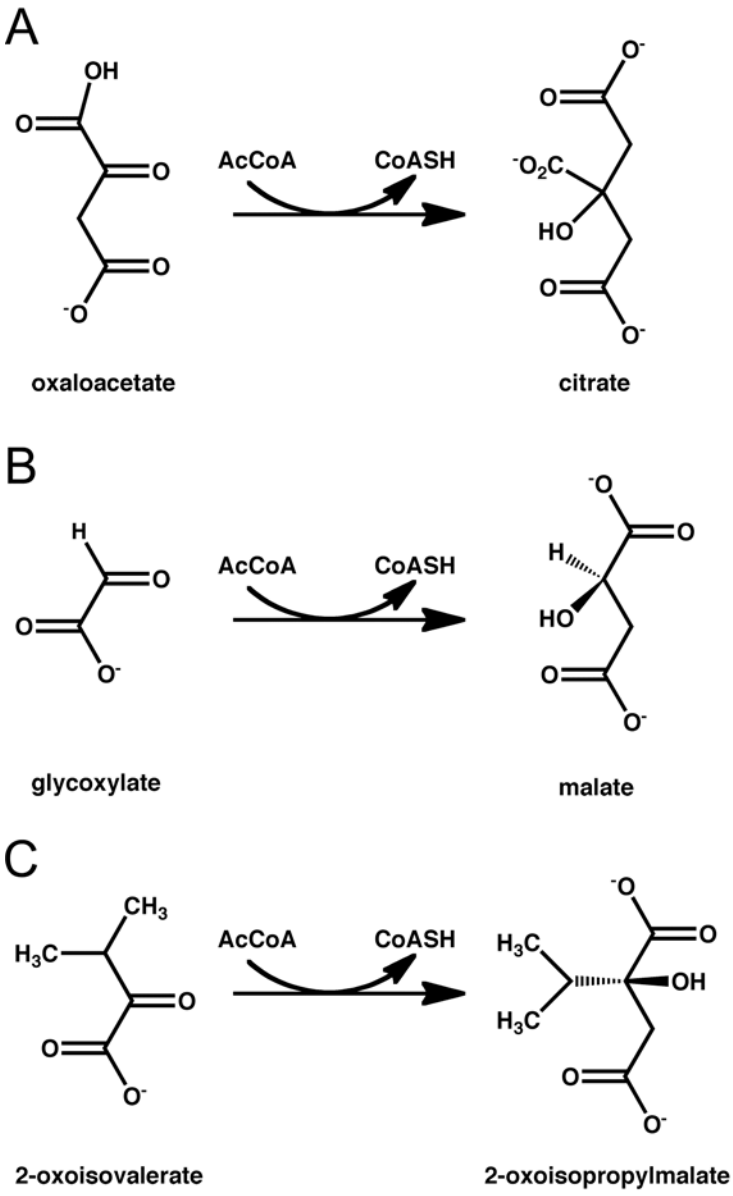

Scheme 1.4 Claisen condensation reactions utilizing AcCoA as the carboxymethyl donor. (A) Reaction catalyzed by citrate synthase. **(B)** Reaction catalyzed by malate synthase. **(C)** Reaction catalyzed by α-IPMS.

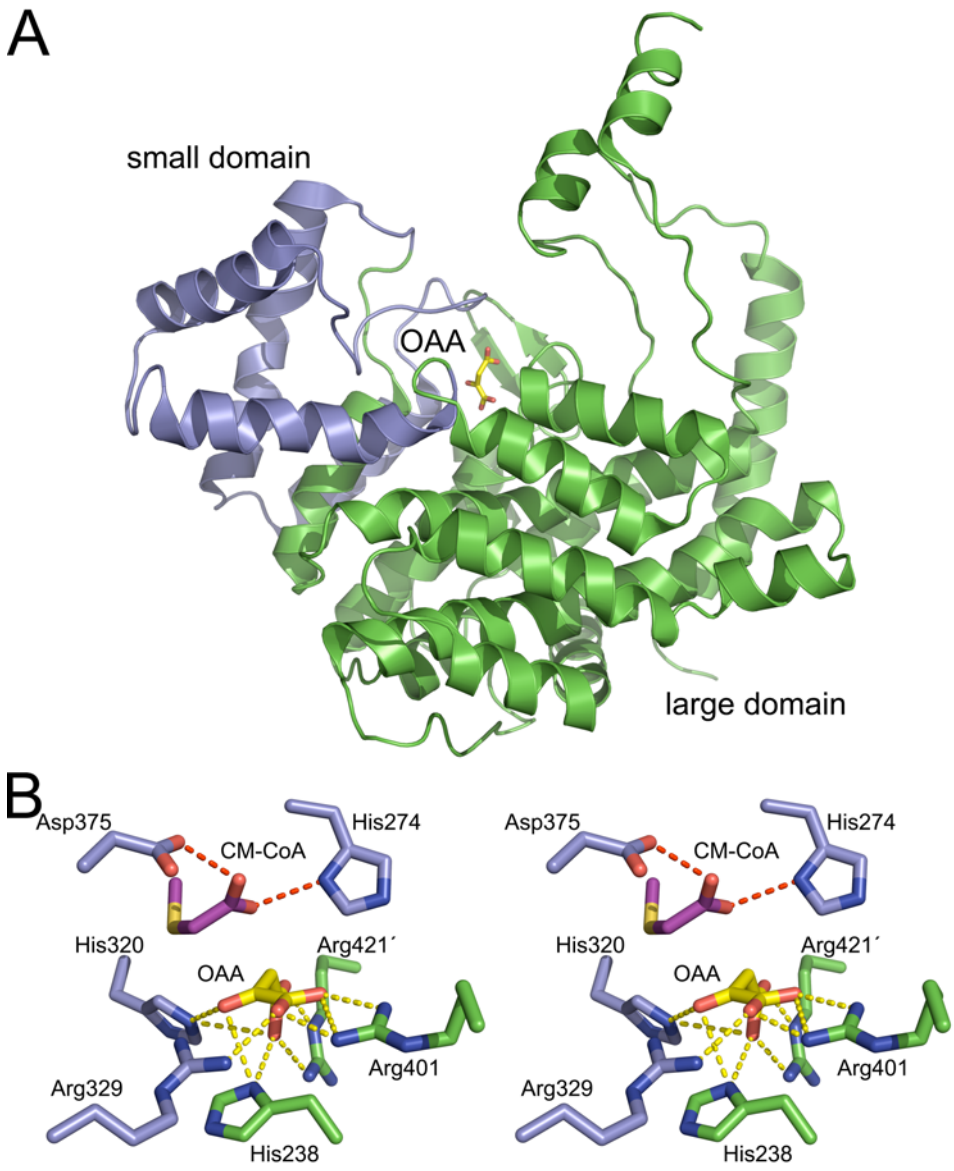

Figure 1.2 Overall structure and active site of *Escherichia coli* citrate synthase. (A) Ribbon diagram of a monomer of citrate synthase (PDB 5CTS) (58) showing the large domain (green) and small domain (blue). Oxaloacetate (OAA) is rendered as sticks with yellow carbons. **(B)** Stereoview of the active site citrate synthase in a ternary complex with oxaloacetate and carboxymethyl-CoA (CM-CoA) (PDB 5CTS) (58). Oxaloacetate along with residues in the large and small domain are colored as described in **A** with Arg421′ belonging to the neighboring monomer. Only the carboxymethyl tail of CM-CoA (purple) is shown for clarity. Hydrogen and salt bridge interactions of active site residues to oxaloacetate (yellow) and hydrogen bonds to carboxylate of CM-CoA (red) are depicted as dashes.

coli malate synthase isoform G in complex with glyoxylate reveals the enzyme functions as a Mg(II)-dependent monomer, with a centrally located $(\alpha/\beta)_8$ TIM barrel fold. An N-terminal α-helical domain flanks the one side of the barrel, while an inserted β–sheet domain folds against the other side of the barrel. Additionally there is an α-helical C-terminal domain, which forms a plug over C-terminal side of the TIM barrel (Figure 1.3A). The active site is sandwiched in a cleft between the C-terminal end of the TIM barrel and the C-terminal plug. The substrate glyoxylate binds within appropriate distancebarrel and the C-terminal plug. The substrate glyoxylate binds within appropriate distance to the proposed catalytic base Asp631 and is stabilized through coordinating to the magnesium ion and hydrogen bonding to the backbone amides of Phe353 and Leu454. The aldehyde oxygen of glyoxylate also forms a hydrogen bond to the guanidinium group of Arg338, which is proposed to partner with Asp631 in the enolization of AcCoA, analogous to Asp375 and His274 in citrate synthase (Figure 1.3B) (57). A ternary complex of malate synthase and mutagenesis studies helped to elucidate the details of the mechanism of malate synthase. Although Asp361 in malate synthase is essential, a R388K mutation is still active suggesting that it does not participate in proton transfer to the carbonyl oxygen of AcCoA (analogous to His274 in citrate synthase) or to the alkoxide intermediate (His320 fulfills this role in citrate synthase). Hence, the alkoxide intermediate may remain deprotonated during the subsequent catalytic steps (56).

Like malate synthase, α-IPMS is also a metal dependent $(\alpha/\beta)_8$ TIM barrel enzyme and catalyzes the transfer of the acetyl group of AcCoA to 2-oxoisovalerate (2-OIV) to form α-isopropylmalate and CoA (Scheme 1.4C). α-IPMS shares 39% sequence homology with HCS and has been used as a model to provide insights into the mechanism and catalytic residues of HCS in lieu of an HCS structure (50). The crystal structure of *Mycobacterium tuberculosis* α-IPMS shows that the enzyme exists as a domain swapped homodimer with each monomer of consisting of three major domains (55) (Figure 1.4A). The N-terminal domain contains an $(\alpha/\beta)_8$ TIM barrel catalytic domain with the active site of the enzyme located at the C-terminal end of the TIM barrel. The C-terminal domain is a regulatory domain consisting of a novel two-unit βββα fold that binds the feedback inhibitor L-leucine. A linker region connects the N-

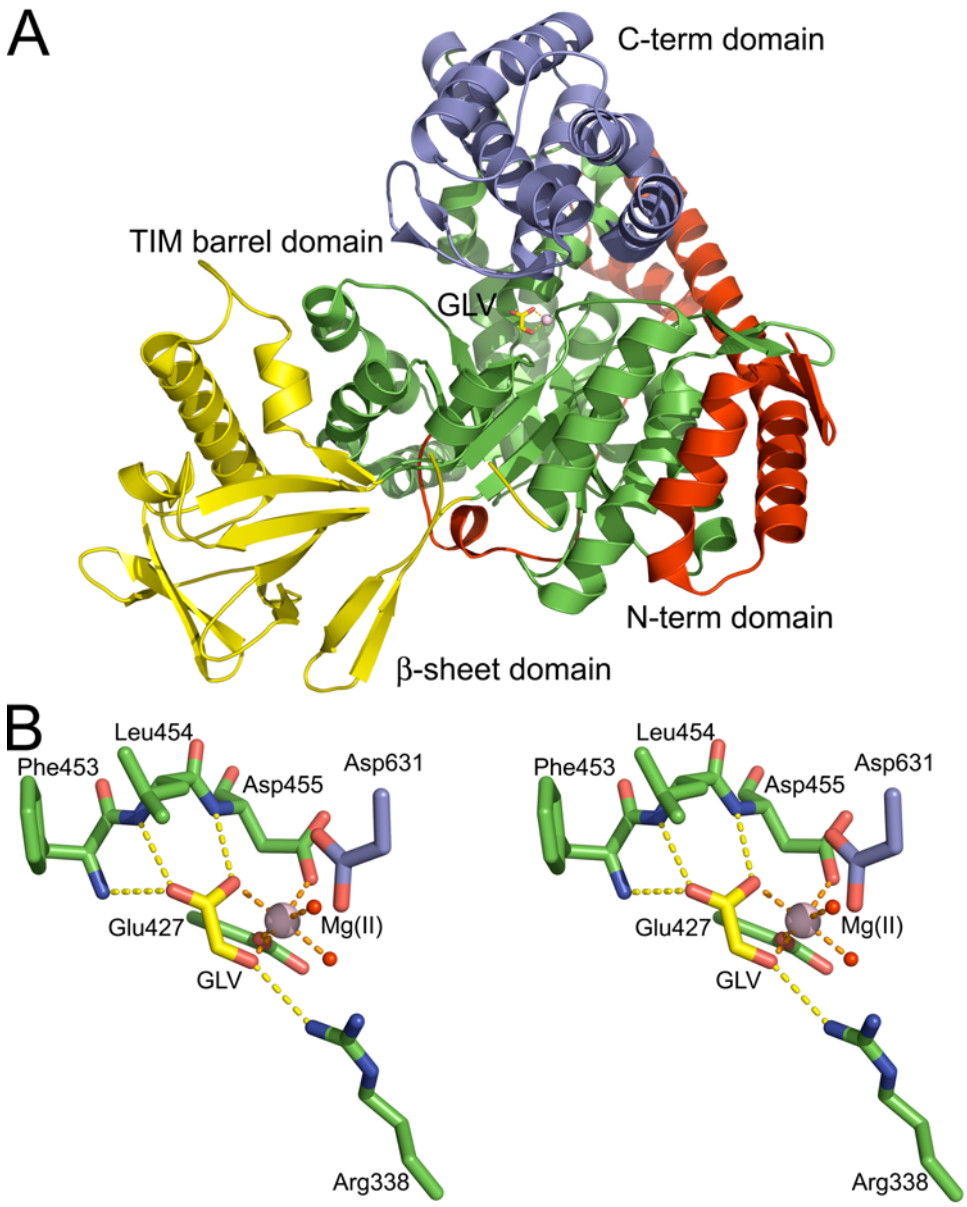

Figure 1.3 Overall structure and active site of *Escherichia coli* malate synthase. (A) Ribbon diagram of malate synthase (PDB 1D8C) (57) showing the N-terminal domain (red), TIM barrel domain (green), β-sheet domain (yellow) and C-terminal domain (blue). Glyoxylate (GLV) is rendered as sticks with yellow carbons and the Mg(II) ion is depicted as a pink sphere. **(B)** Stereoview of the active site of malate synthase in a binary complex with glyoxylate (PDB 1D8C) (57). Glyoxylate, Mg(II) and residues in the active site are colored as described in panel **A.** Orange and yellow dashes represent coordination to the Mg(II) ion and to glyoxylate, respectively.

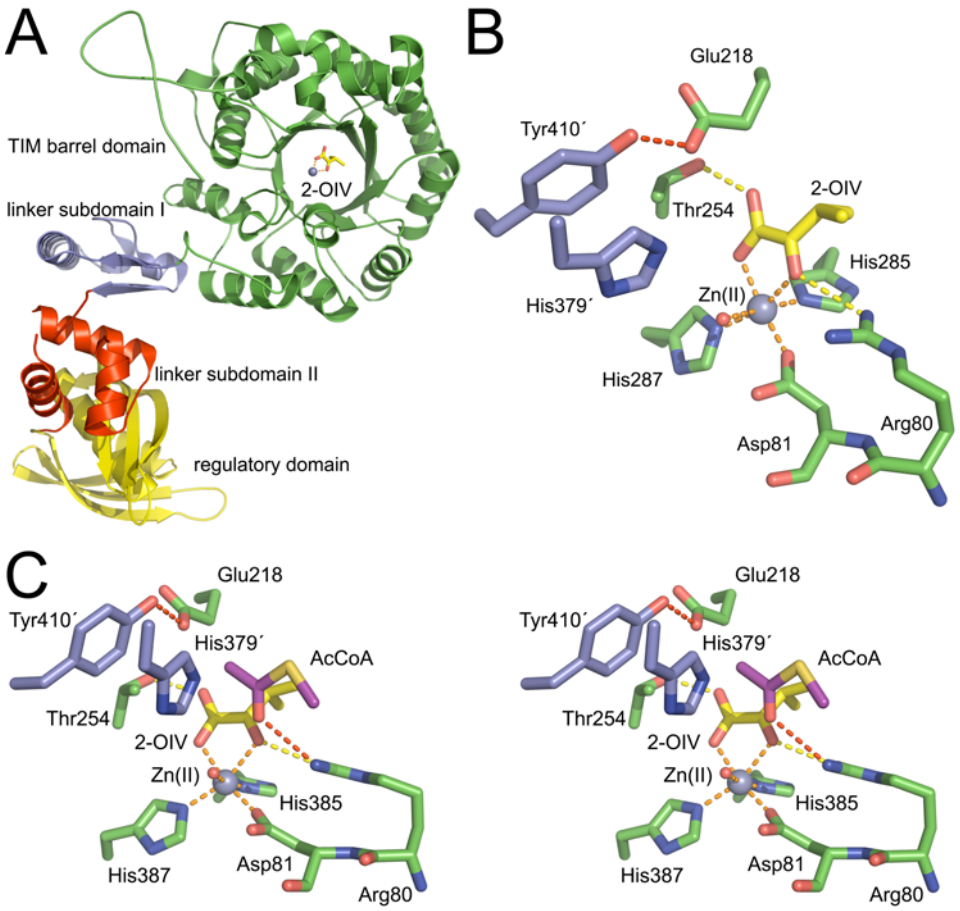

Figure 1.4 Overall structure and active site of *Mycobacterium tuberculosis* α-isopropylmalate synthase (A) Ribbon diagram of a monomer of α-IPMS (PDB 1SR9) (55) depicting the N-terminal TIM barrel domain (green), regulatory domain (yellow) along with subdomain I (blue) and subdomain II (red) of the linker domain. 2-OIV is rendered as sticks with yellow carbons and the Zn(II) metal ion is depicted as a gray sphere. **(B)** Active site of α-IPMS in a binary complex with 2-OIV (PDB 1SR9) (55). The 2-OIV substrate along with the active site residues are colored as described in panel A. Orange, yellow and red dashes represent coordination to the Mg(II) ion, hydrogen bonding to2-OIV, and hydrogen bonding between predicted active site residues, respectively. **(C)** Stereoview of a modeled ternary complex of α-IPMS. The molecule is colored as described in panel A with only the acetyl thioester group of AcCoA (purple) shown for clarity.

terminal catalytic domain to the C-terminal regulatory domain. Subdomain I of the linker domain is composed of an α-helix and two short β-strands, while subdomain II consists of a three-helix bundle. The two subdomains are separated by a disordered hinge region, which allows the two monomers to have different relative orientations in their N- and C-terminal domains.

The active site of α-IPMS located at the interior of C-terminal end of the $(\alpha/\beta)_8$ TIM barrel that consists of a divalent metal cation, Zn(II) in this structure, which has octahedral coordination to three protein ligands: Asp81, His285 and His 287, the C1 and 2-oxo oxygens of the substrate 2-OIV and to a water molecule. 2-IOV is bound within the center of the TIM barrel through hydrogen bond interactions with Thr254 and Arg80 (Figure 1.4B). A ternary complex with 2-OIV and the product CoA could not be solved, so the authors chose to model an AcCoA into the active site. The methyl carbon of the thioacetyl group of AcCoA was modeled to fit between His379′ (the prime (′) denotes the residue is in the neighboring monomer), Glu218 and the C2 carbon of 2-OIV with the carbonyl oxygen forming a hydrogen bond to the guanidinium group of Arg80. Based on the structure of the modeled α-IPMS/2-OIV/AcCoA ternary complex, the authors propose a Claisen condensation reaction mechanism with the conserved Glu218 and His379′ residues in positions to act as the potential bases. Tyr410′ may also be important in base catalysis as it forms a hydrogen bond with Glu218 and also orients His379′ by stacking on top of it (55) (Figure 1.4C). Surprisingly, recent kinetic studies on α-IPMS with mutations at each of these residues, (E218A, H379A or Y410F) did not significantly affect the kinetic parameters of the enzyme suggesting that none of these residues are critical for activity (61). Further studies are needed to determine which residues in α-IPMS are necessary for catalysis.

The Catalytic Mechanism of HCS

Unlike citrate synthase, malate synthase and α-IPMS, a structure of HCS has not been solved prior to this work, and a model for the catalytic mechanism of this enzyme was based on biochemical studies (53). Inductively coupled plasma-high resolution mass spectrometry (ICP-HRMS) analysis of metal affinity purified ScHCS Lys20 reveals the enzyme to most like be a Zn(II) dependent metalloenzyme. Further experiments

examining pH dependence of the kinetic parameters, isotope effects and dissociation constants for competitive inhibitors provide even more insights into the mechanism of HCS. By plotting the log of velocity (*V*) versus pH at saturating concentration of substrates one can determine residues involved in catalysis, whereas plotting the log V/K_M versus pH at sub-saturating levels of one of the substrates gives insights into substrate binding and catalysis. The log *V* versus pH-rate profile of ScHCS Lys20 has slopes of 1 and -1 indicating that one protonated residues and one unprotonated residue are required for catalysis. The unprotonated residue had a p*K* of 6.7 and most like functions as a general base to abstract a proton from AcCoA, while the protonated residue had a p*K* of 8.0, and may be the general acid that donates a proton to form homocitryl-CoA. The log $V/K_{M(2\text{-}OG)}$ versus pH rate profile indicates two protonated residues and one unprotonated residues are important for 2-OG binding and/or catalysis. One of the protonated residues is potentially the hydrogen bond donor to the 2-oxo group of 2-OG and donates a proton during catalysis, and the other protonated residue may form a hydrogen bond with the C5-carboxylate of 2-OG. However, the role of the unprotonated group in 2-OG binding remains unknown. Analysis of the log $V/K_{M(AcCoA)}$ versus pH rate profile shows that two protonated and two unprotonated groups are important for AcCoA binding and/or catalysis. Two of these residues are important for catalysis as described for the log *V* pH-rate profile, while the other two groups are probably important for AcCoA binding. Additionally, no solvent isotope effect is observed, suggesting that the alkoxide remains metal-bound, and subsequently receives a proton form the residue acting as the general acid.

Based on these results, a general acid-base mixed Claisen condensation mechanism was proposed for HCS (53) (Scheme 1.5). In this mechanism, 2-OG binds first coordinating to an active site metal ion with its C1-carboxlate and 2-oxo atoms, while the C5 carbon is stabilized through hydrogen bonding to a protonated residue. AcCoA then binds in a position with its thioester group near the C2 carbon of 2-OG and the residue that acts as the general base. The general base abstracts a proton from the methyl group of AcCoA to generate an enol/enolate, which subsequently attacks the C2 carbon of 2-OG to form the alkoxide of homocitryl-CoA. The alkoxide accepts a proton

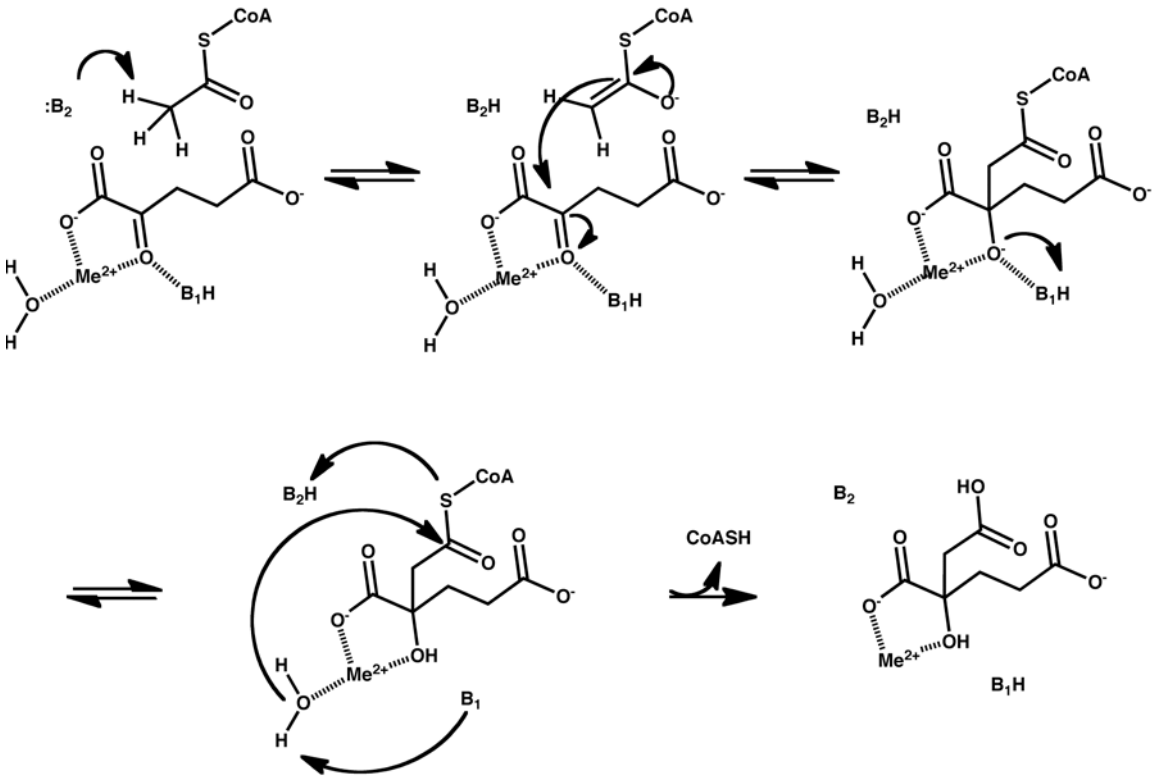

Scheme 1.5 Catalytic mechanism of HCS proposed by Qian *et al.*

from the general acid to form homocitryl-CoA, and subsequent hydrolysis by the metal-bound water yields the products CoA and homocitrate.

The Catalytic Base in HCS

Since HCS shares a moderate degree of sequence homology with α-IPMS, mutagenesis and kinetic studies on several conserved residues within the active site of these two enzymes were probed for their role in HCS catalysis (50). Alanine and conservative mutations of ScHCS Lys20 residues Glu155, His309 and Tyr320 (corresponding to Glu218, His379, and Tyr410 in α-IPMS) (Figure 1.4B) were prepared and tested for activity. No detectable activity was observed for H309A and H309N mutations, and the E155A and E155Q mutations resulted in >1000 fold reduction in activity compared to WT ScHCS Lys20. The presence of imidazole in the H309A mutant and formate in the E155A assays increased the activity slightly for these two mutations, suggesting the side chains of these residues are important in catalysis. In contrast, an Y320F mutation was active, but had a 25-fold decrease in activity compared to WT enzyme suggesting that although it is not important for catalysis, it might aid in substrate binding and orientation. Based on these findings, a His309-Glu155 catalytic dyad was proposed to act as the general base in HCS. However, without an HCS tertiary structure, assignment of the residues involved in acid-base catalysis remains speculative.

Role of the Divalent Metal Ion in Catalysis by HCS

Only a few studies have to the identity of the divalent metal specificity of HCS, an essential component needed for activity, have been performed. Although the divalent metal in the active site of metal affinity purified ScHCS Lys20 HCS was found to most likely be Zn(II) (53), these results may be inaccurate simply due to the fact that the enzyme was purified on a divalent metal affinity column (46). Additionally, purified ScHCS Lys20 that is inactivated with the metal chelator ethylenediaminetetraacetic acid (EDTA) can be reactivated with the addition of either Mn(II) or Zn(II) (53). Recently, the metal dependence of TtHCS was also investigated by adding different divalent metal ions to EDTA treated enzyme and assaying for activity (45). The addition of Mg(II), Mn(II) and Co(II) resulted in the highest activity suggesting to the authors that Mg(II) or Mn(II)

may be the biologically relevant divalent cation. Together, these results raise questions about the identity of the physiologically relevant metal in HCS, and if the enzyme is regulated through a metal switching mechanism similar to the metalloenzymes histone deacetylase HDAC8 (62) and the *E. coli* deacetylase LpxC (63). Studies described in Appendix A begin to characterize SpHCS reconstituted with different divalent metals in an effort to resolve these types of questions.

Regulation of HCS activity by L-Lysine Feedback Inhibition

The activity of many enzymes that function in amino acid biosynthesis pathways are regulated by feedback inhibition by the end product or by an intermediate in the pathway. The least complex form of feedback inhibition is considered to be the inhibition of the first enzyme in the pathway by the final amino acid product (64, 65). This form of inhibition is observed for the AAA pathway of lysine biosynthesis in *S. cerevisiae* (66), *P. chrysogenum* (67), *Y. lipolytica* (18), and *T. thermophilus* (15). However, it cannot be ruled out that another step in the pathway is also regulated by the end product L-lysine. Overexpression of HCS in a *P. chrysogenum* strain with an inactive AAR gene did not lead to an overproduction of the AAR substrate α-aminoadipate, suggesting there may be another rate-limiting step in this pathway in *P. chrysogenum*.

Studies investigating the nature of L-lysine feedback regulation of HCS provide evidence for two distinct models of inhibition. In the first model, L-lysine binds competitively with the substrate 2-OG in the active site of HCS, despite the lack of structural homology between L-lysine and 2-OG. This model is supported by kinetic studies in HCS from *P. chrysogenum* (40), *T. thermophilus* (15) and *S. cerevisiae* (68) which demonstrate that L-lysine inhibition is competitive with 2-OG. The second model of feedback inhibition of HCS is an allosteric model where L-lysine binds in binding pocket that is distinct from the active site of the enzyme. Evidence for this model includes lysine inhibition studies versus the substrate 2-OG in HCS from *Y. lipolytica* (18). In this species, the inhibition kinetics exhibit non-Michealis-Menten kinetics, suggesting an allosteric binding site for L-lysine. Additional evidence that inhibition of HCS by L-lysine, comes from studies that isolated HCS lysine overproducing mutants in *S. cerevisiae* (36, 68). Three lysine insensitive point mutants (R276K and S385F in

isozyme Lys20 and Q366R in isozyme Lys21) were found to be resistant to S-aminoethyl-L-cysteine (AEC), a toxic L-lysine analog. These mutations display a large increase in the apparent inhibitor constant (IC50) values compared to WT enzyme, yet still maintain HCS activity suggesting 2-OG and lysine do not bind in the same site. Determining a structure of an HCS/L-lysine complex resolve this discrepancy by providing indisputable evidence for one model over another.

AAA Pathway Enzymes as Antifungal Inhibitor Targets

Although fungal infections pose little threat in healthy hosts, during the last few decades invasive fungal infections have emerged as an increasing cause of morbidity and mortality in immuno-compromised individuals, such as transplant recipients, cancer and burn patients, and those with acquired immunodeficiencies such as AIDS (29, 69-71). Currently, the species *Candida*, particularly *C. albicans*, is the most common causes of nosocomial fungal infection (72, 73). However, many other fungal pathogens have emerged including the genus *Cryptococcus,* which is the major cause of fungal pulmonary infections in AIDS patients (74) and the *Aspergillus* mold which causes a wide range of ailments, with the most severe being invasive pulmonary aspergillosis in individuals with weakened immune systems (75).

Most of the current therapies to treat invasive fungal infections fall into three major categories: polyenes, azoles, and echinocandins (76-78). Amphotericin B is the most commonly used polyene and functions by disrupting the fungal membrane. Although this agent has a broad fungal specificity, serious side effects, including nephrotoxicity and eventual renal failure, are common making this drug less than ideal. Azoles function by inhibiting the cytochorme P450-dependend enzyme lanosterol demethylase, an enzyme that produces a significant component of the plasma membrane in fungi. Members of this family include fluconazole, itraconazole and voriconazole. Fluconazole is routinely used as a prophylaxis in bone marrow transplant patients to reduce the risk and severity of fungal infections against *Candida,* but this has led to an increase in infections by non-filamentous fungal species including *Aspergillus* (79). The azole drug voriconazole effectively treats *Aspergillus* infections; however, it interacts with many other drugs causing problems for immunodeficient individuals needing

multiple medications. The echinocandins are newest class of antifungal agents and include caspofungin, anidulafungin and micafungin. Echinocandins are lipopeptides that act by specifically inhibiting β-1-3-glucan formation, a component of the fungal cell wall. The specificity of echinocandins is limited to the *Candida* and *Aspergillus* geneses, but they are more effective in treating drug-resistant invasive *Aspergillus* than other classes of antifungals. Though significant progress has been made in developing new antifungal agents, there is still precedence for the development of additional agents especially those that act on novel targets. Many of the current drugs have drawbacks, including severe side effects, interactions with other medications (76-78) or can become ineffective against resistant fungal species (80). Furthermore, treatment of some fungal infections such as aspergillosis with a single agent has a cure rate of only 50% (78) necessitating the development of combinatorial therapies and the discovery of novel antifungal agents especially against this type of infection.

The enzymes in the AAA pathway of lysine biosynthesis represent potential targets for the development of novel antifungal drugs, in part because they are absent in humans. Studies identifying essential genes in *A. fumigatus* either using a conditional promoter replacement method or *in silco* analysis model identified the AAA pathway enzymes HAc, SD and HCS as potential antifungal targets (81, 82). Additionally, a study of *A. nidulans*, the model *Aspergillus* organism, showed that a mutant lacking the ability to synthesize L-lysine (*lysA2*) had a reduced virulence when infected into murine models indicating that lysine levels in the lung are limited, thus making the AAA metabolic pathway a promising novel target for the development of antifungal targets (83). Although the AAA pathway enzymes have long been proposed to be targets for the control of pathogenic yeast (23), only recently have studies been published on the design of inhibitors to enzymes in this pathway. The rational design of carboxyaryl-substituted D-malic acids as analogs to 2-(R)-homocitrate or (2R, 3S)-homoisocitrate, the substrates of HAc, were shown to inhibit growth of *A. ndulans* by 50% at 3 mM compound, however this a very high level compared to the 1 uM of amphotericin B need to cause the same level of inhibition (84). Additionally, a study to design and test inhibitor compounds against HIDH found the molecule thiahomoisocitrate to be a strong inhibitor (K_i of 97 nM) on HIDH from *S. cerevisiae* (85). However, studies are still needed to

further develop these potential inhibitors as antifungal agents and to unearth potent inhibitors against other enzymes in the AAA pathway, especially against HCS, which catalyzes the first and committed step in this pathway.

Objectives of This Work

Since the initial purification of HCS, many genetic and biochemical studies have been performed to elucidate the mechanism and regulation of this enzyme. For example, HCS was found to be regulated at both the levels of gene expression and enzyme activity. Additionally, over the past decade both the kinetic and general chemical mechanism have been described for this enzyme. However, many questions addressing the specifics of the mechanism of regulation of HCS remain unanswered partly due to a lack of a structure of a member of the HCS family. In this work, we address the details of the mechanism and regulation of HCS by using a variety of biochemical approaches including structural studies and *in vivo* and *in vitro* functional assays (Chapters 2, 3). Furthermore, a HCS fluorescent activity assay was developed and used in high-throughput screening (HTS) to begin to identify HCS inhibitors that may be developed as broad-spectrum antifungals (Chapter 4).

REFERENCES

1. Osborne, T. B., and Mendel, L. B. (1914) Amino-acids in nutrition and growth, *J. Biol. Chem. 17*, 325-349.

2. Rose, W. C. (1957) The amino acid requirements of adult man, *Nutr. Abstr. Rev. Ser. Hum. Exp. 27*, 631-647.

3. Rose, W. C., Oesterling, M. J., and Womack, M. (1948) Comparative growth on diets containing ten and 19 amino acids, with further observations upon the role of glutamic and aspartic acids, *J. Biol. Chem. 176*, 753-762.

4. Davis, B. D. (1952) Biosynthetic interrelations of lysine, diaminopimelic acid, and threonine in mutants of Escherichia coli, *Nature 169*, 534-536.

5. Dewey, D. L., and Work, E. (1952) Diaminopimelic acid decarboxylase, *Nature 169*, 533-534.

6. Scapin, G., and Blanchard, J. S. (1998) Enzymology of bacterial lysine biosynthesis, *Adv. Enzymol. Relat. Areas Mol. Biol. 72*, 279-324.

7. Vogel, H. J. (1959) On Biochemical Evolution: Lysine Formation in Higher Plants, *Proc. Natl. Acad. Sci. U.S.A. 45*, 1717-1721.

8. Vogel, H. J. (1960) Two modes of lysine synthesis among lower fungi: evolutionary significance., *Biochim. Biophys. Acta 41*, 172-174.

9. Graham, D. E., and Huse, H. K. (2008) Methanogens with pseudomurein use diaminopimelate aminotransferase in lysine biosynthesis, *FEBS Lett. 582*, 1369-1374.

10. Gilvarg, C. (1960) Biosynthesis of diaminopimelic acid, *Fed. Proc. 19*, 948-952.

11. Bhattacharjee, J. K. (1985) alpha-Aminoadipate pathway for the biosynthesis of lysine in lower eukaryotes, *Crit. Rev. Microbiol. 12*, 131-151.

12. Kosuge, T., and Hoshino, T. (1998) Lysine is synthesized through the alpha-aminoadipate pathway in Thermus thermophilus, *FEMS Microbiol. Lett. 169*, 361-367.

13. Tucci, A. F., and Ceci, L. N. (1972) Homocitrate synthase from yeast, *Arch. Biochem. Biophys. 153*, 742-750.

14. Xu, H., Andi, B., Qian, J., West, A. H., and Cook, P. F. (2006) The alpha-aminoadipate pathway for lysine biosynthesis in fungi, *Cell Biochem. Biophys. 46*, 43-64.

15. Wulandari, A. P., Miyazaki, J., Kobashi, N., Nishiyama, M., Hoshino, T., and Yamane, H. (2002) Characterization of bacterial homocitrate synthase involved in lysine biosynthesis, *FEBS Lett. 522*, 35-40.

16. Bhattacharjee, J. K., and Strassman, M. (1967) Accumulation of tricarboxylic acids related to lysine biosynthesis in a yeast mutant, *J. Biol. Chem. 242*, 2542-2546.

17. Ye, Z. H., and Bhattacharjee, J. K. (1988) Lysine biosynthesis pathway and biochemical blocks of lysine auxotrophs of Schizosaccharomyces pombe, *J. Bacteriol. 170*, 5968-5970.

18. Gaillardin, C. M., Poirier, L., and Heslot, H. (1976) A kinetic study of homocitrate synthetase activity in the yeast Saccharomycopsis lipolytica, *Biochim. Biophys. Acta 422*, 390-406.

19. Hogg, R. W., and Broquist, H. P. (1968) Homocitrate formation in Neurospora crassa. Relation to lysine biosynthesis, *J. Biol. Chem. 243*, 1839-1845.

20. Masurekar, P. S., and Demain, A. L. (1974) Insensitivity of homocitrate synthase in extracts of Penicillium chyrosogenum to feedback inhibition by lysine, *Appl. Microbiol. 28*, 265-270.

21. Schmidt, H., Bode, R., and Birnbaum, D. (1989) Regulation of the lysine biosynthesis in Pichia guilliermondii, *Antonie Van Leeuwenhoek 56*, 337-347.

22. Schmidt, H., Bode, R., Lindner, M., and Birnbaum, D. (1985) Lysine biosynthesis in the yeast *Candida maltosa*: properities of some enzymes and regulation of the biosynthetic pathway, *J. Basic Microbiol. 25*, 675-681.

23. Garrad, R. C., and Bhattacharjee, J. K. (1992) Lysine biosynthesis in selected pathogenic fungi: characterization of lysine auxotrophs and the cloned LYS1 gene of Candida albicans, *J. Bacteriol. 174*, 7379-7384.

24. Zabriskie, T. M., and Jackson, M. D. (2000) Lysine biosynthesis and metabolism in fungi, *Nat. Prod. Rep. 17*, 85-97.

25. Irvin, S. D., and Bhattacharjee, J. K. (1998) A unique fungal lysine biosynthesis enzyme shares a common ancestor with tricarboxylic acid cycle and leucine biosynthetic enzymes found in diverse organisms, *J. Mol. Evol. 46*, 401-408.

26. Betterton, H., Fjellstedt, T., Matsuda, M., Ogur, M., and Tate, R. (1968) Localization of the homocitrate pathway, *Biochim. Biophys. Acta 170*, 459-461.

27. Chen, S., Brockenbrough, J. S., Dove, J. E., and Aris, J. P. (1997) Homocitrate synthase is located in the nucleus in the yeast Saccharomyces cerevisiae, *J. Biol. Chem. 272*, 10839-10846.

28. Goulden, S. A., and Chattaway, F. W. (1968) Lysine control of alpha-aminoadipate and penicillin synthesis in Penicillium chrysogenum, *Biochem. J. 110*, 55P-56P.

29. Walsh, T. J., and Groll, A. H. (1999) Emerging fungal pathogens: evolving challenges to immunocompromised patients for the twenty-first century, *Transpl. Infect. Dis. 1*, 247-261.

30. Hinnebusch, A. G. (1986) The general control of amino acid biosynthetic genes in the yeast Saccharomyces cerevisiae, *CRC Crit. Rev. Biochem. 21*, 277-317.

31. Delforge, J., Messenguy, F., and Wiame, J. M. (1975) The regulation of arginine biosynthesis in Saccharomyces cerevisiae. The specificity of argR- mutations and the general control of amino-acid biosynthesis, *Eur. J. Biochem. 57*, 231-239.

32. Ramos, F., and Waime, J.-M. (1985) Mutation affecting the speciic reulatory control of lysine biosynthetic enzymes in *Saccharomyces cerevisiae*, *Mol. Gen. Genet. 200*, 291-294.

33. Barthelmess, I. B. (1982) Mutants affecting amino acid cross-pathway control in Neurospora crassa, *Genet. Res. 39*, 169-185.

34. Ramos, F., Dubois, E., and Pierard, A. (1988) Control of enzyme synthesis in the lysine biosynthetic pathway of Saccharomyces cerevisiae. Evidence for a regulatory role of gene LYS14, *Eur. J. Biochem. 171*, 171-176.

35. Becker, B., Feller, A., el Alami, M., Dubois, E., and Pierard, A. (1998) A nonameric core sequence is required upstream of the LYS genes of Saccharomyces cerevisiae for Lys14p-mediated activation and apparent repression by lysine, *Mol. Microbiol. 29*, 151-163.

36. Feller, A., Dubois, E., Ramos, F., and Pierard, A. (1994) Repression of the genes for lysine biosynthesis in Saccharomyces cerevisiae is caused by limitation of Lys14-dependent transcriptional activation, *Mol. Cell. Biol. 14*, 6411-6418.

37. El Alami, M., Feller, A., Pierard, A., and Dubois, E. (2000) Characterisation of a tripartite nuclear localisation sequence in the regulatory protein Lys14 of Saccharomyces cerevisiae, *Curr. Genet. 38*, 78-86.

38. Urrestarazu, L. A., Borell, C. W., and Bhattacharjee, J. K. (1985) General and specific controls of lysine biosynthesis in Saccharomyces cerevisiae, *Curr. Genet. 9*, 341-344.

39. Banuelos, O., Casqueiro, J., Steidl, S., Gutierrez, S., Brakhage, A., and Martin, J. F. (2002) Subcellular localization of the homocitrate synthase in Penicillium chrysogenum, *Mol Genet Genomics 266*, 711-719.

40. Jaklitsch, W. M., and Kubicek, C. P. (1990) Homocitrate synthase from Penicillium chrysogenum. Localization, purification of the cytosolic isoenzyme, and sensitivity to lysine, *Biochem. J. 269*, 247-253.

41. Tracy, J. W., and Kohlhaw, G. B. (1975) Reversible, coenzyme-A-mediated inactivation of biosynthetic condensing enzymes in yeast: a possible regulatory mechanism, *Proc. Natl. Acad. Sci. U.S.A. 72*, 1802-1806.

42. Ramos, F., Verhasselt, P., Feller, A., Peeters, P., Wach, A., Dubois, E., and Volckaert, G. (1996) Identification of a gene encoding a homocitrate synthase isoenzyme of Saccharomyces cerevisiae, *Yeast 12*, 1315-1320.

43. Huh, W. K., Falvo, J. V., Gerke, L. C., Carroll, A. S., Howson, R. W., Weissman, J. S., and O'Shea, E. K. (2003) Global analysis of protein localization in budding yeast, *Nature 425*, 686-691.

44. Kwon, E. S., Jeong, J. H., and Roe, J. H. (2006) Inactivation of homocitrate synthase causes lysine auxotrophy in copper/zinc-containing superoxide dismutase-deficient yeast Schizosaccharomyces pombe, *J. Biol. Chem. 281*, 1345-1351.

45. Okada, T., Tomita, T., Wulandari, A. P., Kuzuyama, T., and Nishiyama, M. (2009) Mechanism of substrate recognition and insight into feedback inhibition of homocitrate synthase from thermus thermophilus, *J. Biol. Chem.*

46. Andi, B., West, A. H., and Cook, P. F. (2004) Stabilization and characterization of histidine-tagged homocitrate synthase from Saccharomyces cerevisiae, *Arch. Biochem. Biophys. 421*, 243-254.

47. Zheng, L., White, R. H., and Dean, D. R. (1997) Purification of the Azotobacter vinelandii nifV-encoded homocitrate synthase, *J. Bacteriol. 179*, 5963-5966.

48. Allen, R. M., Chatterjee, R., Madden, M. S., Ludden, P. W., and Shah, V. K. (1994) Biosynthesis of the iron-molybdenum cofactor of nitrogenase, *Crit Rev Biotechnol 14*, 225-249.

49. Hakoyama, T., Niimi, K., Watanabe, H., Tabata, R., Matsubara, J., Sato, S., Nakamura, Y., Tabata, S., Jichun, L., Matsumoto, T., Tatsumi, K., Nomura, M., Tajima, S., Ishizaka, M., Yano, K., Imaizumi-Anraku, H., Kawaguchi, M., Kouchi, H., and Suganuma, N. (2009) Host plant genome overcomes the lack of a bacterial gene for symbiotic nitrogen fixation, *Nature 462*, 514-517.

50. Qian, J., Khandogin, J., West, A. H., and Cook, P. F. (2008) Evidence for a catalytic dyad in the active site of homocitrate synthase from Saccharomyces cerevisiae, *Biochemistry 47*, 6851-6858.

51. Andi, B., West, A. H., and Cook, P. F. (2004) Kinetic mechanism of histidine-tagged homocitrate synthase from Saccharomyces cerevisiae, *Biochemistry 43*, 11790-11795.

52. Brown, W. H., and Foote, C. S. (1998) *Organic Chemistry, Second Edition*, Saunders College Publishing, Orlando, FL.

53. Qian, J., West, A. H., and Cook, P. F. (2006) Acid-base chemical mechanism of homocitrate synthase from Saccharomyces cerevisiae, *Biochemistry 45*, 12136-12143.

54. de Carvalho, L. P., and Blanchard, J. S. (2006) Kinetic and chemical mechanism of alpha-isopropylmalate synthase from Mycobacterium tuberculosis, *Biochemistry 45*, 8988-8999.

55. Koon, N., Squire, C. J., and Baker, E. N. (2004) Crystal structure of LeuA from Mycobacterium tuberculosis, a key enzyme in leucine biosynthesis, *Proc. Natl. Acad. Sci. U.S.A. 101*, 8295-8300.

56. Anstrom, D. M., Kallio, K., and Remington, S. J. (2003) Structure of the Escherichia coli malate synthase G:pyruvate:acetyl-coenzyme A abortive ternary complex at 1.95 A resolution, *Protein Sci. 12*, 1822-1832.

57. Howard, B. R., Endrizzi, J. A., and Remington, S. J. (2000) Crystal structure of Escherichia coli malate synthase G complexed with magnesium and glyoxylate at 2.0 A resolution: mechanistic implications, *Biochemistry 39*, 3156-3168.

58. Karpusas, M., Branchaud, B., and Remington, S. J. (1990) Proposed mechanism for the condensation reaction of citrate synthase: 1.9-A structure of the ternary complex with oxaloacetate and carboxymethyl coenzyme A, *Biochemistry 29*, 2213-2219.

59. Wiegand, G., and Remington, S. J. (1986) Citrate synthase: structure, control, and mechanism, *Annu. Rev. Biophys. Biophys. Chem. 15*, 97-117.

60. Wiegand, G., Remington, S., Deisenhofer, J., and Huber, R. (1984) Crystal structure analysis and molecular model of a complex of citrate synthase with oxaloacetate and S-acetonyl-coenzyme A, *J. Mol. Biol. 174*, 205-219.

61. de Carvalho, L. P., Frantom, P. A., Argyrou, A., and Blanchard, J. S. (2009) Kinetic evidence for interdomain communication in the allosteric regulation of alpha-isopropylmalate synthase from Mycobacterium tuberculosis, *Biochemistry 48*, 1996-2004.

62. Gantt, S. L., Gattis, S. G., and Fierke, C. A. (2006) Catalytic activity and inhibition of human histone deacetylase 8 is dependent on the identity of the active site metal ion, *Biochemistry 45*, 6170-6178.

63. Hernick, M., and Fierke, C. A. (2006) Molecular recognition by Escherichia coli UDP-3-O-(R-3-hydroxymyristoyl)-N-acetylglucosamine deacetylase is modulated by bound metal ions, *Biochemistry 45*, 14573-14581.

64. Umbarger, H. E. (1961) Feedback control by endproduct inhibition, *Cold Spring Harb. Symp. Quant. Biol. 26*, 301-312.

65. Umbarger, H. E. (1969) Regulation of amino acid metabolism, *Annu Rev Biochem 38*, 323-370.

66. Maragoudakis, M. E., Holmes, H., and Strassman, M. (1967) Control of lysine biosynthesis in yeast by a feedback mechanism, *J. Bacteriol. 93*, 1677-1680.

67. Demain, A. L., and Masurekar, P. S. (1974) Lysine inhibition of in vivo homocitrate synthesis in Penicillium chrysogenum, *J. Gen. Microbiol. 82*, 143-151.

68. Andi, B., West, A. H., and Cook, P. F. (2005) Regulatory mechanism of histidine-tagged homocitrate synthase from Saccharomyces cerevisiae. I. Kinetic studies, *J. Biol. Chem. 280*, 31624-31632.

69. Branski, L. K., Al-Mousawi, A., Rivero, H., Jeschke, M. G., Sanford, A. P., and Herndon, D. N. (2009) Emerging infections in burns, *Surg. Infect. (Larchmt) 10*, 389-397.

70. Kaplan, J. E., Benson, C., Holmes, K. H., Brooks, J. T., Pau, A., and Masur, H. (2009) Guidelines for prevention and treatment of opportunistic infections in HIV-infected adults and adolescents: recommendations from CDC, the National Institutes of Health, and the HIV Medicine Association of the Infectious Diseases Society of America, *MMWR Recomm. Rep. 58*, 1-207; quiz CE201-204.

71. Mofenson, L. M., Brady, M. T., Danner, S. P., Dominguez, K. L., Hazra, R., Handelsman, E., Havens, P., Nesheim, S., Read, J. S., Serchuck, L., and Van Dyke, R. (2009) Guidelines for the Prevention and Treatment of Opportunistic Infections among HIV-exposed and HIV-infected children: recommendations from CDC, the National Institutes of Health, the HIV Medicine Association of the Infectious Diseases Society of America, the Pediatric Infectious Diseases Society, and the American Academy of Pediatrics, *MMWR Recomm. Rep. 58*, 1-166.

72. De Rosa, F. G., Garazzino, S., Pasero, D., Di Perri, G., and Ranieri, V. M. (2009) Invasive candidiasis and candidemia: new guidelines, *Minerva Anestesiol. 75*, 453-458.

73. Eggimann, P., Garbino, J., and Pittet, D. (2003) Epidemiology of Candida species infections in critically ill non-immunosuppressed patients, *Lancet Infect. Dis. 3*, 685-702.

74. Huston, S. M., and Mody, C. H. (2009) Cryptococcosis: an emerging respiratory mycosis, *Clin. Chest Med. 30*, 253-264, vi.

75. Dagenais, T. R., and Keller, N. P. (2009) Pathogenesis of Aspergillus fumigatus in Invasive Aspergillosis, *Clin. Microbiol. Rev. 22*, 447-465.

76. Enoch, D. A., Ludlam, H. A., and Brown, N. M. (2006) Invasive fungal infections: a review of epidemiology and management options, *J. Med. Microbiol. 55*, 809-818.

77. Mathew, B. P., and Nath, M. (2009) Recent approaches to antifungal therapy for invasive mycoses, *ChemMedChem 4*, 310-323.

78. Rogers, T. R., and Frost, S. (2009) Newer antifungal agents for invasive fungal infections in patients with haematological malignancy, *Br. J. Haematol. 144*, 629-641.

79. Caston-Osorio, J. J., Rivero, A., and Torre-Cisneros, J. (2008) Epidemiology of invasive fungal infection, *Int. J. Antimicrob. Agents 32 Suppl 2*, S103-109.

80. Peman, J., Canton, E., and Espinel-Ingroff, A. (2009) Antifungal drug resistance mechanisms, *Expert Rev. Anti. Infect. Ther. 7*, 453-460.

81. Hu, W., Sillaots, S., Lemieux, S., Davison, J., Kauffman, S., Breton, A., Linteau, A., Xin, C., Bowman, J., Becker, J., Jiang, B., and Roemer, T. (2007) Essential gene identification and drug target prioritization in Aspergillus fumigatus, *PLoS Pathog. 3*, e24.

82. Thykaer, J., Andersen, M. R., and Baker, S. E. (2009) Essential pathway identification: from in silico analysis to potential antifungal targets in Aspergillus fumigatus, *Med. Mycol. 47 Suppl 1*, S80-87.

83. Tang, C. M., Smith, J. M., Arst, H. N., Jr., and Holden, D. W. (1994) Virulence studies of Aspergillus nidulans mutants requiring lysine or p-aminobenzoic acid in invasive pulmonary aspergillosis, *Infect. Immun. 62*, 5255-5260.

84. Palmer, D. R., Balogh, H., Ma, G., Zhou, X., Marko, M., and Kaminskyj, S. G. (2004) Synthesis and antifungal properties of compounds which target the alpha-aminoadipate pathway, *Pharmazie 59*, 93-98.

85. Yamamoto, T., and Eguchi, T. (2008) Thiahomoisocitrate: a highly potent inhibitor of homoisocitrate dehydrogenase involved in the alpha-aminoadipate pathway, *Bioorg. Med. Chem. 16*, 3372-3376.

CHAPTER 2
CRYSTAL STRUCTURE AND FUNCTIONAL ANALYSIS OF HOMOCITRATE SYNTHASE

Many organisms can synthesize lysine utilizing one of two distinct biosynthetic pathways. In plants and most bacteria lysine is synthesized via the DAP pathway (1-3). Yeast, and most fungi, including the human pathogens *Cryptococcus neoformans, Candida albicans* and *Aspergillus fumigatus,* and some archaebacteria, including *Thermus thermophilus* utilize the AAA pathway to synthesize lysine (4-7). Because HCS is unique to fungi, and absence in mammals, these enzymes represent an excellent target for screening and developing small molecule inhibitors that may have potential clinical value as broad-spectrum anti-fungal therapeutics, particularly for immuno-compromised individuals, such as AIDS and cancer patients and transplant recipients, who are at higher risk of developing invasive fungal infections.

The AAA lysine biosynthetic pathway in fungi and yeast consists of eight enzymatic steps with HCS catalyzing the first and committed step in this pathway by transferring an acetyl group from AcCoA to 2-OG to form homocitrate and CoA (5, 8). The kinetic mechanism of ScHCS Lys20 was determined to be a sequential Bi-Bi reaction with 2-OG binding before AcCoA followed by the release of CoA before homocitrate (9). The reaction mechanism of HCS has been proposed to follow a general acid base mixed Claisen condensation reaction (10), which is the same mechanism used by citrate synthase (11), malate synthase (12, 13) and α-IPMS (14). Based on the structure of α-IPMS, mutagenesis and kinetic studies of ScHCS Lys20 have provided evidence that a glutamate-histidine catalytic dyad is responsible for the deprotonation of the AcCoA acetyl group (15). However, without a structure of a HCS, the residues that act as the general acid and general base are not definitively known.

Here we describe the first crystal structures of a fungal HCS along with two distinct binary complexes with the substrate 2-OG. In one of the 2-OG binary complexes, a lid motif covers the entrance to the active site, gating access for substrate binding.

Steady state kinetic assays and *in vivo* yeast growth assays on WT SpHCS and active site allow us to elucidate the contribution these residues play in substrate binding and catalysis. Together these results yield new insights into the mechanism of HCS, which provides a platform for identifying anti-fungal modulators of HCS.

MATERIALS AND METHODS

Materials

DNA primers used for cloning were purchased from Invitrogen, whereas primers used for mutagenesis were obtained from Integrated DNA Technologies. The pLp2211 vector containing *lys4*$^{+}$ under the control of the *S. cerevisiae* HCS *LYS20* promoter was constructed in the laboratory of Lorraine Pillus at the University of California San Diego. Tobacco Etch Virus (TEV) protease was purified on Talon resin essentially as described (16), but was further purified by eluting with a 100 mM to 1 M NaCl gradient on a SP-sepharose ion exchange column (Amersham Biosciences) at pH 8.0. Peak fractions were concentrated to 1 mg/mL (ε_{280nm} = 31970$M^{-1}cm^{-1}$) and glycerol was added to 10% (v/v). Aliquots were flash frozen and stored at -80 ^{o}C. Amino acids and L-selenomethionine used in the selenomethionine minimal media were purchased from Sigma. The polyethylene glycol (PEG) 400, sodium phosphate monobasic and potassium phosphate dibasic used in crystallization screens were purchased from sigma at the highest quality available, while the magnesium acetate was supplied as a 1 M solution from Hampton Research. Thiostar [10-(2,5-dihydro-2, 5-di-oxo-1H-pyrrol-1-yl)-9-methoxy-3-oxo-, methyl ester 3*H*-naphthol(2,1-b) pyran-*S*-carboxylic acid] dye was purchased from Luminos LLC and prepared by dissolving in dimethyl sulfoxide (DMSO). The concentration of the dye was determined by measuring its absorbance at 381 nM and using an extinction coefficient of 15,100 M^{-1} cm^{-1}. AcCoA trilithium salt was purchased from Sigma. Commercially available AcCoA is contaminated with a small percentage of CoA, which causes high background in the HCS fluorescent assay. Therefore, purchased AcCoA (25 mg) was treated with 50 μL acetic anhydride (Fluka) for 10 minutes at room temperature, brought up to 1 mL with 100 mM HEPES, pH 7.5 and the concentration was measured (ε_{260nm} = 15,400 M^{-1} cm^{-1}). Aliquots were flash frozen and stored at -80 ^{o}C until use. 2-OG disodium salt was purchased from Fluka and

was stored as a 1 M stock at -20 ^{o}C. CoA trilithium salt was purchased from Sigma and stocks were made up in water and the concentration was determined (ε_{260nm} = 15,400 M^{-1} cm^{-1}) before flash freezing and storing at -80 ^{o}C. All other materials used were of the highest grade available.

Cloning of SpHCS

Full length HCS encoded by the *lys4*$^{+}$ gene was amplified from *Schizosaccharomyces pombe* genomic clone SPBC1105.02c (Sanger Institute) using the polymerase chain reaction and the following primers: 5'-GCAGGTAAGATGGTAGGA TCCATGTCTGTGTCCGAAGCAA-3' and 5'-CTGGCTCATCCGCTCGAGGAATTCT TAAGCAGACGCTTCTTTGG-3'. The PCR reaction was catalyzed using Platinum *Pfx* DNA Polymerase (Invitrogen) and the resulting DNA fragment was purified using agarose gel electrophoresis on a 1% agarose gel and a rapid gel extraction kit (Marligen). The SpHCS DNA and a parallel expression vector pHIS2 (17), which contains an N-terminal 6xHIS tag and TEV protease cleavage site, were each digested for 1 hour at 37 ^{o}C with the restriction enzymes BamH1 and EcoR1. The digested SpHCS DNA and pHIS2 vector were PCR purified (Marligen) and ligated using T4 DNA ligase. Ligation product was transformed into calcium competent *Escherichia coli* DH5α cells, which were grown overnight at 37^{o} C on Luria-Broth (LB) agar plates containing 100 μg/mL ampicillin (AMP). Plasmid DNA from resulting colonies was purified using a QIAprep Spin Miniprep kit (Qiagen) and dideoxynucleotide sequencing was performed (University of Michigan DNA Sequencing Core) to confirm the sequence of the *lys4*$^{+}$ gene.

Mutagenesis of SpHCS Active Site Residues

Active site mutants of SpHCS/pHIS2 and SpHCS/pLp2211 were made using site-directed mutagenesis following a modified Quikchange^{TM} mutagenesis kit protocol (Stratagene). Complimentary sets of primers containing the mutations were designed (Table 2.1) and PCR reactions (50 μL) were set up with 10 or 20 ng vector/SPHCS DNA, 125 ng of each primer, 300 μM dNTPs (Invitrogen), 1X PfuUltra^{TM} HF reaction buffer

Table 2.1 Primers used for SpHCS site directed mutagenesis.

Mutation	Primer
R43A	5′-CCATTATTGAGTCTACTCTT**GCT**GAAGGTGAGCAATTCGC-3′[a]
R43K	5′-CCATTATTGAGTCTACTCTT**AAG**GAAGGTGAGCAATTCGC-3′
R43Q	5′-CCATTATTGAGTCTACTCTT**CAG**GAAGGTGAGCAATTCGC-3′
Q47A	5′-CTACTCTTCGTGAAGGTGAG**GCA**TTCGCAAACGCTTTTTTCG-3′
E74A	5′-CTTTGGTGTCGATTACATT**GCA**TTGACTTCTCCCGTGGC-3′
E74Q	5′-CTTTGGTGTCGATTACATT**CAA**TTGACTTCTCCCGTGGC-3′
H103A	5′-GGCTTAAAGTGTAAAATTTTAACT**GCT**ATTCGCTGTCATATGG-3′
R163A	5′-GCAAGGGTATTGAAGTC**GCC**TTTTCATCTGAGGATTCTTTCCG-3′
R163K	5′-GCAAGGGTATTGAAGTC**AAG**TTTTCATCTGAGGATTCTTTCCG-3′
R163Q	5′-GCAAGGGTATTGAAGTC**CAG**TTTTCATCTGAGGATTCTTTCCG-3′
S165A	5′-GCAAGGGTATTGAAGTCCGCTTT**GCA**TCTGAGGATTCTTTCCG-3′
E167A	5′-GAAGTCCGCTTTTCATCT**GCG**GATTCTTTCCGTTCTGATC-3′
E167Q	5′-GAAGTCCGCTTTTCATCT**CAG**GATTCTTTCCGTTCTGATC-3′
T197A	5′-CCGTGTTGGTATTGCTGAC**GCC**GTTGGTTGCGCTACTCCTCGCC-3′
T197S	5′-CCGTGTTGGTATTGCTGAC**TCC**GTTGGTTGCGCTACTCCTCGCC-3′
T197V	5′-CCGTGTTGGTATTGCTGAC**GTC**GTTGGTTGCGCTACTCCTCGCC-3′
H321A	5′-GCTTTTACCCATAAGGCTGGTATC**GCT**GCTAAAGCTATTCTCGC-3′
Y332A	5′-CGCTAACCCTTCTACA**GCT**GAAATTCTTAAGCCCGAGG-3′
Y333F	5′-CGCTAACCCTTCTACA**TTT**GAAATTCTTAAGCCCGAGG-3′

[a]Forward primer is listed with reverse primer being the reverse complement of the forward primer. The mutated codon is denoted in bold.

and 2.5 U pfuUltra^{TM} HF DNA polymerase (Stratagene). The reactions were cycled for 30 seconds at 95 ^{o}C followed by 16 rounds of 30 seconds at 95 ^{o}C, 1 minute at 55 ^{o}C and 9 minutes at 68 ^{o}C in a thermocycler. The resulting amplifications were digested with 20 U *Dpn* 1 (Invitrogen) for 1 hour at 37 ^{o}C and 1 μL of the digest was transformed into *E. coli* DH5α cells. The cells were plated on LB agar plates containing 100 μg/mL AMP and grown overnight at 37 ^{o}C. DNA from the resulting colonies was isolated utilizing a QIAprep Spin Miniprep kit (Qiagen) and the mutated sequences were verified by dideoxynucleotide sequencing (University of Michigan DNA Sequencing Core).

Expression of SpHCS

SpHCS/pHIS2 plasmid was transformed into *E. coli* Rosetta2 (DE3) cells (EMD Biosciences) and grown overnight at 37 ^{o}C on LB agar plates containing 100 μg/mL AMP and 50 μg/mL chloramphenicol (CHLOR). Several colonies were transferred and grown in a starter culture of 2X-YT media supplemented with 100 μg/mL AMP and 50 μg/mL CHLOR overnight at 37 ^{o}C. SpHCS was over expressed by inoculating the starter culture into twelve flasks of 500 mL 2X YT media supplemented with 100 μg/mL AMP and 50 μg/mL CHLOR. The cells were grown at 37 ^{o}C to an OD_{600} of 0.3 and the temperature was reduced to 18 ^{o}C. Once the shaker reached 18 ^{o}C, protein was overexpressed by adding 0.1 mM isopropyl β-D-1-thiogalactopyranoside (IPTG) and growing the cells overnight. Harvested cells were resuspended in lysis buffer consisting of 50 mM sodium phosphate pH 7.0, 500 mM NaCl, 5mM β-mercaptoethanol (β-me) and stored at -20 ^{o}C.

Purification of SpHCS for Crystallization

All purification steps were performed at 4 ^{o}C unless otherwise stated. Cell pellets were thawed and lysed by adding 5 mg lysozyme and rocking at room temperature for 1 hour followed by a flash freeze and thaw cycle. The cells were sonicated after the addition of 30 mL lysis buffer and the insoluble material was separated from the soluble enzyme by centrifugation at 15,000 rpm for 20 minutes in a Sorvall SS-34 rotor. The soluble enzyme was loaded onto a Talon (Clontech) Co(II) immobilized metal affinity

chromatography (IMAC) column pre-equilibrated in lysis buffer and eluted with a linear gradient of 0-500 mM imidazole. Fractions containing SpHCS were pooled and the 6xHIS tag was removed by TEV protease during dialysis in a 10,000 MW cut-off bag (Pierce) overnight against 50 mM sodium phosphate, pH 8.0, 150 mM NaCl and 5 mM β-me. The NaCl and imidazole concentrations in the dialyzed protein were brought up to 500 mM and 40 mM respectively and the TEV protease and undigested SpHCS were removed by batch binding to 5 mL Talon resin for 1 hour. Unbound SpHCS was concentrated to 2 mL using an 30k Amicon Ultra centrifugal Filter Device (Millipore) and was further purified by loading onto a Superdex 200 (GE healthcare) gel filtration column and isocratically eluted with 25 mM Tris, pH 9.0, 50 mM NaCl, 1 mM tris(2-carboxyethyl)phosphine (TCEP). In some cases for crystallization, SpHCS was treated with 10mM EDTA prior to gel filtration to remove the bound divalent metal. Peak fractions were judged to be essentially pure by SDS-PAGE and were concentrated to 40-80 mg/mL as measured by absorbance at 280 nM using the calculated extinction coefficient of 28350 M^{-1} cm^{-1}. Concentrated SpHCS was flash frozen and stored at -80 ^{o}C.

Purification of SpHCS and SpHCS Mutants for Kinetic Studies

A Zn(II) charged IMAC sepharose 6 Fast flow (GE Healthcare) resin was used in the first steps of the purification of SpHCS and SpHCS mutants used in kinetic studies. With the exception of the IMAC resin, the purification was performed identically as described for crystallization.

Inductively Coupled Plasma-High Resolution Mass Spectroscopy

WT SpHCS from two different purifications on Zn(II) charged IMAC sepharose along with WT SpHCS from a Talon Co(II) IMAC purification treated with EDTA were diluted to 20 μM in 50 mM HEPES, pH 7.5. Metal content was analyzed using a ThermoFisher Finnigan Element Inductively Coupled Plasma-High Resolution Mass Spectrometer (ICP-HRMS; University of Michigan, Department of Geology) with the protein buffer analyzed as a control. Metal standard calibration curves were performed at 0-100ppb.

Preparation of Selenomethionyl-Incorporated SpHCS

Selenomethionyl-SpHCS (SeMet-SpHCS) was prepared following a modified protocol of Doubolié (*18, 19*). Selenomethionine minimal media (10 L) was prepared by cooling 5 L of autoclaved MilliQ water to 60 ^{o}C and adding 0.4 g tyrosine and 5.0 g of each of the following bases: adenine, guanosine, thymine and uracil (TyB media). The TyB media was cooled to room temperature and divided into two 6 L flasks and the following was added to each flask: 100 mL of 50x amino acid mix (all amino acids at 0.2 mg /mL except for tyrosine, glutamine and methionine), 100 mL 50% glycerol, 50 mL 20% glucose, 10 mL glutamine (20 mg/mL), 6.25 mL trace metal ion mix (5g $FeCl_2$•4 H_2O, 184 mg $CaCl_2$•2 H_2O, 64 mg H_3BO_3, 40 mg $MnCl_2$•4 H_2O, 18 mg $CoCl_2$•6 H_2O, 4 mg $CuCl_2$•2 H_2O, 340 mg $ZnCl_2$ and 605 mg Na_2MoO_4•2 H_2O dissolved in 8 mL concentrated HCl and brought up to 500 mL with water), 5.0 mL 1M $MgSo_4$, 2.5 ml 1M $CaCl_2$, and 2.0 ml thiamine (5 mg/mL), 1 L autoclaved selenomethionine salts (5 mg/mL NH_4SO_4, 22.5 mg/mL KH_2PO_4, 52.5 mg/mL K_2PO_4 and 2.5 mg/mL Na_3Citrate), 1.25 L autoclaved water and 200 mg L-selenomethionine. SpHCS/pHIS2 plasmid was transformed into the methionine auxotroph *E. coli* B843 (DE3) cell line and a starter culture of the cells was grown overnight in LB media supplemented with 100 mg/mL AMP and 50 mg/mL CHLOR. The selenomethionine minimal media with 100 mg/mL AMP and 50mg/mL CHLOR was inoculated with a 1/100 dilution of the starter culture and SeMet-SpHCS was overexpressed and purified identically to wild type enzyme used for crystallization.

Crystallization of SpHCS

To identify initial conditions that produced crystals of SpHCS, several commercially available sparse matrix crystallization screens were utilized including the Index HT Screen (Hampton Research), Wizard I and II Screen (Emerald BioSystems) Structure Screen 1 and 2 (Molecular Dimensions) and JCSG+ Suite Screen (Qiagen formally Nextal). Crystallization was carried out in 96 well protein sitting drop crystallization plates (Greiner Bio-One) by adding 70 uL of the crystallization solution to the reservoir well and 2 μL a 1:1 ratio of the protein mixture (20-24 mg/mL SpHCS,

1-2 mM CoA, 1-50 mM 2-OG) to crystallization solution to the crystallization wells. The trays were immediately sealed, incubated at 20 ^{o}C or 24 ^{o}C and observed daily for crystal formation.

SpHCS protein crystals formed in several initial conditions, a few of which were optimized to obtain the largest and sharpest looking crystals. To identify optimized crystallization conditions, the hanging drop vapor diffusion method was employed using 24 well VDX™ plates (Hampton Research). A 2 μL drop of a 1:1 ratio of protein mixture to crystallization condition was dispensed onto cover slides, which were sealed over each reservoir containing 500 μL of the crystallization condition. SpHCS-free enzyme protein crystals formed in 100 mM HEPES, pH 6.8-7.2, 200 mM Mg acetate, 16-25% (v/v) PEG 400 at 24 ^{o}C using 24 mg/ mL native SpHCS or SeMet-SpHCS, 1 mM CoA and 1 mM 2-OG. To obtain crystals of SpHCS in complex with the substrate 2-OG, a phosphate condition was optimized. Crystals of the SpHCS open loop complex with 2-OG were obtained in 1.3-1.6 M Na/KPO_4 (pH 5.4-6.4) at 24 ^{o}C using 20 mg/mL EDTA treated SpHCS, 1 mM Zn(II), 2 mM CoA and 50 mM 2-oxoglutarate while crystals of the SpHCS closed loop complex with 2-OG were obtained in 1.2-1.8 M Na/KPO_4, pH 5.6-6.8 at 24^{o} C using 24 mg/mL SpHCS, 2 mM CoA and 50 mM 2-OG. Optimized crystals were harvested, cryo-protected in the crystallization condition containing 20% glycerol and flash frozen in liquid nitrogen.

Phase Determination and Data Collection

To determine the phases needed for SpHCS structure determination, the selenomethionyl single wavelength anomalous dispersion (SAD) technique was used (20). Data was collected at the phi and inverse phi angles on a single SeMet-SpHCS crystal at the experimentally determined selenium peak (0.97913 Å) using the 23-ID-B beamline of General Medicine Cancer Institutes-Collaborative Access Team (GM/CA-CAT) at the Advanced Source Synchatron (Table 2.2). The data was then processed and scaled using HKL2000 (21). The program SOLVE/RESOLVE (22) located 8/9 initial Se sites in a $P6_222$ space group and the program autoSHARP (23) was used to refine the heavy atom sites, calculate and refine SAD phases, perform density modification and build a partial model. A complete high-resolution data set was also collected to 2.24 Å using a different

Table 2.2 Data collection and refinement statistics.

	SeMet SpHCS SAD [Co(II)]	SeMet SpHCS-Apoenzyme [Co(II)]	WT SpHCS/2OG closed lid [Zn(II)]	WT SpHCS/2OG open lid [Co(II)]
Data Collection				
Beamline	23-ID-B	23-ID-B	21-ID-G	21-ID-G
Space group	$P6_222$	$P6_2$	$P6_2$	$P6_2$
Cell dimensions a=b, c (Å)	136.9, 120.9	136.0, 122.1	133.7, 125.9	133.8, 125.7
Wavelength (Å)	0.97913	0.97930	0.97856	0.97872
Resolution (Å)	40.0-2.70 (2.80-2.70)[a]	50.0-2.24 (2.33-2.24)	40.0-2.67 (2.78-2.67)	40.0-2.72 (2.82-2.72)
R_{merge} (%)	7.9 (32.5)	6.0 (54.0)	6.0 (51.2)	5.6 (49.5)
I/σI	48.3 (15.4)	28.1 (3.67)	35.4 (4.54)	22.2 (2.54)
Reflections				
Total	657,489	446,827	343,456	125,123
Unique	18,936	60,860	36,145	33,176
Redundancy	34.7 (31.7)	7.3 (7.0)	9.5 (8.8)	3.8 (3.7)
Completeness (%)	100.0 (100.0)	99.4 (99.7)	100.0 (100.0)	96.4 (98.5)
Phasing power	2.789			
Sites found/total	8/9			
F.O.M.[b]	0.4727/0.8464			
Refinement				
Resolution range (Å)		29.45-2.24	39.4-2.67	39.41-2.72
No. of reflections		60,728	36,061	31,491
No. of atoms		6064	6324	5935
Protein atoms		5788	6149	5794
Metals/ligand atoms		4/--	4/20	4/20
Water atoms		272	151	117
R_{work}/R_{free}[c]		19.1/22.1	16.5/20.7	17.9/21.9
Average B-factors (Å^2)				
Overall		54.5	54.5	63.3
Protein		55.1	55.7	66.2
Metals/Ligand		54.9/--	38.6/57.8	51.1/78.7
Water		59.0	56.3	63.5
R.m.s. deviations				
Bond length (Å)		0.012	0.013	0.013
Bond angles (°)		1.294	1.436	1.472
MolProbity score		1.93[d]	2.09[e]	2.28[f]
Ramachandran favored (%)		96.69	96.20	96.43
Ramachandran allowed (%)		3.31	3.80	3.57
Ramachandran outliers (%)		0.00	0.00	0.00

[a]Values in parentheses are for the highest-resolution shell.
[b]Before and after density modification in SHARP.
[c]$R_{work} = \sum ||F_o| - |F_c|| / \sum |F_o|$; $R_{free} = \sum T||F_o| - |F_c|| / \sum T|F_o|$, where T is a randomly chosen set of reflections consisting of 5% of the total reflections.
[d]89th percentile for 1.99-2.49 Å structures.
[e]97th percentile for 2.42-2.92 Å structures.
[f]94th percentile for 2.47-2.97 Å structures.

SeMet-SpHCS crystal at the 23-ID-B beamline. The detector distance was set to 225 mm and 120 degrees of data were collect at 0.5^o of oscillation with an exposure time of 3 seconds at a wavelength of 0.97930 Å.

Data sets for SpHCS in complex with the substrate 2-OG were collected at the 21-ID-G beamline of Life Sciences-Collaborative Access Team (LS-CAT). The open loop complex (120^o of data at 0.5^o oscillation) was collect at a wavelength of 0.9782 Å with a detector distance of 320 mm and an exposure time of 3 seconds. Data (150^o at 0.5^o oscillation) for the closed loop complex 150^o of data at 0.5^o oscillation collected for the closed loop complex at a wavelength of 0.97856 Å with a detector distance of 300 mm and an exposure time of 9 seconds. Both the 2-OG open and closed data sets were processed and scaled in HKL2000 (21).

Model Building and Refinement

The partial model built by autoSHARP (23) using the SAD phases and data from the SeMet-SpHCS crystal was completed by alternating between refinement using CNS (24, 25) and manual building in the program Coot (26). The initial model consisted of a monomer in which the main chain of 350 out of 418 residues was built. This model was then used for molecular replacement with the high resolution SeMet SpHCS data set in MOLREP (27) with the programs Coot (26) and REFMAC (28) used for model building and refinement, respectively. The R-factors remained high during refinement in the higher symmetry space group $P6_222$ because the crystallographic two-fold axis is forced to coincide with the pseudo-symmetry of the molecular two-fold axis of the dimer, masking subtle differences between the two monomers. This problem was resolved by refining in the lower space group $P6_2$ in which the entire homodimer was refined, allowing for minor variations in the conformation of each monomer. In later stages of refinement, residues with alternative conformations were modeled, TLS refinement (29) was applied and water molecules were added. The SpHCS 2-OG complexes were built and refined similarly to the high resolution SeMet SpHCS data set. The final SeMet-SpHCS structure has $R_{working}$ and R_{free} values of 19.1% and 22.1% respectively, while the final R_{work} and R_{free} values for the 2-OG open lid and the 2-OG closed lid structures were 17.9% and 21.9% and 16.5% and 20.7% respectively (Table 2.2). No residues in any of

the structures were found in the disallowed regions of the Ramachandran plot as determined by MolProbity (30). Simulated annealing omits maps for 2-OG were calculated in CNS (24, 25).

Kinetic Studies Using a Fluorescent HCS Assay

The fluorescence assay used to determine the steady state kinetic parameters of SpHCS and SpHCS mutants was adapted from previous work (31). Instead of using the fluorescent dye CPM [7-diethylamino-3-(4-maleimidylphenyl)-4-methylcoumarin], ThioStar was used (32) (Scheme 2.1). HCS assays were carried out in triplicate at room temperature in 100mM HEPES, pH 7.5 with potassium hydroxide. Before adding to the reaction mixture, AcCoA stocks were diluted 2:1 in 1 M HEPES, pH 7.5 to bring the pH of the solution to 5. To determine K_M and k_{cat} values for AcCoA, the 2-OG concentration was held at a saturating concentration of 5 mM to 200 mM, and the AcCoA concentration was varied from 0-400 μM. To determine K_M and k_{cat} values for 2-OG, the AcCoA concentration was held at a saturating concentration of 200 μM or 400 μM and the 2-OG concentration was varied from 0-200 mM. The enzyme concentration used in the assays was 10-100 nM. Assays were initiated with the addition of enzyme into a 220 μL reaction mixture and 50 μL aliquots were quenched at 0, 1, 2 and 3 minutes in 50 μL DMSO dispensed into individual wells of a black round bottom 96-well polypropylene plate (Corning). After completing the assay, 100 μL of 25 μM ThioStar was added to each well and allowed to react in the dark for 10 min. The plate was then read on a Genios Pro (Tecan) using emission and excitation filters at 400 nM and 510 nM at 25 ^{o}C with a gain setting of 30. Standard curves were measured in duplicate with each assay using 0-10 μM CoA in 100 mM HEPES, pH 7.5. Additionally, to correct for the increased fluorescence of the ThioStar dye with increasing concentrations of 2-OG over 2 mM, CoA standard curves were performed at every 2-OG concentration above 2 mM used in each assay.

Fluorescence acetyltransferase data was analyzed in Excel (Microsoft) by first converting fluorescence values to CoA concentrations by using the CoA standard curves. Initial velocities (ν_o) were determined by fitting a least squares linear fit to CoA concentration versus time for each substrate concentration assay. Initial velocities were plotted versus substrate concentration ([S]) and were fit to the Michaelis-Menten

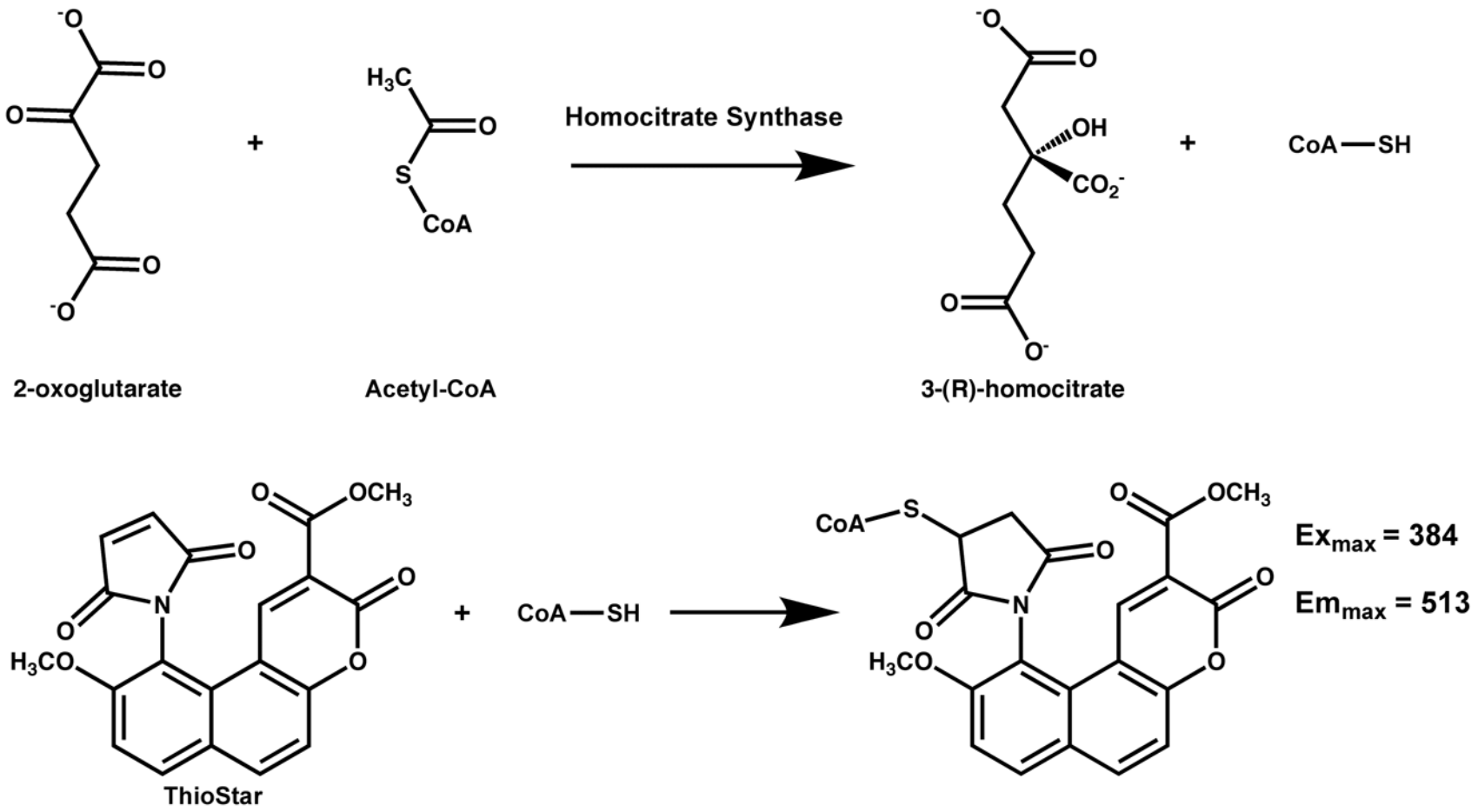

Scheme 2.1 HCS fluorescence assay. The CoA-SH generated in the HCS reactions is quantified by reacting with the sulfhydryl-sensitive fluorophore Thiostar, which produces a thiol adduct that fluoresces strongly at 513 nM when excited at 384 nM.

equation (Eq. 1) in SigmaPlot (Systat Software) or Prism (GraphPad Software) to determine K_M and k_{cat} values.

$$\text{Eq 1: } v_o = k_{cat}[E_t][S]/([S] + K_M)$$

Circular Dichroism Spectroscopy of Inactive SpHCS Mutants

To confirm proper folding of the inactive SpHCS mutants circular dichroism was measured using a J-715 spectropolarimeter (Jasco) at room temperature in a 1 mm pathlength cell. Enzyme was diluted to 0.1 mg/mL in 50 mM sodium phosphate, pH 7.5 and scans were taken at 100 nm/ second at a bandwidth of 1 nM and response time of 1 second. Each spectrum represents the average of 20 consecutive scans, which were corrected for baseline and converted to mean residue ellipiticity.

***In vivo* Cell Growth Assay for HCS Activity**

Yeast strain LPY 11411 (*MATa ade2-1 can1-100 his3-11,15 leu2-3,112 trp1 ura3-1 rDNA::ADE2CAN1 lys20Δ::KanMX lys21Δ::NATMX4)* was transformed using lithium acetate method with empty 2 μm *URA3* vector pRS202 (pLP1402), pRS202 containing *LYS20* (pLP1412*)*, pRS426 containing *lys4*$^+$ under the control of the *S. cerevisiae LYS20* promoter (pLP2211), or pLP2211 containing point mutations of *lys4*$^+$. Yeast cells were grown on synthetic complete medium lacking uracil or uracil and lysine according to standard procedures (33). Western blot analysis demonstrated that the steady state levels of the SpHCS mutant proteins were comparable to that of the WT SpHCS.

RESULTS

Purification and Structure Determination of SpHCS

We observed SpHCS structures bound to two different divalent metals. Analysis of synchatron radiation x-ray fluorescence scans detected Co(II) in the SeMet derivatized crystals, which was most likely incorporated into the protein from the Co(II) IMAC purification steps. The structures of the Zn(II) bound SpHCS/2-OG closed lid complex and the Co(II) bound SpHCS/2-OG open lid complex were solved by treating the Co(II)

IMAC purified enzyme with EDTA prior to gel filtration followed by the addition of 2 mM Zn(II) or Co(II), respectively during crystallization. Additionally, because HCS has been reported to be a Zn(II) dependent enzymes, SpHCS and its mutants were purified on a Zn(II) IMAC column for kinetic analysis. Both the EDTA treated Co(II) IMAC and Zn(II) IMAC purified SpHCS appeared to elute as a dimer at ~110 kDa on a superdex 200 gel filtration column and were judged to be essentially pure by SDS-PAGE (Figure 2.1). To verify the metal content of WT SpHCS used in crystallization trials and kinetic studies, we analyzed the enzyme using ICP-HRMS. SpHCS purified on a Zn(II) IMAC column had a Zn(II) content of 87 ± 5 %, whereas SpHCS purified on a Co(II) IMAC column and treated with EDTA retained only 8.4 ± 0.4 % Co(II).

The crystal structure of full-length (residues 1-418) SpHCS was solved by selenomethionine SAD phasing to 2.7 Å resolution in space group $P6_222$ (Table 2.2). The partially refined model of the SpHCS monomer was used in molecular replacement to determine the high resolution (2.24 Å) SeMet-SpHCS structure (PDB 3IVS). During refinement of this structure, the R-factors remained high, and it was discovered that SpHCS is not a perfect homodimer. Refinement in the lower symmetry space group $P6_2$ let us refine each monomer separately, which allowed for small differences in amino acid conformations between the two monomers. The SeMet-SpHCS dimer was then used as a molecular replacement model to solve the 2-OG bound complex structures. While screening for crystals of the SpHCS/2-OG complex, we discovered two different conformations (open and closed) of the lid motif (residues 320-333) that functions to gate access to the active site of SpHCS. In the closed lid complex (2.67 Å) (PDB 3IVT), clear electron density is seen for the lid motif, which obstructs the entrance of the active site. In contrast, electron density for the lid motif is missing in the open lid complex (2.72 Å) (PDB 3IVU) leaving the active site solvent exposed.

Crystal Structure of SpHCS

SpHCS forms a domain-swapped (34) homodimer within the asymmetric unit of space group $P6_2$ with a 46.7 kDa monomer being composed of two domains: an N-terminal catalytic domain and a C-terminal domain of mixed α-helical and β-sheet topology (Figure 2.2). The N-terminal domain (residues 1-300) consists of an N-terminal

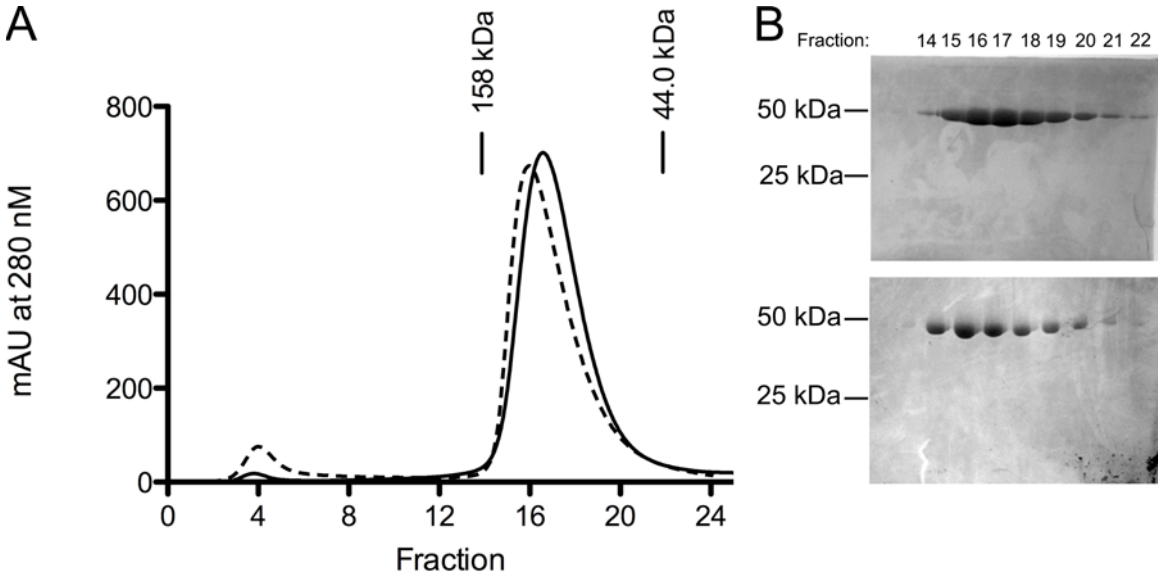

Figure 2.1 Purification of SpHCS. (A) Superdex 200 gel filtration chromatogram of SpHCS purified on a Zn(II) IMAC column (solid lined) and Co(II) Talon column followed by treatment with EDTA (dashed line). Molecular weight values for gel filtration standards are also depicted and demonstrate that SpHCS appears to elute as a dimer. (B) SDS-PAGE gels of the peak fractions from the Superdex 200 purifications of SpHCS (Zn(II) on the top and Co(II) treated with EDTA on the bottom). SpHCS migrates at approximately 50 kDa corresponding with the calculated molecular weight of the native protein (46.7 kDa).

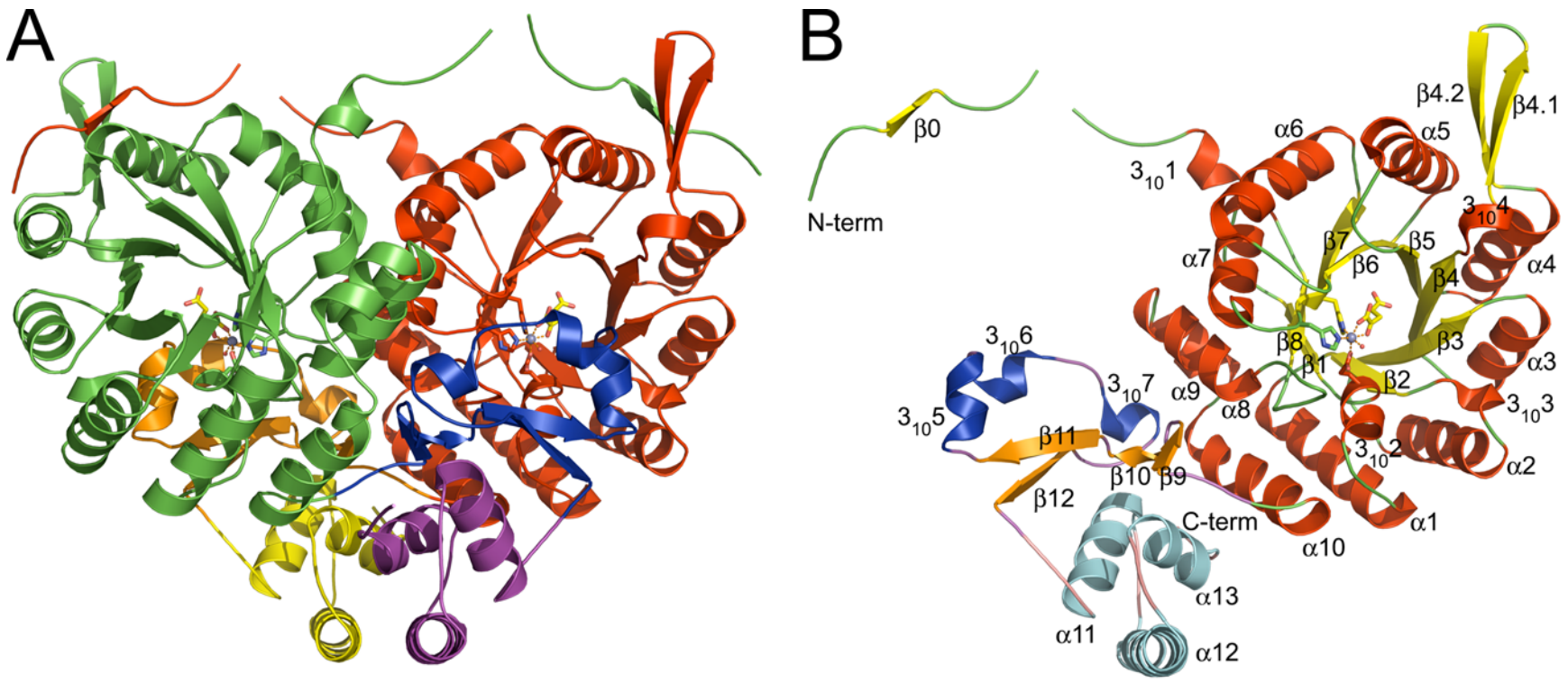

Figure 2.2 Crystal structure of SpHCS. (A) Ribbon diagram of the SpHCS homodimer bound to 2-OG (closed lid motif) with the N-terminal domain, C-terminal subdomain I, and C-terminal subdomain II of monomer A depicted in red, orange, and yellow, respectively, and of monomer B depicted in green, blue, and violet, respectively. The Zn(II) atom is modeled as a dark gray sphere and the bound 2-OG is rendered as sticks with yellow carbon atoms. **(B)** Ribbon diagram of the secondary structure of a monomer of SpHCS in complex with 2-OG with the secondary structure assigned following standard nomenclature for TIM barrel enzymes. The secondary structure is colored to distinguish between the N-terminal domain, C-terminal subdomain I, and C-terminal subdomain II.

extension (residues 1-34), with electron density only being present in the SpHCS/2-OG complexes and a canonical $(\alpha/\beta)_8$ TIM barrel (residues 35-300). The N-terminal extension is composed of a short β-strand (β0) followed by a 3_{10} helix ($3_{10}1$) in the SpHCS/2-OG complexes, however the extension preceding the 3_{10} helix is disordered in the free enzyme. Within the canonical $(\alpha/\beta)_8$ TIM barrel are additional secondary structural elements. Several short 3_{10} helices ($3_{10}2$-$3_{10}4$) are present throughout the α/β fold. Additionally, a 3_{10} helix followed by β-sheet hairpin (β4.1 and β4.1) forms between α4 and β4 in the SpHCS/2-OG complexes, whereas in the SpHCS free enzyme, this region remains disordered (see below). At the C-terminus of the N-terminal domain, two α-helices (α9 and α10) pack against helices α8 and α1 of the TIM barrel, respectively.

The C-terminal domain consists of two subdomains (Figure 2.2B). Subdomain I (residues 301-350) is of mixed topology and is composed of a short anti-parallel β-sheet (β9-β10) followed by a second parallel β-sheet (β11-β12), with the two β-strands separated by three 3_{10} helices ($3_{10}5$-$3_{10}7$). In the SpHCS free enzyme and closed lid 2-OG complex, $3_{10}5$ and $3_{10}6$ form the lid motif that prevents access to the active within the TIM barrel. Subdomain II (residues 351-405) forms a three-helix bundle (α11-α13), with the residues following α13 (406-418) being disordered in all of the SpHCS structures.

Both the N-terminal catalytic domain and C-terminal domain contribute to the dimer interface and act to stabilize the domain swapped homodimer (Figure 2.2A), which is assumed to be the biological unit based on the structure and elution size during purification (Figure 2.1). Dimerization buries an extensive area of ~5900 $Å^2$ per monomer, representing ~41 % of the total monomer surface. A large percentage of the total buried surface area is formed by the dimerization of the TIM barrel domains through interactions between α6-α10 helices of each monomer (Figure 2.2). The remainder of the interaction between the two monomers is formed by domain swapping of the N-terminal extension and the C-terminal domain. In the SpHCS/2-OG complexes, β0 in the N-terminal extension forms an anti-parallel β-sheet with β4.1 of the β-harpin between α4 and β4, whereas these regions are disordered in the SpHCS free enzyme.

The C-terminal domain also plays an important role in stabilizing the domain-swapped homodimer. Deletion of this region (residues 301-418) results in insoluble

protein, demonstrating the importance of this domain in maintaining the quaternary structure of SpHCS (data not shown). Both subdomain I and II of the C-terminal domain participate in dimerization. The two β-sheets along with the $3_{10}5$ and $3_{10}6$ helices in that make up the lid motif that make up subdomain I contact the neighboring monomer (Figure 2.2). However, in the open SpHCS/2-OG helices $3_{10}5$ and $3_{10}6$ are disordered, and this interaction is absent. The three helix bundle in subdomain II also contributes to the dimer interface with α12 and α13 packing against their counterparts in the adjacent monomer.

Structural Comparison of SpHCS and α-IPMS

After determining the structure of SpHCS, we sought to identify structural homologs of the enzyme by searching the Protein Data Bank using the 3D structure comparison server Dali (35). Using a full length SpHCS monomer, many structural matches were identified by Dali. However most of the structures were matches simply because of the commonality of the TIM barrel protein fold. The TIM barrel enzymes 3-hydroxy-3-methylglutaryl-CoA lyase (36), the aldolase-dehydrogenase DmpG/DmpF (37), and *M. tuberculosis* α-IPMS (14) shared the highest homology with SpHCS. The latter enzyme was identified as the top hit (Z-score 31.1), consistent with the predicted structural homology between SpHCS and α-IPMS and the analogous reactions catalyzed by these enzymes. The TIM barrel domains of α-IPMS (residues 73-357) and SpHCS (residues 36-298) align extremely well with a root mean square deviation (R.M.S.D.) in the main chain positions of 1.38 Å (Figure 2.3). The active site residues that coordinate to the divalent metal and that are involved in substrate binding and catalysis are also structurally homologous between the two enzymes (see below). There are a few differences in the fold of the TIM barrel between the enzymes nevertheless; SpHCS has a 3_{10}-helix following β2 and β-hairpin, which are both absent in α-IPMS.

In contrast to the TIM barrel catalytic domain, the C-terminal domain of SpHCS shares limited homology to the linker domain of α-IPMS. Subdomain I of SpHCS and α-IPMS are structurally similar with the exception of helices $3_{10}5$ and $3_{10}6$ of SpHCS being replaced by a single α-helix (α10) in α-IPMS (Figure 2.3). In addition, although

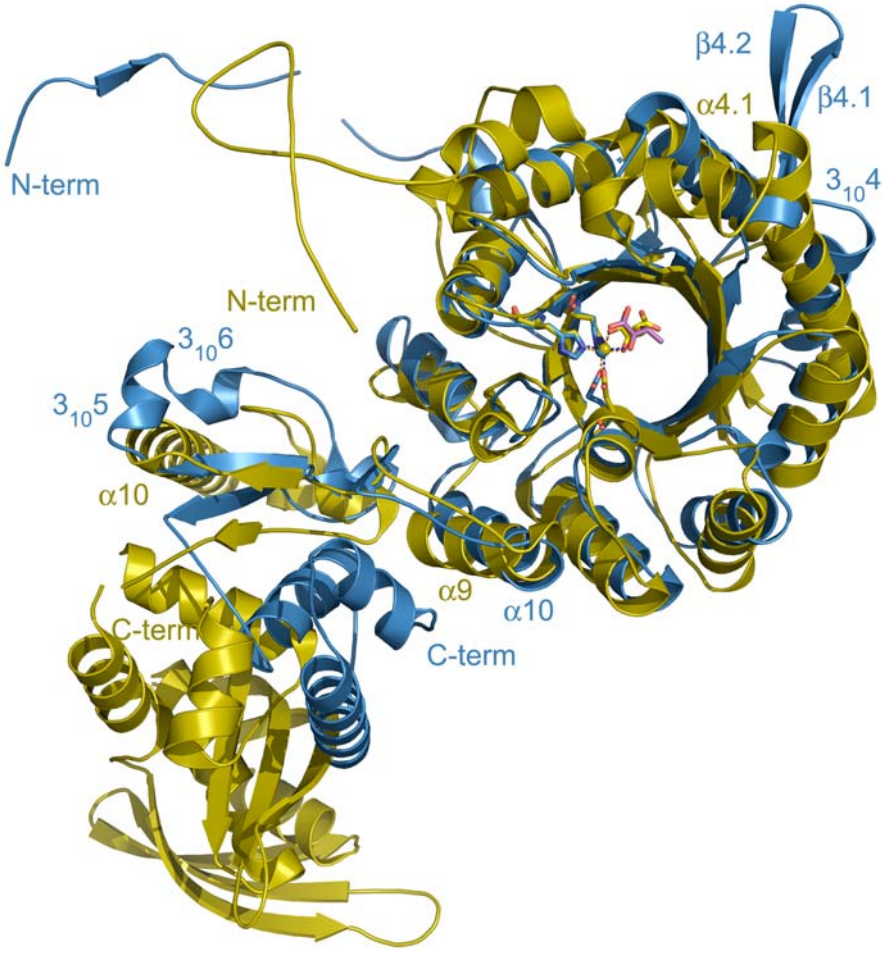

Figure 2.3 SpHCS superimposed with M. tuberculosis α-IMPS. A monomer of SpHCS (blue) in complex with 2-OG and overlaid with a monomer of α-IPMS (gold) bound to 2-OIV. Coordination of the Zn(II) metal site in SpHCS and in α-IPMS is depicted as dashed orange and blue lines, respectively, while 2-OG and 2-OIV are depicted with yellow and magenta carbon atoms, respectively.

subdomain II of SpHCS and α-IPMS are both composed of three helix-bundles, they are oriented differently in space relative to the TIM barrel. However, the largest difference between the two structures in the presence of a βββα fold regulatory domain at the C-terminus of α-IPMS that is absence in SpHCS. In α-IPMS, the regulatory module functions to allosterically bind the feedback inhibitor leucine. In SpHCS, feedback inhibition by lysine has been reported to be competitive versus the substrate 2-OG, suggesting that lysine binds within the active site (*38, 39*). Lack of this regulatory domain in SpHCS indicates that the two enzymes may utilize distinct regulatory mechanisms for feedback inhibition (see Chapter 3).

Active Site and 2-OG Binding

The active site of SpHCS is located at the C-terminal end of each $(\alpha/\beta)_8$ in the interior of the TIM barrel (Figure 2.2B) and is identifiable by the presence of a divalent metal. In the structures reported here, the divalent metal cation is either Co(II) or Zn(II), (Table 2.2) which coordinates in an octahedral geometry to the side chains of Glu44, His224 and His226 is SpHCS, to the C1 carboxylate and the 2-oxo carbonyl of 2-OG; and to a water molecule (Figure 2.4A). 2-OG is further stabilized through a network of hydrogen bonds and salt bridge interactions with the protein. The C1 carboxylate of 2-OG hydrogen bonds to the hydroxyl group of Thr197 while the 2-oxo group forms a hydrogen bond with the guanidinium group of Arg43. The C5 carboxylate group of 2-OG also engages in several hydrogen bonds with the side chains of residues His103, Arg163 and Ser165 of SpHCS. The active sites and substrate binding orientation of SpHCS and α-IPMS are analogous, with the exception of the hydrophobic interaction the methyl groups of 2-OIV with Leu143 within the TIM barrel (Figure 2.4).

Upon 2-OG binding, a conformational change takes place within the catalytic domain of SpHCS. Superimposition of the active sites of the SpHCS free enzyme and 2-OG closed complex shows that the carboxylate groups of Asp123 and Glu222 rotate away from the center of the barrel to make room for the C5 carboxylate of 2-OG while Arg43, His103, Arg163 and Ser165 rotate inwards to form hydrogen bonds or salt bridge interactions with the substrate (Figure 2.5). This reorientation appears to coincide with global structural changes within the TIM barrel. Although the overall differences between

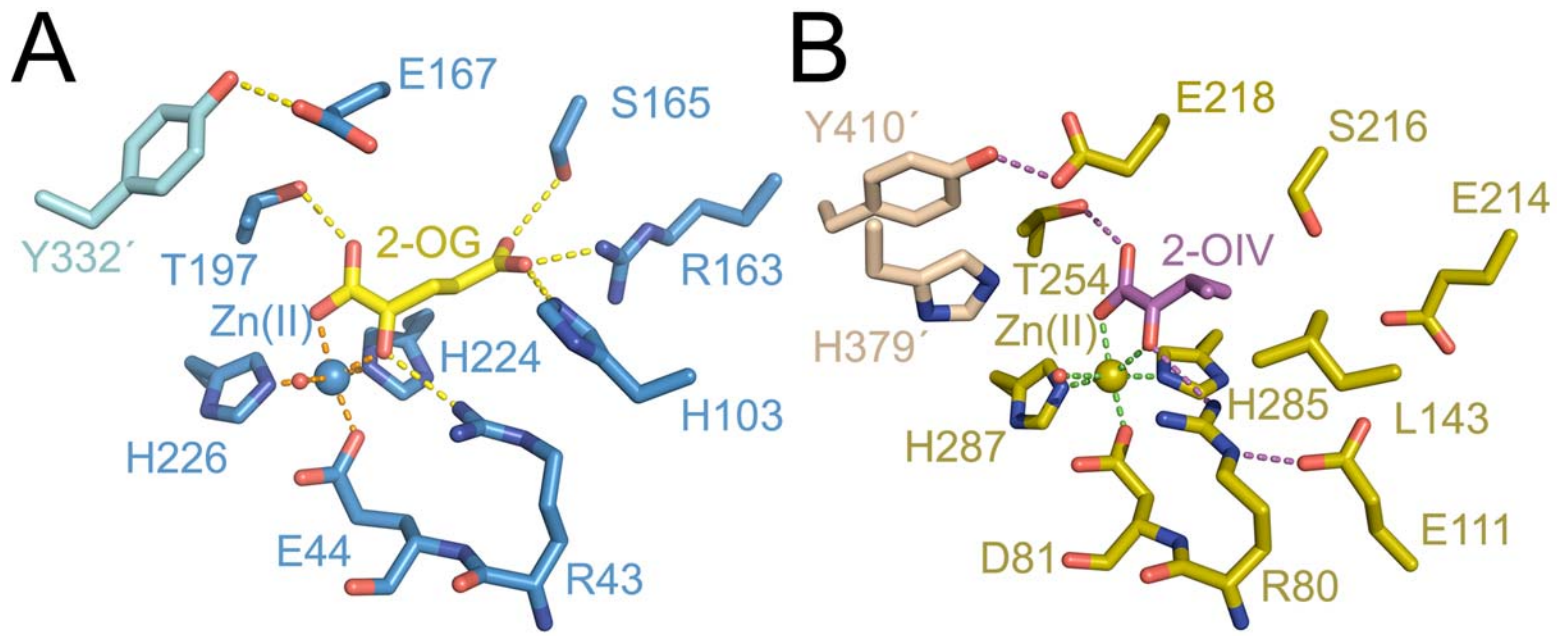

Figure 2.4 Active sites of SpHCS and α-IPMS. (A) Active site of SpHCS (closed lid conformation; blue carbon atoms) in complex with 2-OG (yellow carbons) and Zn(II) (blue). Orange and yellow dashes represent coordination of the Zn(II) ion and hydrogen bonding to 2-OG, respectively. **(B)** Active site of α-IPMS (gold carbons) in complex with 2-OIV (magenta carbons) and Zn(II) (gold). The coordination of the Zn(II) ion and hydrogen bonds to 2-OIV are colored green and magenta, respectively.

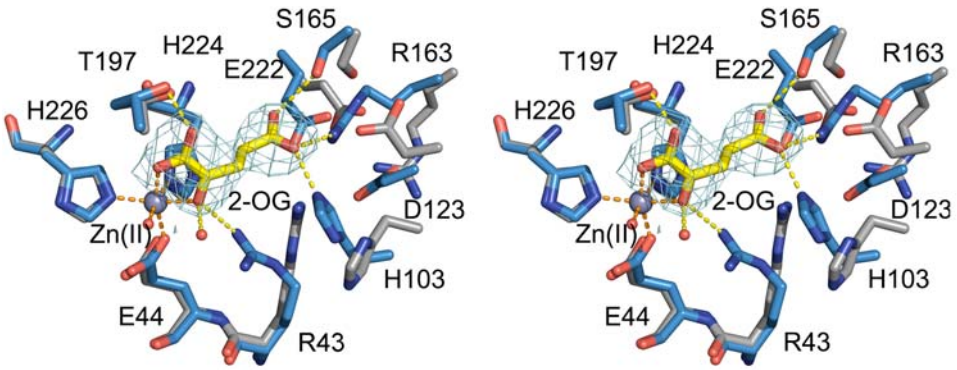

Figure 2.5 Stereoview of the active site of SpHCs 2-OG closed lid complex and SpHCS free enzyme. The SpHCS 2-OG closed lid complex (rendered as in figure 2.4) overlaid with the SpHCS apoenzyme (gray carbons). The Zn(II) ion and water molecules are represented as gray and red spheres, respectively. Electron density of the Fo-Fc simulated annealing omit map (contoured at 2.5 σ) corresponding to the 2-OG in the closed loop complex is depicted in cyan.

the catalytic domains of the free enzyme and 2-OG complex are modest with a R.M.S.D value of 1.25 Å for all aligned atoms, structural changes do occur in the linker between β4 and α4. This region is disordered in the free enzyme, however upon 2-OG binding, the linker becomes ordered and forms the $3_{10}4$ helix and the β4.1-β4.2 hairpin. Additionally, the first turn of helix α4 is unwound and the helix is pushed outward to accommodate the formation of the β-haripin. The formation of this region contributes to the ordering of the N-terminal extension with β0 in the N-terminal extension forming a β-sheet with the β-hairpin (Figure 2.6).

Kinetic Analysis of 2-OG Binding Mutants

To investigate the structural basis for the changes that occur upon 2-OG binding, we analyzed the residues involved in 2-OG binding. Steady state kinetic analysis of Zn(II)-bound SpHCS yielded a k_{cat} value of ~300 per min and K_M values for AcCoA and 2-OG of 10.7 ± 0.6 μM and 0.159 ± 0.015 mM, respectively (Figure 2.7 and Table 2.3). These values are comparable to those reported for other HCSs, including ScHCS Lys20 and TtHCS (k_{cat} = 63-92 min^{-1}, $K_{M(2\text{-}OG)}$ = 0.044-0.140 mM and $K_{M\ (AcCoA)}$ = 32-42 μM) (15, 40). We next measured the steady state kinetic parameters of conservative and alanine mutations of the active site residues that interact with the 2-OG (Figure 2.4). In addition, to demonstrate proper folding of inactive SpHCS mutants, circular dichroism spectra were taken of WT and inactive mutants (Figure 2.8). The spectra of the inactive SpHCS mutants were nearly superimposible with WT SpHCS illustrating that the loss of activity of these mutants is not due to misfolding.

Mutation of Thr97, which forms a hydrogen bond to the C1-carboxylate of 2-OG, to serine, resulted in a modest decrease in the catalytic efficiency (as defined by k_{cat}/K_M) compared to WT SpHCS due to a minor decrease in the turnover number. In contrast, a T197A substitution exhibited a 25 fold decrease in the k_{cat} value, whereas the T197V mutation abolished activity (Table 2.3). These results illustrate that the hydrogen bond between the Thr197 hydroxyl group and the C1-carboxylate group of 2-OG contributes to catalysis. Interactions between the 2-oxo carbonyl group of 2-OG are also important for efficient homocitrate formation. Alanine and glutamine and lysine substitutions of Arg43

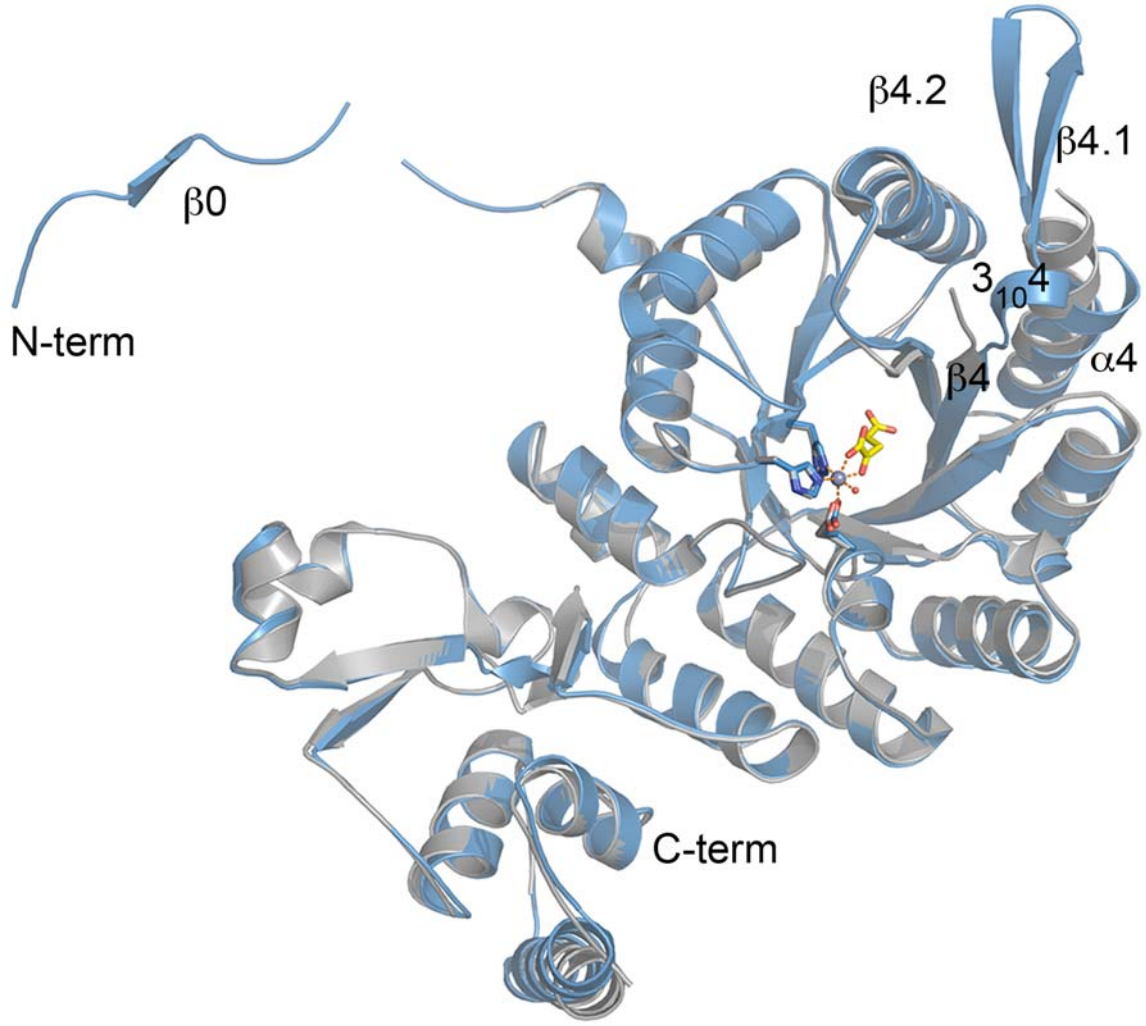

Figure 2.6 Superimposition of SpHCS 2-OG closed lid complex and SpHCS free enzyme. SpHCS 2-OG closed lid complex is denoted in blue with the corresponding monomer in the SpHCS apoenzyme in gray. The secondary structural elements that undergo conformational changes between the two complexes are denoted.

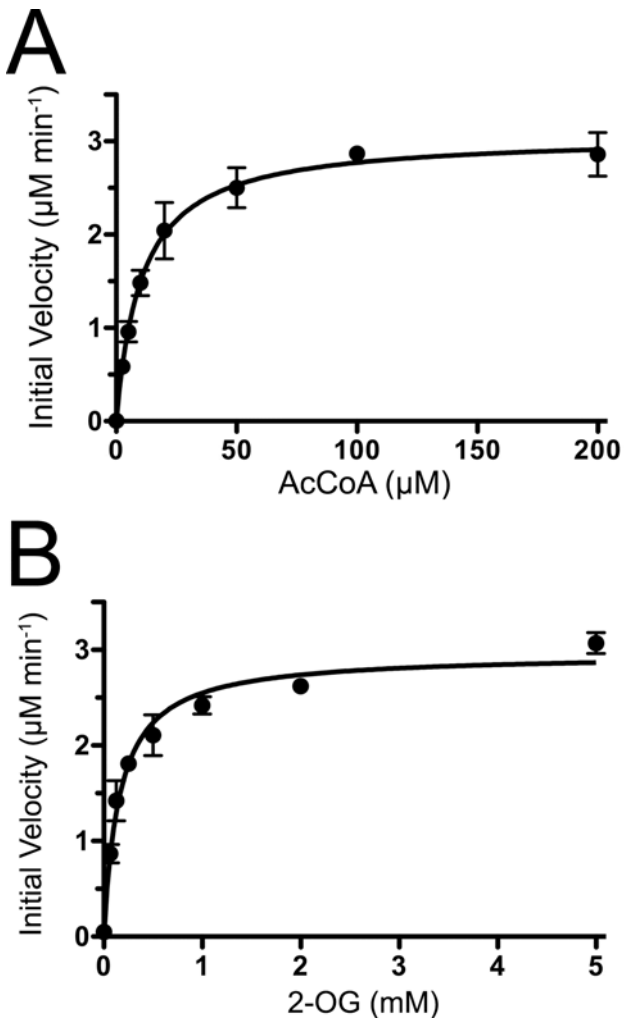

Figure 2.7 *In vitro* activity of SpHCS. (A and B) Michaelis-Menten plot of the initial velocity versus AcCoA concentration with 2-OG held at 5 mM**(A)** and 2-OG concentration with AcCoA held at 200 mM **(B)** for the formation of homocitrate catalyzed by WT SpHCS. Data points are the average of triplicate measurements, and the error bars represent one standard deviation.

Table 2.3 Kinetic analysis of WT SpHCS and its active site mutants.

	K_M AcCoA	k_{cat} varying AcCoA	k_{cat}/K_M	K_M 2-OG	k_{cat} varying 2-OG	k_{cat}/K_M
	μM	min^{-1}	min^{-1} μM^{1}	mM	min^{-1}	min^{-1} mM^{-1}
WT	10.7 ± 0.6[a]	299 ± 7	28.0 ± 1.7	0.159 ± 0.015	308 ± 4	1940 ± 190
R43A	N.A.	N.A.	N.A.	N.A.	N.A.	N.A.
R43K	N.A.	N.A.	N.A.	N.A.	N.A.	N.A.
R43Q	N.A.	N.A.	N.A.	N.A.	N.A.	N.A.
Q47A	57.6 ± 12.6	35.0 ± 0.1	0.608 ± 0.133	4.94 ± 1.28	33.5 ± 0.08	6.78 ± 1.76
E74A	N.A.	N.A.	N.A.	N.A.	N.A.	N.A.
E74Q	30.7 ± 3.0	44.5 ±1.4	1.45 ± 0.15	0.791 ± 0.081	46.7 ± 1.7	59.0 ± 6.3
H103A	35.2 ± 5.7	20.0 ± 0.9	0.568 ± 0.096	3.56 ± 0.61	18.2 ± 0.7	5.11 ± 0.35
R163A	N.A.	N.A.	N.A.	N.A.	N.A.	N.A.
R163K	146 ± 28[b]	33.9 ± 2.8[b]	0.232 ± 0.048	24.4 ± 4.3	26.1 ± 1.4[c]	1.07 ± 0.20[c]
R163Q	N.A.	N.A.	N.A.	N.A.	N.A.	N.A.
S165A	18.6 ± 2.3	158 ± 5.8	8.5 ± 1.0	0.536 ± 0.070	160 ± 6	298 ± 40
E167A	N.A.	N.A.	N.A.	N.A.	N.A.	N.A.
E167Q	N.A.	N.A.	N.A.	N.A.	N.A.	N.A.
T197A	7.44 ± 0.35	10.7 ± 0.1	1.44 ± 0.07	0.341 ± 0.083	11.9 ± 0.7	34.9 ± 8.7
T197S	6.00 ± 0.59	124 ± 3	20.6 ± 2.1	0.229 ± 0.034	137 ± 4	597 ± 91
T197V	N.A.	N.A.	N.A.	N.A.	N.A.	N.A.
Y332A	N.A.	N.A.	N.A.	N.A.	N.A.	N.A.
Y332F	40.0 ± 4.6	23.5 ± 0.8	0.59 ± 0.07	0.461 ± 0.070	20.7 ± 0.79	44.9 ± 6.9

N.A. No detectable activity measured using 100 nM mutant assayed with 200 μM AcCoA and 50 mM 2-OG.

[a]Errors are reported as the error in curve fitting.

[b]Values are approximate because the mutant is inhibited at AcCoA concentrations above 400 μM so saturation could not be achieved.

[c]Values were underestimated because the mutant is inhibited at AcCoA concentrations above 400 μM.

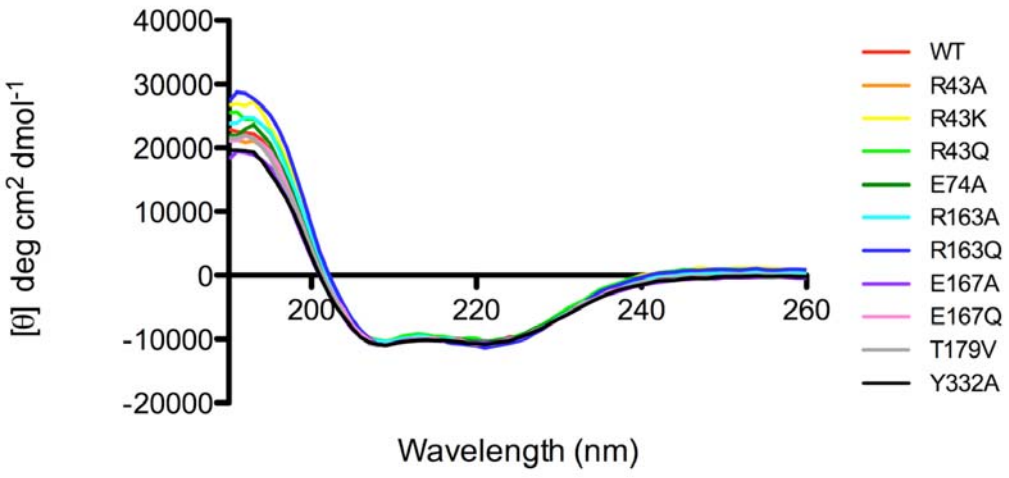

Figure 2.8. Overlay of the CD spectra of WT SpHCS and inactive mutants.

abolished activity suggesting the hydrogen bond between the 2-oxo atom of 2-OG and the guanidinium group of Arg43 is critical for catalysis.

Residues that interact with the C5 carboxylate group of 2-OG are also essential for substrate binding (Figure 2.4). Mutagenesis of Arg163 to alaine of glutamaine completely arrested activity, whereas H103A and R163K substitutions severally impaired catalytic efficiency. Mutation of His103 to alanine resulted in a reduced k_{cat}/K_M >370 fold compared to WT SpHCS by increasing K_M value for 2-OG (>20 fold) and reducing the turnover rate (>16 fold), while the R163K substitution caused a 200 fold reduction in catalytic efficiency by raising the K_M of 2-OG by 150 fold. Unexpectedly, the R163K mutation also increased the K_M for AcCoA by ~13 fold. This could be caused by the severely diminished affinity for 2-OG, which binds before AcCoA in the ordered Bi-Bi reaction mechanism (9). In contrast, an alanine mutation of Ser165 resulted in a modest decrease in the catalytic efficiency compared to WT SpHCS (Table 2.3). Together, these results illustrate that the residues that interact with the C5 carboxylate group of 2-OG are vital for proper substrate binding within the active site.

In Vivo Analysis of 2-OG Binding Mutants

To evaluate the effects these SpHCS mutations *in vivo* yeast growth assays were performed. For these studies, the two genes encoding the ScHCS homologs *LYS20* and *LYS21* were deleted in *S. cerevisiae* to generate a *lys20Δ lys21Δ* double deletion strain. This strain exhibits lysine auxotrophy, but displays robust growth on lysine-supplemented media (Figure 2.9). Next, we tested if expression of SpHCS encoded by *lys4*$^+$, which is >80 % identical to ScCHS Lys20 and Lys21 (Figure 2.10), could rescue lysine auxotrophy by transforming the double deletion strain with a vector of the *lys4*$^+$ gene under the control of the *LYS20* promoter. Transformants expressing either LYS20 or *lys4*$^+$ were able to restore growth on media lacking lysine, whereas those transformed with vector alone were inviable on lys- media, demonstrating that *lys4*$^+$ complements the loss of ScHCS Lys20 and Lys21 (Figure 2.9). Finally we determined whether SpHCS 2-OG binding mutants had the ability to complement growth on lysine deficient media. As controls, we first demonstrated that the 2-OG binding mutants expressed at comparable levels to WT SpHCS by protein immunoblotting and confirmed that the

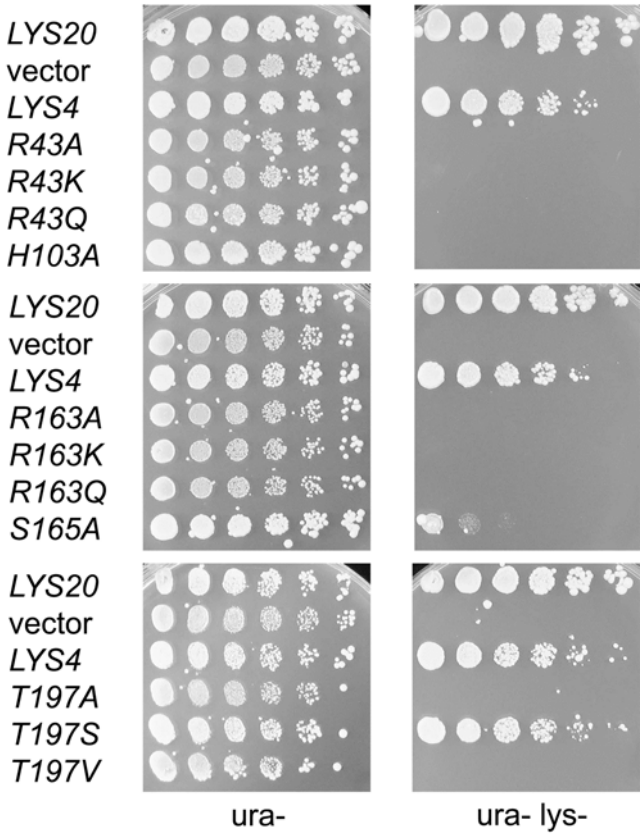

Figure 2.9 *In vivo* yeast growth assays of *LYS4* and *LYS4* 2-OG binding mutants.

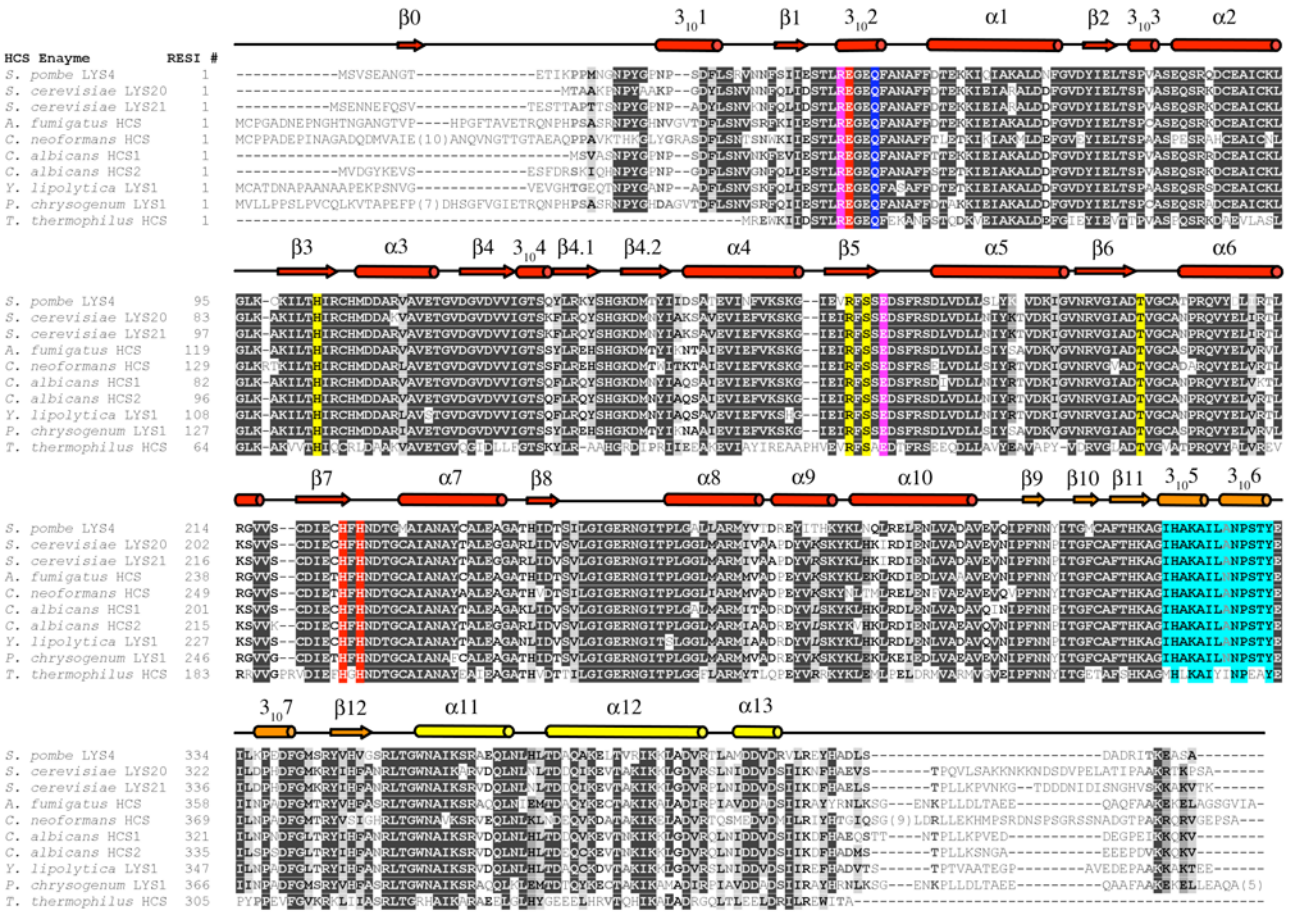

Figure 2.10 Sequence alignment of HCSs with the secondary structure of SpHCS 2-OG closed lid complex. The secondary structure of the TIM barrel, C-terminal subdomain I and C-terminal subdomain II are depicted in red, orange and yellow respectively. Residues involved in metal coordination, 2-OG binding, and binding to the acetyl oxygen atom of AcCoA are highlighted in red and yellow and blue respectively while residues that act as the catalytic acid and base along with the lid loop motif are highlighted in magenta and light blue respectively.

mutants behave in a recessive manner when co-expressed in WT cells (data not shown). All of the 2-OG binding mutations, with the exception of the SpHCS conservative T197S mutant, and to a lesser extent the S165A mutant failed to grow on lysine deficient media (Figure 2.9). These results are in agreement with our *in vitro* kinetic studies where the T197S and S165A mutants only exhibited a three-fold and seven-fold reductions in catalytic efficiency, respectively compared to WT SpHCS (Table 2). In contrast, the other 2-OG binding mutants had more severe defects in catalytic efficiency and failed to restore growth on media lacking lysine.

Putative Functions of the Lid Motif

An interesting finding that arose during our studies of the SpHCS structures is the presence of a lid motif that encloses over the active site of the enzyme. The lid motif is a conserved feature of fungal HCSs (Figure 2.10) but is absent in the structurally related α-IPMS. The lid motif is made up of the $3_{10}5$-$3_{10}6$ helices in subdomain I of the C-terminal domain, and when closed participates in domain-swapping by completely burying the substrate 2-OG in the active site of the neighboring monomer. In contrast, the motif is disordered in the SpHCS/2-OG open lid complex, which leaves the active site solvent exposed permitting free exchange of the substrate 2-OG and water molecules (Figure 2.11A). Alignment of the active sites of the open and closed 2-OG SpHCS complexes shows that the lid's disorder does not cause large changes in the residues that coordinate 2-OG (Figure 2.11B). This is consistent with the observation that the lid motif does not form direct contacts with 2-OG. Instead several water molecules are lodged between 2-OG and the lid motif, which are presumably trapped during lid closure.

Comparison of the lid loop motif in the open and closed structures reveals that the lid closure is maintained by a network of hydrogen bonds in the neighboring monomer with the hydroxyl group of Y332′ along with the backbone amide nitrogens of Leu326′ and Ala327′ (the (′) denotes residues in the lid motif of the neighboring monomer) forming interactions with Glu167 (Figure 2.12A). In the open lid complex residues 323′-329′ in the lid motif are disordered, resulting in the loss of the hydrogen bond interactions of Leu326′ and Ala327′. Additionally, the phenol side chain of Try332′ in the

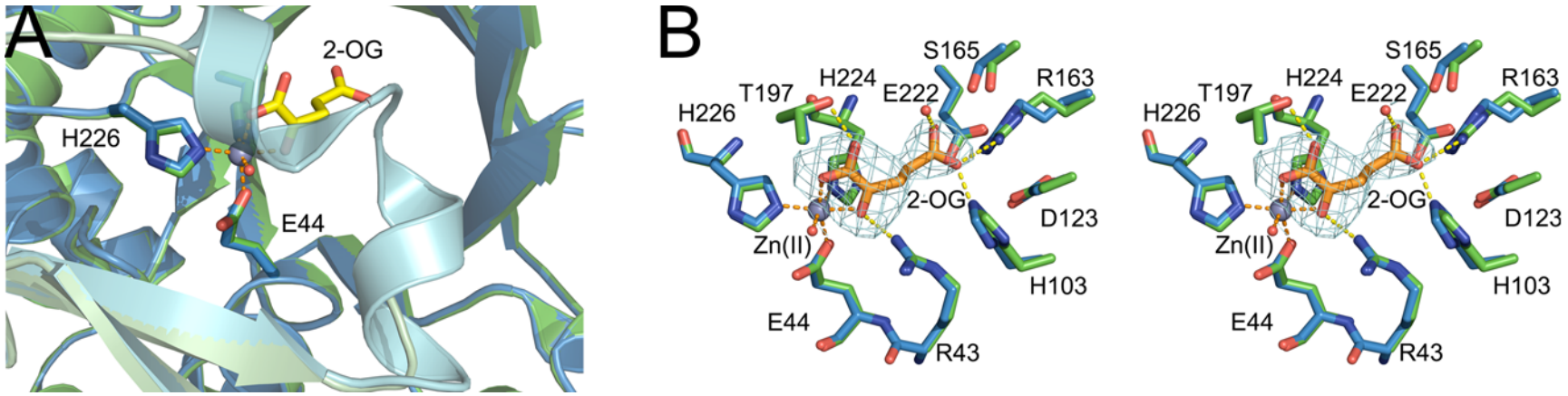

Figure 2.11 The SpHCS/2-OG open lid complex. (A) Structural superimposition of the SpHCS/2-OG complexes with the open lid motif (monomer A is green and monomer B is pale green) and the closed lid motif (monomer A is blue and monomer B is cyan). The 2-OG and Zn(II) ion of the closed lid structure are depicted in yellow carbons and gray, respectively. **(B)** Stereoview of the active site of SpHCS/2-OG open lid complex (green carbon atoms with 2-OG rendered with orange carbons) overlaid with the SpHCS/2-OG closed lid complex (blue carbons). Electron density for the F_o-F_c simulated annealing omit map (contoured at 2.0 σ) corresponding to the 2-OG in the open lid complex is shown in cyan. The orange and yellow dashes represent coordination of the Zn(II) ion and hydrogen bonding to 2-OG, respectively.

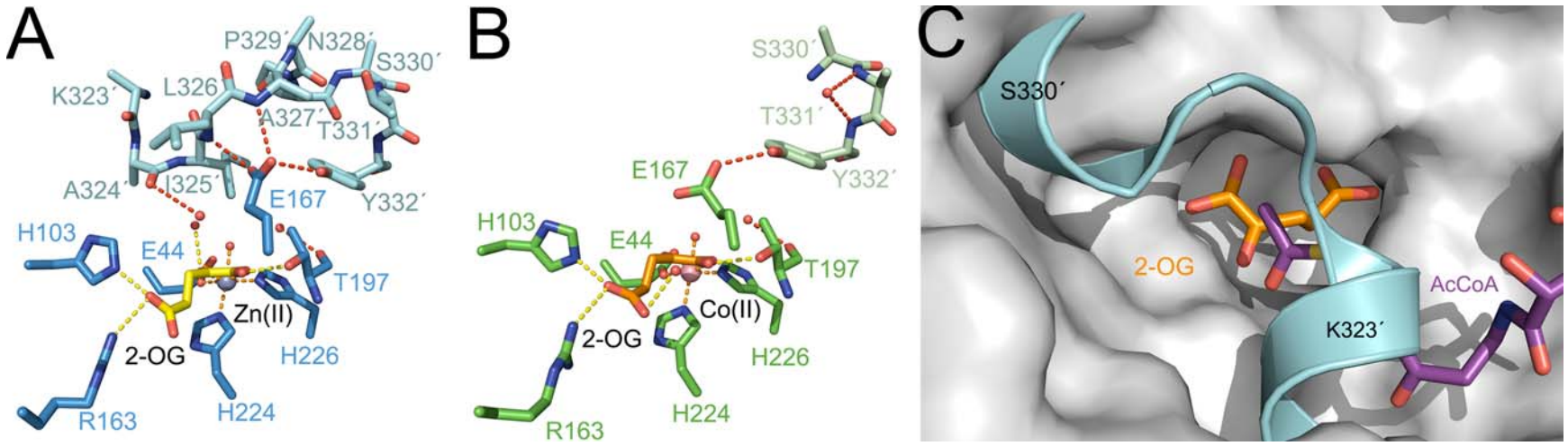

Figure 2.12 The lid motif of SpHCS (A, B) Comparisons of the active site and lid motif of the SpHCS/2-OG open and closed lid complexes. Monomer A (blue carbons) and B (cyan carbons) of the closed lid complex are depicted with the Zn(II) ion (gray) and 2-OG (yellow carbons) **(A)**, whereas monomer A (green carbons) and B (light green carbons) of the open lid complex are illustrated with the Co(II) ion (pink) and 2-OG (orange carbons) (D). Dashed lines denoted the coordination of the metal ion (orange), hydrogen bonding to 2-OG (yellow), and hydrogen bonding within the lid motif (red). Residues in the lid motif that lack interpretable side chain electron density are modeled as alanines, while the side chain of Tyr332 in the open lid complex **(B)** is modeled with an occupancy of 0.5. **(C)** Model of a ternary complex of SpHCS bound to 2-OG (orange carbons) and AcCoA (violet carbons). The lid motif of the SpHCS/2-OG closed lid complex (cyan) is superimposed on the gray surface of the SpHCS/2-OG open lid complex.

open complex is only partially ordered and is modeled with occupancy of 0.5. The hydroxyl group of Tyr332′ still maintains its hydrogen bind with the side chain of Glu167, but these residues adopt an alternative conformation over the 2-OG binding site presumably orienting the carboxyl group of Glu167 for base catalysis of the acetyl group of AcCoA (Figure 2.12B) (see below).

In addition to gating access to 2-OG, the lid motif may also function to regulate AcCoA binding to SpHCS. We were unsuccessful in obtaining an SpHCS ternary complex with 2-OG and either CoA or acetonyl-CoA or with the inactive E167Q mutant with 2-OG and AcCoA, therefore we modeled a SpHCS Michaelis complex with 2-OG and AcCoA based on the superimposition of the coordinates of the 2-OG open complex and the previously reported model of the α-IPMS/2-OIV/AcCoA ternary complex (14). The model shows a groove in the enzyme's surface adjacent to the active site where the pantetheine arm of AcCoA could bind (Figure 2.12C). Superimposition of the AcCoA-bound model with the closed SpHCS/2-OG complex reveals that the lid motif occupies the same space as the modeled AcCoA, implying that the lid motif must be inherently flexible to accommodate AcCoA binding. Together, these findings imply that the lid motif serves as the gatekeeper to regulate substrate binding to SpHCS.

Catalytic Reaction Mechanism

The catalytic mechanism of HCS has been proposed to proceed via a mixed Claisen condensation reaction (10) (Scheme 2.2). In this reaction mechanism, there is first an ordered binding of the substrate 2-OG followed by AcCoA, which is consistent with kinetic studies of ScHCS Lys20, and the spatial arrangement of the substrates in the modeled ternary complex. A general base then abstracts a proton from the methyl group of AcCoA to generate an enol (or enolate). The enol/enolate nucleophile then attacks the C2 carbonyl carbon of 2-OG to form the alkoxide of homocitryl-CoA, which is protonated by a catalytic acid to generate homocitryl-CoA. The water molecule bound to the active site divalent metal ion has been proposed to subsequently hydrolyzes the thioester bond homocitryl-CoA yielding the products CoA and homocitrate. A similar reaction mechanism is thought to occur for α-IPMS (14).

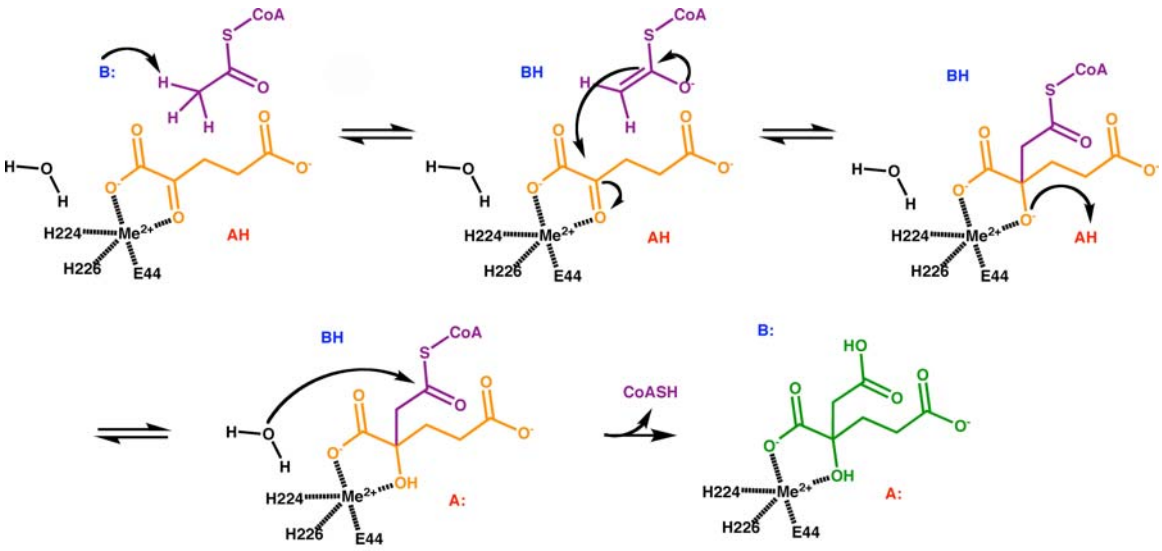

Scheme 2.2 Catalytic mechanism of SpHCS. The 2-OG and AcCoA substrates are depicted as in Figure 2.11C and homocitrate illustrated in green.

The SpHCS/2-OG/AcCoA ternary complex model gives insights into the residues implicated in homocitrate synthesis (Figure 2.12). The AcCoA is arranged in the active site so that its acetyl group is located near the C2 carbon of 2-OG where nucleophilic attack by the enolate occurs. Many residues that are conserved in HCS (Figure 2.10) and that are structurally analogous in α-IPMS surround the AcCoA acetyl group, implicating them in catalysis. In the SpHCS/2-OG/AcCoA ternary model, the carbonyl oxygen of the acetyl group of AcCoA is within hydrogen bond distance to the amide side chain of Gln47 and to the guaidinium group of Arg43, which also hydrogen bonds to 2-OG. A similar model of AcCoA binding has been proposed for α-IPMS where the positively charged side chain for the corresponding Arg80 stabilized both AcCoA and 2-OIV (14). The hydrogen bonds to Gln47 and Arg43 in SpHCS also stabilize the enol tautomer of AcCoA, promoting nucleophilic attack of the C2 atom of 2-OG. In the modeled complex, the methyl group of AcCoA is located ~3 Å from the carboxylate group of Glu167, which is proposed to function as the catalytic base that deprotonates the methyl group of AcCoA. The orientation of the side chain of Glu167 is stabilized by hydrogen bonding to the hydroxyl group of Tyr332′ in the adjacent monomer. This glutamate-tyrosine dyad is conserved in HCSs (Figure 2.10) and in α-IPMS (residues E218-Y410′) (Figure 2.4B) and has been proposed to position the glutamate's carboxylate group for base catalysis in both enzymes (14, 15). Following enolization of AcCoA, the enol/enolate nucleophile attacks the C2 carbonyl carbon of 2-OG to form homocitryl-CoA through the formation of a carbon-carbon bond (Scheme 2.3 and Figure 2.13). The C2 center becomes electrophilic due to the polarization of the 2-oxo atom of 2-OG through its coordination to the metal ion and hydrogen bond to the guanidinium cation of Arg43. In the SpHCS structures, the conformation of the Arg43 side chain is maintained through a hydrogen bond to Gln47 and salt-bridge interaction with Glu74 (Figure 2.13). Arg43 and Glu74 of SpHCS are conserved in HCSs (Figure 2.10) and structurally invariant in α-IPMS, suggesting a role for them in catalysis.

In Vitro and *In Vivo* Activity of Residues Implicated in Catalysis

To better understand the functions of the residues described above, we assayed

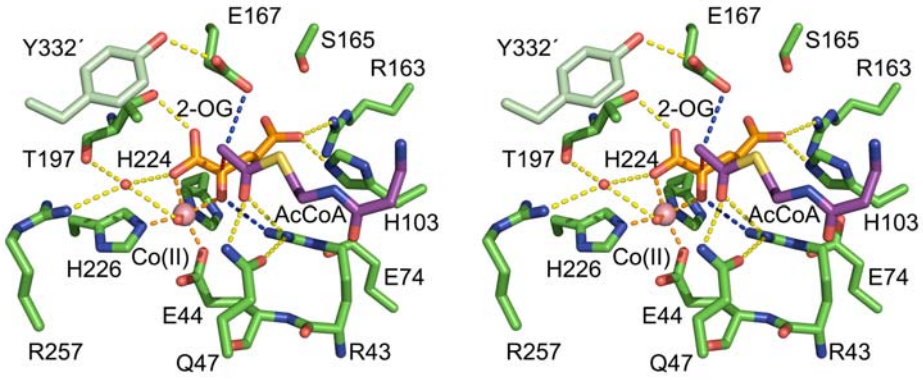

Figure 2.13 SpHCS ternary complex model. Stereoview of the active site of the modeled SpHCS ternary complex with 2-OG and the panetheine arm of AcCoA rendered as in Figure 2.11C. Dashed lines represent coordination of the Zn(II) ion (orange), hydrogen bonding to 2-OG (yellow), hydrogen bonding to the putative catalytic residues (blue) and the direction of the nucleophilic attack from the enolate tautomer of AcCoA to the C2 atom of 2-OG (red).

the *in vitro* and *in vivo* activities of conservative and alanine catalytic mutations (Table 2.3 and Figure 2.14). First, we examined the effects of mutations of the putative catalytic base Glu167, and the adjacent Tyr332′ in SpHCS (Figure 2.13). Both alanine and glutamine substitutions of Glu167 abolish activity *in vitro,* which is consistent with the idea that this residue acts as the catalytic base in enolization of AcCoA. This also agrees with the >1000 fold decrease in k_{cat} reported for alanine and glutamine mutations of the corresponding residues Glu155 in ScHCS Lys20 (15). Mutation of Tyr332′, which forms a hydrogen bond with Glu167, also disrupted activity. No detectable activity was observed for the Y332A mutation while the turnover rate of the Y332F mutation was reduced by ~13 fold with only modest increases in the K_M values for each substrate compared to WT SpHCS. In *vivo plate* growth assays using the *S. cerevisiae lys20Δ lys21Δ* deletion strain demonstrated that both the SpHCS Glu167 and Tyr332′ mutations were unable to rescue growth on lys- media (Figure 2.14), consistent with the *in vitro* kinetic defects of these mutants.

We also examined the effects mutations of Arg43, Gln47 and Glu74 had on homocitrate production. As discussed previously, Arg43 mutations to alanine, glutamine and lysine abolished activity *in vitro* and *in vivo* (Table 2.3 and Figure 2.9), demonstrating that the guanidinium group of Arg43 is vital for catalysis. Substitutions of Gln47 and Glu74, which hydrogen bond to Arg43 also reduced enzymatic activity (Figure 2.14). An alanine substitution of Glu74 in SpHCS abrogated activity *in vitro,* while the E74Q mutation resulted in a moderate decrease in the turnover and slight increase in the K_M values for 2-OG and AcCoA in comparison to WT enzyme (Table 2.3). An alanine mutation of Q47 resulted in even more elevated (5 fold for AcCoA and 30 fold for 2-OG) K_M values. Substitution of the Gln47 side chain may have resulted in increased K_M values by weakening hydrogen bonding to the acetyl group of AcCoA in the ternary complex and by perturbing the orientation of Arg43 which hydrogen bonds to 2-OG. Like the SpHCS Glu167 and Tyr332 mutants the Arg43, Gln47 and Glu74 mutations failed to grow on lysine deficient media when transformed into the double deletion strain (Figure 2.9 and 2.14), demonstrating the importance of these residues in homocitrate synthesis *in vivo*.

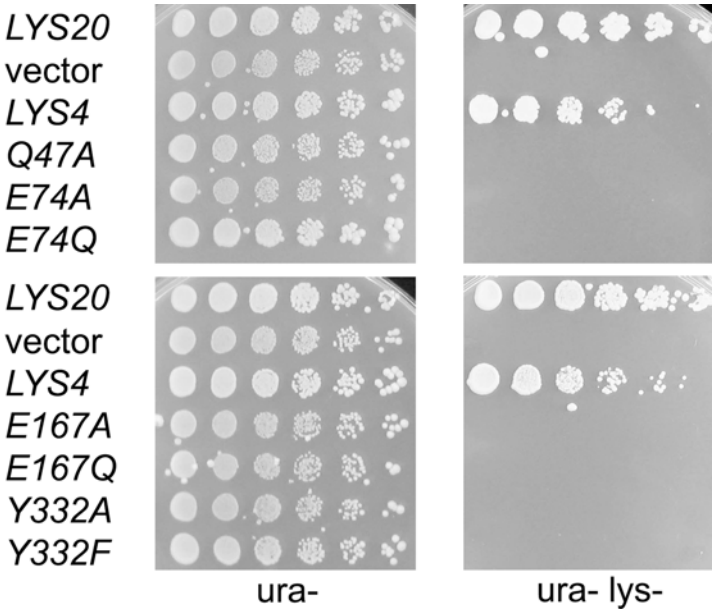

Figure 2.14 *In vivo* yeast growth assays of the *LYS4* mutants implicated in catalysis.

DISCUSSION

Residues Implicated in Base Catalysis

The structures of SpHCS presented here yield new insights into the basis of substrate binding and catalytic mechanism of HCSs. Additionally, our results highlight the similarities and differences between HCSs and other enzymes that catalyze mixed Claisen condensation reactions including α-IMPS, MS and CS. Recent studies have proposed that a glutamate-histidine dyad in α-IPMS (Glu218-His279′) and ScHCS Lys20 (Glu155-His309′) participates in base abstraction of the methyl group of AcCoA (14, 15). In α-IPMS, the side chains of Glu218 and His-279′ are close enough to deprotonate the acetyl group of AcCoA in the modeled IPMS/2-OIV/AcCoA ternary complex (14). A similar role has been proposed for Glu115-His309′ in ScHCS Lys20 (15). However, the structure of SpHCS reveals that His321′ (corresponding to His309′ in ScHCS) is located in helix $3_{10}5$ within the lid motif (Figure 2.10), which is disordered in one or the two monomers of the 2-OG open complex used to make the ternary model. In monomer B of the 2-OG open complex, clear electron density is seen for His321′, however the side chain of this residue is located ~13 Å away from the Glu-167 carboxylate group. Similar distances between these two residues are also observed in the free enzyme and the SpHCS/2-OG open lid complex. Although this distance is too large to form a histidine-glutamate dyad, upon AcCoA binding it is possible that a conformational change in the lid motif could take place that would bring the side chains of residues Glu167 and His321′ close enough to act in base catalysis. Consistent with this model, a H321A mutation decreased the activity by more than 200-fold compared to WT SpHCS (data not shown) in agreement with His309 mutations that affect the activity of ScHCS Lys20 (15). Alternatively, mutations of residues within the lid motif, such as His321′ and Tyr332′, might disrupt substrate binding by altering local dynamics in the conformation of the lid motif without directly affecting the chemical steps in catalysis. Further studies are needed to determine whether a histidine-glutamate dyad participates in base catalysis in HCS.

Residue Implicated in Acid Catalysis

There is a general consensus that the conserved glutamate residue is involved in base catalysis in HCS and α-IPMS (14, 15), however the identity of the catalytic acid in the reaction mechanisms of these enzymes remains unknown (Scheme 2.2). Our structural and biochemical studies suggest that Arg43 may fulfill this role by protonating the alkoxide of homocitryl-CoA. Although it is unusual for an arginine guanididium cation to act as a proton donor due to its high pK_A value, several lines of evidence support the role for Arg43 in acid catalysis. First, there are no other ionizable residues or solvent molecules in the active site of the ternary complex model that are located within a distance to the 2-oxo atom of 2-OG to function as catalytic acid, unless a large conformation change occurs within the TIM barrel upon AcCoA binding (Figure 2.13). Additionally, Arg43 is invariant in the HCS family (Figure 2.10) and mutation of this residue completely abolishes activity (Table 2), illustrating the importance of this residue in substrate binding and/or catalysis. Third, the pK_A value of an alkoxide ion is greater than 12.5, favoring protonation by the guanidinium group of Arg43 (aqueous pK_A = 12.5). Fourth, a recent review has described a role for arginine in acid-base catalysis for several enzyme reaction mechanisms (41). For example, in soluble fumarate reductase, an arginine residue (Arg402) has been reported to protonate fumarate to form succinate during flavin-dependent reduction (42). Finally, the close proximity of the divalent metal ion to the Arg43 guanidinium group (~5 Å) may contribute to reducing the residue's pK_A value promoting acid catalysis. Collectively, these observations suggest a role for Arg43 as the proton donor, however it is also possible that an acid-catalyzed step is not required in the reaction mechanism of HCS. Instead, the alkoxide intermediate may remain deprotonated during the subsequent steps in catalysis, similar to the mechanism of *E. coli* malate synthase in which the arginine residue (Arg338) that hydrogen bonds to aldehyde oxygen of glycoxylate was shown not to participate in proton transfer (Figure 1.3) (12, 13). Future studies are needed to determine whether the reaction mechanism of HCS occurs via an acid-catalyzed step, and if so, whether the structurally conserved arginine acts as the catalytic acid in protonation of the alkoxide intermediate.

Comparison of HCS with α-IPMS and Citrate Synthase

Although the HCS and α-IPMS are structurally similar and catalyze analogous reactions, the mechanisms by which their activities are regulated are distinct. Among the most noticeable differences are the relative accessibilities of their active sites. In α-IPMS, the entrance of the TIM barrel is solvent-exposed, suggesting that the enzyme can accommodate the binding of the substrates 2-OIV and AcCoA within its active site (Figure 2.3). In contrast, the entrance of the TIM barrel in SpHCS is effectively blocked by the flexible lid motif that gates access of 2-OG to the active site and competes with AcCoA binding to the enzyme (Figure 2.11B and 2.11C). The closed lid conformation is stabilized by hydrogen bonding to the carboxylate group of Glu167, illustrating its dual roles in catalysis and in regulating substrate access to the active site. The intrinsic flexibility of the lid motif may serve a regulatory function by interacting with factors that control its open or closed states, thus governing the rate of homocitrate synthesis and the metabolic flux through the AAA pathway.

In contrast, the structural similarities along with the details of the catalytic mechanisms of HCS and α-IPMS are distinct from those of citrate synthase, which catalyzes the Claisen condensation of oxaloacetate and AcCoA to yield citrate and CoA. Citrate synthase functions as a homodimer with each monomer composed of two domains that are predominately α-helical, whereas HCS and α-IPMS adopt a TIM barrel fold (14, 43, 44). The active site of citrate synthase is located between the two domains of the each monomer with arginine and histidine residues forming hydrogen bonds and salt bridge interactions with the substrate oxaloacetate. This substrate binding mode is different from HCS in which 2-OG is bound within the TIM barrel through coordination to the divalent metal center and through basic and polar amino acids (Figure 2.4A). Furthermore, there are differences in the residues involved in acid-base catalysis in the Claisen condensations reactions catalyzed for each enzyme. In citrate synthase an aspartate residue (Asp375) functions the catalytic base in deprotonation of AcCoA to initiate the condensation reaction and a histidine residue (His320) acts as the catalytic acid to protonate the alkoxide intermediate of citryl-CoA (Figure 1.2) (11, 44). In contrast, our structural and functional studies of SpHCS suggest that Glu167 functions as the catalytic acid, whereas Arg43 may participate in acid catalysis. Additionally, there are major

differences in the conformational changes that occur upon substrate binding in citrate synthase and HCS. Citrate synthase can exist in an open and closed form with the binding of oxaloacetate inducing closure of the enzyme which then stimulation AcCoA binding and catalysis (43, 44). In HCS, a large-scale conformational change upon substrate binding does not take place. Instead the lid motif in HCS appears to function as a flexible gate that regulates substrate binding (Figure 2.11), and conformational changes in the TIM barrel are localized to the β4-α4 region where a β-haripin forms upon 2-OG binding (Figure 2.6). In summary, the structure and catalytic mechanisms of citrate synthase and HCS are quite different providing evidence for the molecular evolution of two different mechanisms for the catalysis of Claisen condensation reactions using two closely related 2-oxo acid substrates.

HCS as an Antifungal Target

The enzymes in the AAA pathway have been proposed as potential targets for antifungal inhibitors. HCS, in particular, represents an excellent target for inhibition because it catalyzes the first and committed step in the pathway, and also functions in controlling the metabolic flux through the pathway as it is feedback inhibited by L-lysine (8). The loss of activity exhibited by the majority of the *lys4*$^{+}$ mutants *in vivo* further emphasizes the importance of HCS in maintaining fungal viability in lysine deficient conditions (Figure 2.8 and 2.14). Our structural and functional characterization of SpHCS provides a platform for developing selective inhibitors to HCS. The enzyme active site has a conserved divalent metal ion and a number of polar and charged residues with which small molecules may interact. Additionally, to maximize interactions with the active site and surrounding surface, bi-substrate analog inhibitors that mimic homocitryl-CoA could be synthesized. However, efforts to rationally design inhibitors must account for the flexibility of the active site residues that bind 2-OG as well as the movement of the lid motif that regulates access to the active site. Small molecules that are rationally designed or identified in high-throughput screening may take advantage of the conformational flexibility of HCS to discover potent inhibitors that may act as lead compounds for the development of new antifungal drugs.

ACKNOWLEDGEMENTS

I would like to recognize Jean-François Couture for cloning the SpHCS/pHIS2 vector, developing the purification protocol, and for finding the initial PEG 400, Mg acetate crystallization condition. I wish to acknowledge Lorraine Pillus and her graduate student Erin Scott for generating the *lys20Δ lys21Δ* double deletion strain and for cloning the *lys4*$^{+}$ gene into the pLP2211 vector. Additionally, Erin transformed the WT *lys4*$^{+}$/pLP2211 and mutant strains into the *lys20Δ lys21Δ* deletion strain and assayed the transformants for growth. I would also like to thank John Woodward at the Sanger Institute for providing the genomic clone of *lys4*$^{+}$ and John Aris for supplying the yeast HCS antibody. I thank Elizabeth Townsend and Corey Burbank for assistance in protein purification and in preparing site-directed mutants, respectively. In addition, I acknowledge Spencer Anderson and Ruslan Sanishvili for assistance in X-ray data collection, Ted Huston for performing the ICP-HRMS analysis, and Ari Gafni and Edgar Lee for use of their CD spectropolarimeter. I kindly thank Ted Baker and Nayden Koon for furnishing us with the coordinates of the α-IPMS/AcCoA/2-OIV model.

REFERENCES

1. Davis, B. D. (1952) Biosynthetic interrelations of lysine, diaminopimelic acid, and threonine in mutants of Escherichia coli, *Nature 169*, 534-536.

2. Dewey, D. L., and Work, E. (1952) Diaminopimelic acid decarboxylase, *Nature 169*, 533-534.

3. Vogel, H. J. (1960) Two modes of lysine synthesis among lower fungi: evolutionary significance., *Biochim. Biophys. Acta 41*, 172-174.

4. Tucci, A. F., and Ceci, L. N. (1972) Homocitrate synthase from yeast, *Arch. Biochem. Biophys. 153*, 742-750.

5. Bhattacharjee, J. K. (1985) alpha-Aminoadipate pathway for the biosynthesis of lysine in lower eukaryotes, *Crit. Rev. Microbiol. 12*, 131-151.

6. Garrad, R. C., and Bhattacharjee, J. K. (1992) Lysine biosynthesis in selected pathogenic fungi: characterization of lysine auxotrophs and the cloned LYS1 gene of Candida albicans, *J. Bacteriol. 174*, 7379-7384.

7. Kosuge, T., and Hoshino, T. (1998) Lysine is synthesized through the alpha-aminoadipate pathway in Thermus thermophilus, *FEMS Microbiol. Lett. 169*, 361-367.

8. Xu, H., Andi, B., Qian, J., West, A. H., and Cook, P. F. (2006) The alpha-aminoadipate pathway for lysine biosynthesis in fungi, *Cell Biochem. Biophys. 46*, 43-64.

9. Andi, B., West, A. H., and Cook, P. F. (2004) Kinetic mechanism of histidine-tagged homocitrate synthase from Saccharomyces cerevisiae, *Biochemistry 43*, 11790-11795.

10. Qian, J., West, A. H., and Cook, P. F. (2006) Acid-base chemical mechanism of homocitrate synthase from Saccharomyces cerevisiae, *Biochemistry 45*, 12136-12143.

11. Karpusas, M., Branchaud, B., and Remington, S. J. (1990) Proposed mechanism for the condensation reaction of citrate synthase: 1.9-A structure of the ternary complex with oxaloacetate and carboxymethyl coenzyme A, *Biochemistry 29*, 2213-2219.

12. Anstrom, D. M., Kallio, K., and Remington, S. J. (2003) Structure of the Escherichia coli malate synthase G:pyruvate:acetyl-coenzyme A abortive ternary complex at 1.95 A resolution, *Protein Sci. 12*, 1822-1832.

13. Howard, B. R., Endrizzi, J. A., and Remington, S. J. (2000) Crystal structure of Escherichia coli malate synthase G complexed with magnesium and glyoxylate at 2.0 A resolution: mechanistic implications, *Biochemistry 39*, 3156-3168.

14. Koon, N., Squire, C. J., and Baker, E. N. (2004) Crystal structure of LeuA from Mycobacterium tuberculosis, a key enzyme in leucine biosynthesis, *Proc. Natl. Acad. Sci. U.S.A. 101*, 8295-8300.

15. Qian, J., Khandogin, J., West, A. H., and Cook, P. F. (2008) Evidence for a catalytic dyad in the active site of homocitrate synthase from Saccharomyces cerevisiae, *Biochemistry 47*, 6851-6858.

16. Kapust, R. B., Tozser, J., Fox, J. D., Anderson, D. E., Cherry, S., Copeland, T. D., and Waugh, D. S. (2001) Tobacco etch virus protease: mechanism of autolysis and rational design of stable mutants with wild-type catalytic proficiency, *Protein Eng. 14*, 993-1000.

17. Sheffield, P., Garrard, S., and Derewenda, Z. (1999) Overcoming expression and purification problems of RhoGDI using a family of "parallel" expression vectors, *Protein Expression Purif. 15*, 34-39.

18. Doublie, S. (1997) Preparation of selenomethionyl proteins for phase determination, *Methods Enzymol. 276*, 523-530.

19. Doublie, S. (2007) Production of selenomethionyl proteins in prokaryotic and eukaryotic expression systems, *Methods Mol. Biol. 363*, 91-108.

20. Brodersen, D. E., de La Fortelle, E., Vonrhein, C., Bricogne, G., Nyborg, J., and Kjeldgaard, M. (2000) Applications of single-wavelength anomalous dispersion at high and atomic resolution, *Acta Crystallogr. D. Biol. Crystallogr. 56*, 431-441.

21. Otwinowski, Z., and Minor, W. (1997) Processing of X-ray Diffraction Data Collected in Oscillation Mode, *Methods Enzymol. 276*, 307-326.

22. Terwilliger, T. C., and Berendzen, J. (1999) Automated MAD and MIR structure solution, *Acta Crystallogr., Sect D: Biol. Crystallogr. 55*, 849-861.

23. Vonrhein, C., Blanc, E., Roversi, P., and Bricogne, G. (2007) Automated structure solution with autoSHARP, *Methods Mol. Biol. 364*, 215-230.

24. Brunger, A. T. (2007) Version 1.2 of the Crystallography and NMR system, *Nat. Protoc. 2*, 2728-2733.

25. Brunger, A. T., Adams, P. D., Clore, G. M., DeLano, W. L., Gros, P., Grosse-Kunstleve, R. W., Jiang, J. S., Kuszewski, J., Nilges, M., Pannu, N. S., Read, R. J., Rice, L. M., Simonson, T., and Warren, G. L. (1998) Crystallography & NMR system: A new software suite for macromolecular structure determination, *Acta Crystallogr., Sect D: Biol. Crystallogr. 54*, 905-921.

26. Emsley, P., and Cowtan, K. (2004) Coot: model-building tools for molecular graphics, *Acta Crystallogr., Sect D: Biol. Crystallogr. 60*, 2126-2132.

27. Vagin, A. A., Teplyakov, A. (1997) MOLREP: an automated program for molecular replacement., *J. Appl. Crystallogr. 30*, 1022-1025.

28. Murshudov, G. N., Vagin, A. A., and Dodson, E. J. (1997) Refinement of macromolecular structures by the maximum-likelihood method, *Acta Crystallogr., Sect D: Biol. Crystallogr. 53*, 240-255.

29. Winn, M. D., Murshudov, G. N., and Papiz, M. Z. (2003) Macromolecular TLS refinement in REFMAC at moderate resolutions, *Methods Enzymol. 374*, 300-321.

30. Davis, I. W., Leaver-Fay, A., Chen, V. B., Block, J. N., Kapral, G. J., Wang, X., Murray, L. W., Arendall, W. B., 3rd, Snoeyink, J., Richardson, J. S., and Richardson, D. C. (2007) MolProbity: all-atom contacts and structure validation for proteins and nucleic acids, *Nucleic Acids Res. 35*, W375-383.

31. Trievel, R. C., Li, F. Y., and Marmorstein, R. (2000) Application of a fluorescent histone acetyltransferase assay to probe the substrate specificity of the human p300/CBP-associated factor, *Anal. Biochem. 287*, 319-328.

32. Collazo, E., Couture, J. F., Bulfer, S., and Trievel, R. C. (2005) A coupled fluorescent assay for histone methyltransferases, *Anal. Biochem. 342*, 86-92.

33. Amberg, D. C., Burke, D. J., and Strathern, J. N. (2005) *Methods in Yeast Genetics: A Cold Spring Harbor Laboratory Course Manual, 2005 Ed.*, Cold Spring Harbor Press, Cold Spring Harbor, NY.

34. Liu, Y., Gotte, G., Libonati, M., and Eisenberg, D. (2002) Structures of the two 3D domain-swapped RNase A trimers, *Protein Sci. 11*, 371-380.

35. Holm, L., Kaariainen, S., Rosenstrom, P., and Schenkel, A. (2008) Searching protein structure databases with DaliLite v.3, *Bioinformatics 24*, 2780-2781.

36. Fu, Z., Runquist, J. A., Forouhar, F., Hussain, M., Hunt, J. F., Miziorko, H. M., and Kim, J.-J. P. (2006) Crystal structure of human 3-hydroxy-3-methylglutaryl-CoA Lyase: insights into catalysis and the molecular basis for hydroxymethylglutaric aciduria, *J. Biol. Chem. 281*, 7526-7532.

37. Manjasetty, B. A., Powlowski, J., and Vrielink, A. (2003) Crystal structure of a bifunctional aldolase-dehydrogenase: sequestering a reactive and volatile intermediate, *Proc. Natl. Acad. Sci. U.S.A. 100*, 6992-6997.

38. Andi, B., West, A. H., and Cook, P. F. (2005) Regulatory mechanism of histidine-tagged homocitrate synthase from Saccharomyces cerevisiae. I. Kinetic studies, *J. Biol. Chem. 280*, 31624-31632.

39. Jaklitsch, W. M., and Kubicek, C. P. (1990) Homocitrate synthase from Penicillium chrysogenum. Localization, purification of the cytosolic isoenzyme, and sensitivity to lysine, *Biochem. J. 269*, 247-253.

40. Wulandari, A. P., Miyazaki, J., Kobashi, N., Nishiyama, M., Hoshino, T., and Yamane, H. (2002) Characterization of bacterial homocitrate synthase involved in lysine biosynthesis, *FEBS Lett. 522*, 35-40.

41. Guillen Schlippe, Y. V., and Hedstrom, L. (2005) A twisted base? The role of arginine in enzyme-catalyzed proton abstractions, *Arch. Biochem. Biophys. 433*, 266-278.

42. Mowat, C. G., Moysey, R., Miles, C. S., Leys, D., Doherty, M. K., Taylor, P., Walkinshaw, M. D., Reid, G. A., and Chapman, S. K. (2001) Kinetic and crystallographic analysis of the key active site acid/base arginine in a soluble fumarate reductase, *Biochemistry 40*, 12292-12298.

43. Remington, S., Wiegand, G., and Huber, R. (1982) Crystallographic refinement and atomic models of two different forms of citrate synthase at 2.7 and 1.7 A resolution, *J. Mol. Biol. 158*, 111-152.

44. Wiegand, G., and Remington, S. J. (1986) Citrate synthase: structure, control, and mechanism, *Annu. Rev. Biophys. Biophys. Chem. 15*, 97-117.

CHAPTER 3
STRUCTURAL BASIS FOR L-LYSINE FEEDBACK INHIBITON OF HOMOCITRATE SYNTHASE

The AAA pathway in *S. cerevisiae* is highly regulated at both the levels of gene expression and enzyme activity (1). Regulation of enzyme activity is mediated predominantly through feedback inhibition of HCS by L-lysine, thus limiting the metabolic flux through the pathway. This pathway is also regulated transcriptionally by two different mechanisms. Along with other amino biosynthesis pathways, enzymes in the second half of the AAA pathway respond to the general control of amino acid biosynthesis (2). Additionally, expression of several AAA pathway enzymes is specifically regulated by the transcriptional activator Lys14p in the presence of the pathway intermediate α-aminoadipate semialdehyde (3). Conversely, six of the seven *S. cerevisiae* AAA pathway enzymes, including HCS were shown to be repressed by the end product L-lysine (4). However, L-lysine regulation of the five enzymes downstream of HCS has been attributed to a diminished production of α-aminoadipate semialdehyde and inactivation of Lys14p due to a reduced metabolic flux caused specifically by lysine feedback inhibition of HCS (5, 6). This implicates feedback inhibition of HCS to be vital in the control of lysine biosynthesis at both the biochemical and transcriptional levels.

Lysine feedback inhibition of HCS has been observed in many fungal species that utilize the AAA pathway. Based on these studies two opposing models of inhibition have been proposed. Kinetic studies in ScHCS (7), PcHCS (8) and TtHCS (9) have demonstrated that L-lysine inhibition is competitive with the substrate 2-OG, suggesting that the amino acid binds within the enzyme's active site. However, this model leads to a contradiction in understanding how both 2-OG, a dicarboxylic acid, and lysine, a basic amino acid can both be accommodated within the same site. Feedback inhibition of HCS by L-lysine has also been proposed to be allosteric with L-lysine inhibition of *Y. lipolytica* HCS exhibiting allosteric kinetics (10). Further evidence for an allosteric model arises

from studies in which ScHCS point mutants were found to be insensitive to lysine yet still maintain HCS activity suggesting 2-OG and lysine may not bind in the same site (6). Due to data supporting both these models, the mechanism of feedback inhibition of HCS has remained unresolved.

To elucidate the molecular basis for feedback regulation of HCS, we have determined the structure of SpHCS in a binary complex L-lysine and compare it to he structures of the free enzyme and binary complex with the substrate 2-OG (Chapter 2). The structure of SpHCS/L-lysine complex reveals that the inhibitor binds within the 2-OG binding site at the center of the TIM barrel domain, in agreement with steady state kinetic analysis illustrating that the amino acid is a competitive inhibitor of 2-OG. Differential recognition of 2-OG and L-lysine is accomplished through a switch position within the active site in which acidic residues interact with the ε-ammonium group of L-lysine and basic residues coordinate the C5 carboxylate group of 2-OG. Steady state kinetic yeast growth assays of SpHCS mutants demonstrate that the acidic residues in the switch position are essential for L-lysine feedback inhibition in implicated *in vitro* and *in vivo*. Additionally, SpHCS mutations homologous to those reported for the L-lysine insensitive mutant in ScHCS also displayed a reduced sensitivity to L-lysine. Taken together these studies allow us to elucidate the mechanism of regulation of HCS by L-lysine feedback inhibition.

MATERIALS AND METHODS

Materials

DNA primers used for mutagenesis were synthesized by Integrated DNA Technologies. The sodium phosphate monobasic and potassium phosphate dibasic used in crystallization screens were purchased from Sigma at the highest quality available. Reagents used in the fluorescent HCS assay including the ThioStar dye (Luminos LLC), along with AcCoA and CoA purchased from Sigma were prepared as described in Chapter 2, whereas the L-lysine acetate, D-lysine and s-aminoethyl-L-cysteine (AEC) hydrochloride used in the inhibition studies were obtained at the highest grade from Sigma. All other materials used were of the highest grade available.

Mutagenesis and Purification of SpHCS Lysine Binding Mutants

Mutants of SpHCS/pHIS2 and SpHCS/pLp2211 involved in feedback inhibition by lysine were made by designing complementary sets of primers (Table 3.1) and using site-directed mutagenesis following a modified Quikchange™ mutagenesis kit protocol (Stratagene) as described in Chapter 2. Lysine binding mutants were overexpressed and purified identically to SpHCS purified for kinetic studies (Chapter 2) using a Zn(II) charged IMAC Sepharose™ High Performance resin (GE Healthcare) column for the affinity purification.

Crystallization of SpHCS in Complex with Lysine

SpHCS enzyme used in crystallization trails was purified on Talon (Clontech) Co(II) affinity resin column as described in Chapter 2. The sodium and potassium phosphate condition used to crystallize SpHCS in complex with 2-OG (Chapter 2) was optimized and used to produce crystals of SpHCS in complex with L-lysine using the hanging drop vapor diffusion technique as described in Chapter 2. SpHCS crystals in complex with lysine were obtained in 1.2-1.5 M sodium and potassium phosphate (pH 5.8-6.8) at 24 ^{o}C using 20 mg/mL EDTA treated SpHCS, 1 mM Zn(II) and 100 mM L-lysine. SpHCS/L-lysine crystals were harvested, cryo-protected in the crystallization condition containing 20% glycerol and flash frozen in liquid nitrogen.

Data Collection, Model Building and Refinement

A data set of SpHCS in complex with the feedback inhibitor L-lysine to 2.38 Å (Table 3.2) was collected at the 21-ID-G beamline of LS-CAT at a wavelength of 0.97856 Å and a detector distance of 300 mm. 150^{o} of data was collect at an oscillation of 0.5^{o} with an exposure time of 4 s per frame. The data set was processed and scaled in HKL2000 (11) and the structure was solved using the high resolution (2.24 Å) SeMet-SpHCS structure (PDB 3IVS) as a model for molecular replacement in MOLREP (12). Model building and refinement was performed similarly to the SpHCS 2-OG complexes (Chapter 2) using the programs Coot (13) and REFMAC (14). The final SpHCS/lysine structure had R_{work} and R_{free} values of 16.9% and 20.3%, respectively (Table 3.2). Additionally, no residues were found in the disallowed regions of the Ramachandran

Table 3.1 Primers used for SpHCS mutagenesis of residues involved in L-lysine feedback inhibition

Mutation	Primer
D123N	5′- GAGACTGGAGTTGATGGTGTT**AAT**GTTGTTATCGGAACTTCTC-3′[a]
E222Q	5′-TCTCTTGTGATATT**CAA**TGTCATTTTCACAATGACACTGGTATGGCTATTG-3′
R288K	5′-CCCACAAATACAAGCTTAACCAGTTA**AAG**GAGCTTGAAAACCTTGTCGC-3′
Q364R	5′-GCCATCAAATCTCGTGCTGAG**CGG**CTTAACCTTCATCTTACTGATGCC-3′

[a]Forward primer is listed with reverse primer being the reverse complement of the forward primer. The mutated codon is denoted in bold.

Table 3.2 Data collection and refinement statistics.

	WT SpHCS/L-lysine complex (Zn(II))
Data Collection	
Beamline	21-ID-G
Space group	$P6_2$
Cell dimensions a=b,c (Å)	135.6, 122.9
Wavelength (Å)	0.97856
Resolution (Å)	40.0-2.38 (2.48-2.38)[a]
R_{merge} (%)	5.7 (47.2)
I/σI	35.7 (3.02)
Reflections	
Total	455,828
Unique	50,397
Redundancy	9.0 (6.7)
Completeness (%)	98.0 (89.1)
Refinement	
Resolution range (Å)	38.7-2.38
No. of reflections	47,811
No. of atoms	6107
Protein atoms	5799
Metals/ligand atoms	4/20
Water atoms	284
R_{work}/R_{free}[b]	17.0/20.4
Average B-factors (Å^2)	
Overall	53.6
Protein	54.6
Metals/Ligand	35.9/50.0
Water	55.3
Root mean square deviation	
Bond length (Å)	0.013
Bond angles (^{o})	1.402
MolProbity score	2.11[c]
Ramachandran favored (%)	96.03
Ramachandran allowed (%)	3.97
Ramachandran outliers (%)	0.00

[a]Values in parentheses are for the highest-resolution shell.
[b]$R_{work} = \sum ||F_o| - |F_c|| / \sum |F_o|$; $R_{free} = \sum T ||F_o| - |F_c|| / \sum T |F_o|$, where T is a randomly chosen set of reflections consisting of 5% of the total.
[c]89th percentile for 2.13 Å -2.63 Å structures

plot as determined by MolProbity (15). Simulated annealing omits maps were calculated in CNS (16, 17).

Steady State Kinetics and Lysine Inhibition Studies

The fluorescence HCS assay was used to determine the steady state kinetic parameters for WT and mutant SpHCS enzymes as described in Chapter 2. Briefly, HCS assays were carried out in triplicate at room temperature in 100mM HEPES, pH 7.5 using 10 nM enzyme and variable concentrations of 2-OG and AcCoA. To correct for the increased fluorescence of the ThioStar dye (Luminos) with increasing concentrations of 2-OG over 2 mM, CoA (ε_{260nm} = 15,400 M^{-1} cm^{-1}) standard curves were performed at every 2-OG concentration over 2 mM that was used in each assay. The K_M and k_{cat} values for HCS mutants were determined by fitting the data to the Michaelis-Menten non-linear regression using Prism (GraphPad Software).

The fluorescence HCS assay was also used to determine the inhibition pattern and equilibrium inhibition constant (K_i) value of L-lysine versus the substrates 2-OG and AcCoA for WT SpHCS. Additionally, the K_i values for L-lysine versus 2-OG were determined for HCS mutants implicated in lysine binding. Initial velocities were measured in triplicate at varying concentrations of the substrate 2-OG (0.66-2.0 mM or 0-100 mM for the E222Q mutant) at various fixed concentrations of L-lysine (0-50 μM for WT enzyme or 0-10mM for the lysine binding mutants) with AcCoA held constant (100 μM or 200 μM for the E222Q) mutant. Inhibition of WT SpHCS by D-lysine (up to 2 mM) was also tested using a similar protocol. To determine the inhibition pattern and K_i value of L-lysine versus the substrate AcCoA for WT SpHCS, initial velocities were measured in triplicate at varying concentrations of the substrate AcCoA (0-100 μM) at various fixed concentrations of L-lysine (0-100 μM) with the 2-OG concentration held at a saturating concentration of 2 mM. To correct for the increased fluorescence due to lysine concentrations over 1mM, CoA standard curves were performed at every combination of L-lysine and 2-OG concentrations used in each assays.

Data was analyzed using the program Prism (GraphPad Software). Double reciprocal plots of the 2-OG concentrations versus initial velocities for each lysine concentration and Lineweaver-Burk lines using K_M and V_{max} values calculated from

Michaelis-Menten fits to the untransformed data were plotted to determine the pattern of inhibition. To determine K_i values for L-lysine versus the substrate 2-OG, data sets were fit to the non-linear Michaelis-Menten regressions for a competitive inhibitor (Eq. 1). Data for lysine inhibition versus the substrate AcCoA was fit to the regression for a mixed inhibitor (Eq. 2), where K_i and K_i' represent the equilibrium constants for competitive and uncompetitive inhibition, respectively.

$$\text{Eq 1: } \nu_o = k_{cat}[E_t][S]/([S] + K_M(1+[I]/K_i))$$

$$\text{Eq.2: } \nu_o = k_{cat}[E_t][S]/(K_M(1+ [I]/K_i) + [S](1+[I]/K_i'))$$

In Vivo Cell Growth Assays

In vivo viability of the *lys4*$^+$ lysine mutants in the absence of L-lysine was determined as previously described (Chapter 2). Cells were assayed for growth on synthetic complete medium lacking lysine (lys-) and uracil (ura-) to maintain selection of the vector, WT, or mutant *lys4*$^+$ plasmids. Where indicated, plates contained AEC. Protein immunoblot analysis showed that the steady state levels of the mutant proteins were comparable to WT SpHCS (data not shown).

RESULTS

Crystal Structure of SpHCS Bound to L-lysine

The crystal structure of full length SpHCS (residues 1-418) bound to the feedback inhibitor lysine was determined by molecular replacement to 2.38 Å using SeMet-SPHCS (PDB 3IVS) (Chapter 2) as a model (Table 3.1). Unlike the free SpHCS structure, the L-lysine bound structure contains the divalent metal Zn(II) in the active site, which was achieved by removing the Co(II) from the Talon purified enzyme with EDTA and adding 2mM Zn(II) during crystallization. The overall structure of the SpHCS/lysine complex is highly similar to the Co(II)-bound free SpHCS structure with a R.M.S.D. of 0.66 Å for all aligned atoms. (Figure 3.1A), whereas an alignment with the Zn(II)-bound SpHCS/2-OG complex reveals that the L-lysine bound structure lacks the β4.1- β4.2 hairpin motif and domain-swapped N-terminal extension present in the substrate complexes (Figure 3.1B). In addition, the domain-swapped lid motif (residues 323-329), which regulates substrate

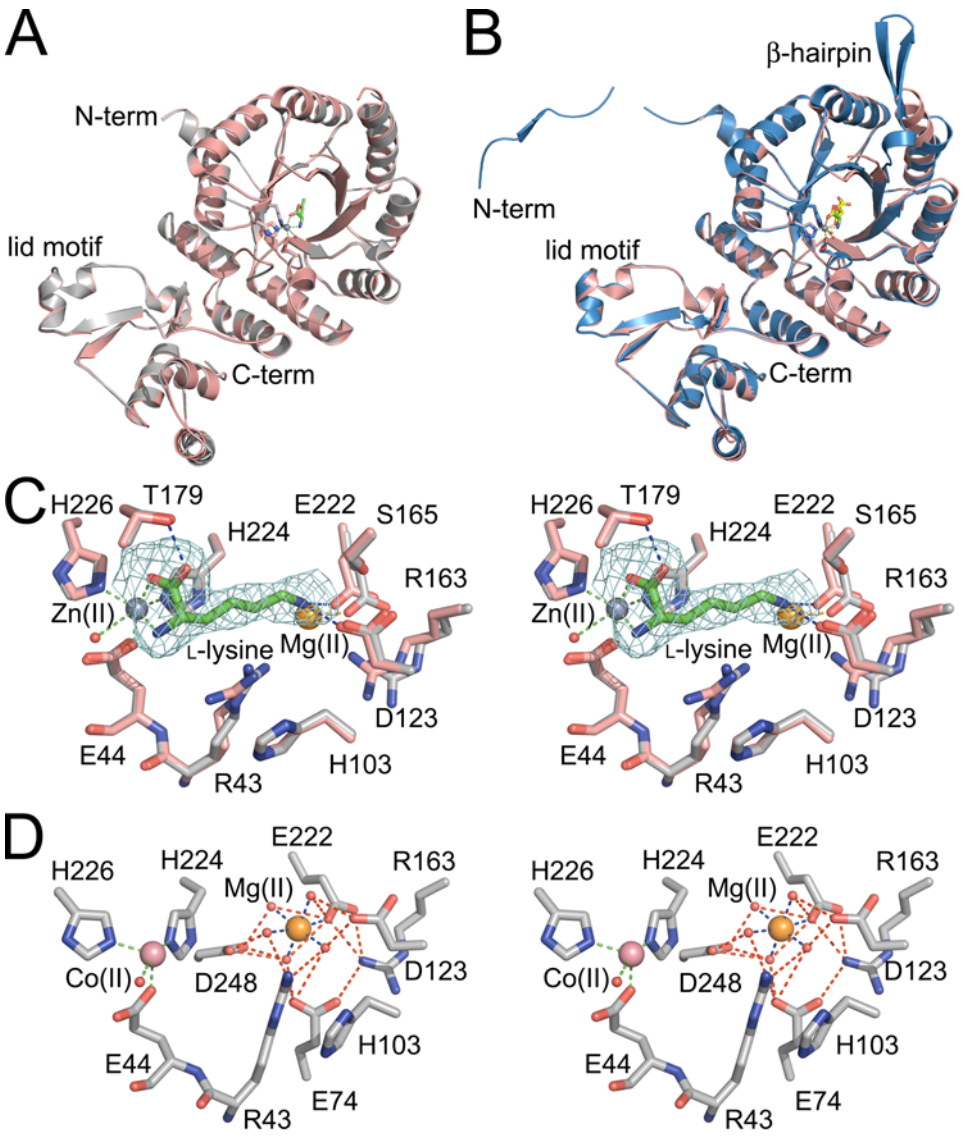

Figure 3.1 Structure of SpHCS in complex with L-lysine and comparison with the free enzyme. (A) Ribbon diagram of the overall structure of SpHCS in complex with L-lysine (pink with L-lysine rendered in green) overlaid with free enzyme (gray). **(B)** Overall structure of SpHCS L-lysine complex (colored as described in A) superimposed with SpHCS 2-OG closed lid complex (blue with 2-OG rendered in yellow). **(C)** Stereoview of the active site of SpHCS L-lysine complex (pink carbons) overlaid with SpHCS free enzyme (gray carbons). Electron density of the simulated annealing F_o-F_c omit map (contoured at 2.5 Å) corresponding to the L-lysine is shown in cyan, while green and blue dashes represent coordination to the Zn(II) ion and hydrogen bonding to L-lysine, respectively **(D)** Stereoview of the active site of the free SpHCS enzyme (gray carbons). Coordination to the active site Co(II) ion (pink) is represented by green dashes, while coordination to the Mg(II) ion (orange) and hydrogen bonds with the protein and solvent molecules are shown as blue and red dashes, respectively.

substrate binding in the neighboring monomer, adopts a closed conformation as in the free enzyme and closed SpHCS/2-OG structures (Chapter 2).

Inspection of the electron density maps of the active site of SpHCS revealed density corresponding to a bound L-lysine molecule, which was subsequently confirmed in a simulated annealing F_o-F_c omit map (Figure 3.1C). An alignment of the coordinates of the SpHCS free enzyme and L-lysine complex reveals that the residues within the active site are virtually superimposable with the exception of Arg43 that adopts an alternative side chain conformation to accommodate inhibitor binding (see below). In the free enzyme structure, a Mg(II) ion occupies the area of the ε-ammonium group of L-lysine and is bound to Glu222 and five water molecules in an octahedral coordination, suggesting that this pocket can function as a general cation binding site (Figure 3.1D).

An alignment of the L-lysine and 2-OG complexes illustrates that the substrate and inhibitor are nearly superimposable, providing structural evidence that L-lysine is a competitive inhibitor of 2-OG (Figure 3.2A). Surprisingly, the substrate and inhibitor have similar binding conformations despite their lack of structural and chemical homology. Coordination of the carboxylate groups and α-amine of L-lysine to the active site metal coincides with the coordination of the C1 carboxylate and 2-oxo moiety of 2-OG, respectively In addition, the carboxylate of L-lysine hydrogen bonds to the hydroxyl group of Thr197, analogous to its interactions with the C1 carboxylate of 2-OG. The L-lysine side chain adopts an extended all-*trans* conformation that spans the diameter of the TIM barrel's interior, positioning its ε-ammonium group for the salt-bridge interactions with the carboxylate groups of Asp123 and Glu222 and water mediated interactions with Glu74 and Asp258 (Figure 3.2B). The Asp123 and Glu222 residues are located in the barrel's interior adjacent to Arg163 and Ser165 that hydrogen bond to the C5 carboxylate of 2-OG and assist in orienting the side chain of Arg163 for hydrogen bonding to the substrate (Figure 3.2C).

A superimposition of the structures of the lysine and 2-OG closed complexes provides insights into the flexibility of the active site in accommodating the binding of the inhibitor and substrate (Figure 3.2A). This flexibility arises through conformational changes in the key active site residues that are coupled with ligand recognition.

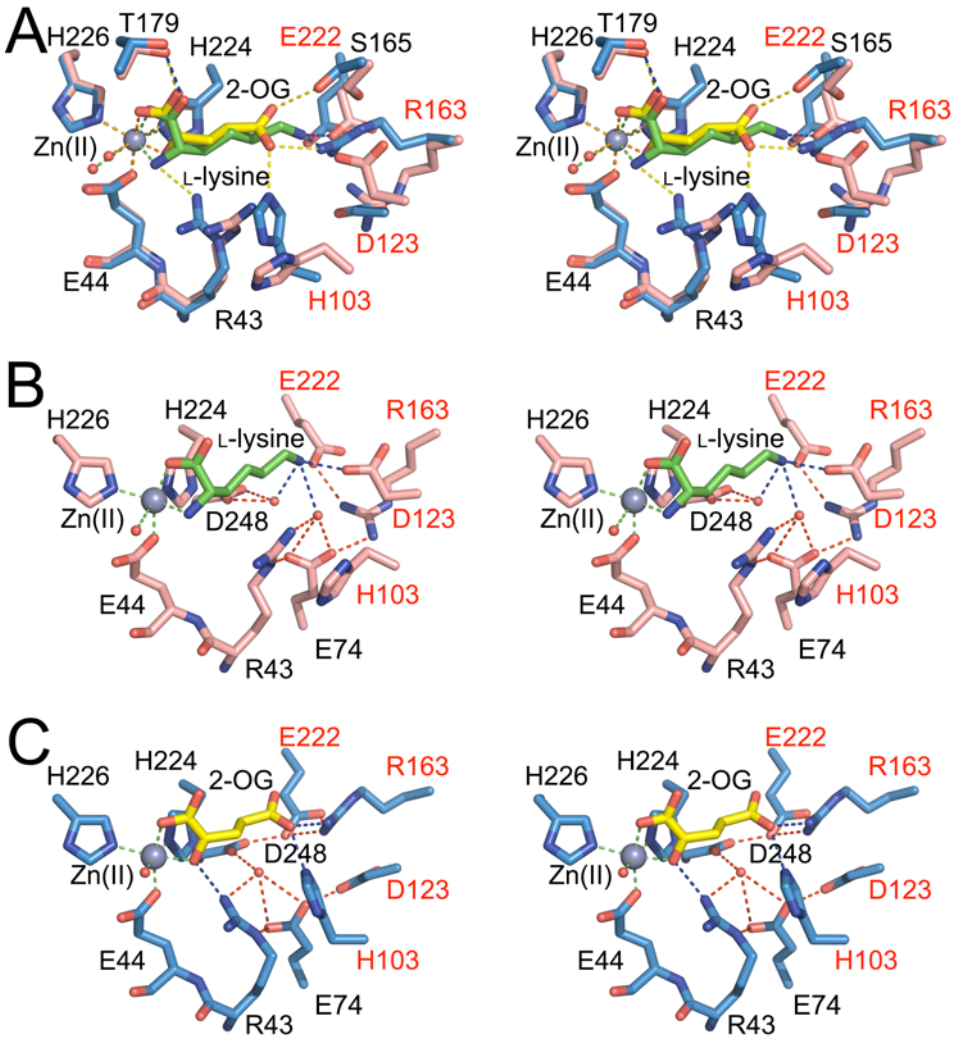

Figure 3.2 The switch position in SpHCS mediates differential ligand recognition. (A) Stereoview of the active site of the SpHCS L-lysine complex (pink carbons) superimposed with the SpHCS 2-OG closed lid complex (blue carbons). Orange and yellow dashes represent coordination to the Zn(II) ion and hydrogen bonding to 2-OG respectively in the 2-OG closed loop complex, whereas coordination to the Zn(II) ion and hydrogen bonding to L-lysine are depicted as described in Figure 1C. Residues composing the switch position are labeled in red. (B) Stereoview of the active site of the SpHCS/L-lysine complex (pink carbons with L-lysine shown with green carbons). Coordination to the Zn(II) ion (gray) is shown as green dashes while potential hydrogen bonds to the inhibitor lysine and are represented by blue dashes. Hydrogen bonds within the protein and to solvent molecules are displayed as red dashes. (C) Stereoview of the active site of the SpHCS/2-OG complex (blue carbons with 2-OG shown with yellow carbons). Coordination to the Zn(II) ion (gray), hydrogen bonds to 2-OG, and interactions between the protein and solvent are as depicted as in panel B. For clarity, only certain residues that hydrogen bond to 2-OG are shown.

The residues, His103, Asp123, Arg163 and Glu222 have roles in distinguishing between 2-OG and lysine. These four residues line the interior wall of the TIM barrel opposite the metal ion active site in a location that we refer to as the switch position. In the SpHCS/2-OG complex, the basic residues His103 and Arg163 rotate towards the substrate to form hydrogen bonds or salt bridge interactions with the C5 carboxylate of 2-OG (Figure 3.2B). Previous studies have shown that these residues are important *in vitro* and *in vivo* for homocitrate production (Chapter 2). In the L-lysine SpHCS complex, these basic residues are orientated away from the inhibitor and the acid residues Asp123 and Glu222 reorient to form salt bridge interactions with the lysine ε-ammonium group (Figure 3.2B). Alignment of the SpHCS free enzyme and the ligand bound complexes of SpHCS reveals that the conformational changes in the residues that make up the switch position appear to be coordinated due to their close proximity and to the salt bridge interactions between Arg163 and Glu222 that is maintained in each of the structures (Figure 3.2). The arrangement of the switch position in the 2-OG complex may also explain the ordering of the adjacent β-hairpin motif that is disordered in the structures of the free enzyme and L-lysine complex (Figure 3.1A and 3.1B). Analysis of the crystal packing in the three structures reveals that the β-hairpin motif is solvent exposed in the various structures and crystal contacts do not contribute to the ordering of this region. Thus, rearrangements in the switch region residues appear to coincide with the ordering of this region in the 2-OG bound structure.

Along with conformational changes within the active site, rearrangements in the lid motif are also observed in the SpHCS free enzyme and ligand-bound complexes. In the free enzyme, Arg43 forms a bifurcated hydrogen bond between its guanidinium group and the carbonyl oxygen of Ala324′ (the ′ denotes a residue from the adjacent monomer) (Figure 3.3A), which maintains the closed lid state. However, the binding of the inhibitor L-lysine causes a conformational change in the side chain of Arg43 resulting in a direct and a water-mediated hydrogen bond to the carbonyl oxygen of Ala324′. This conformational change and altered hydrogen bonding pattern results in the lid motif shifting a small distance away from the TIM barrel active site as compared to the free enzyme. A third lid motif conformation is seen in the 2-OG complex with the guanidinium groups of Arg43 forming hydrogen bonds to the 2-oxo group of the

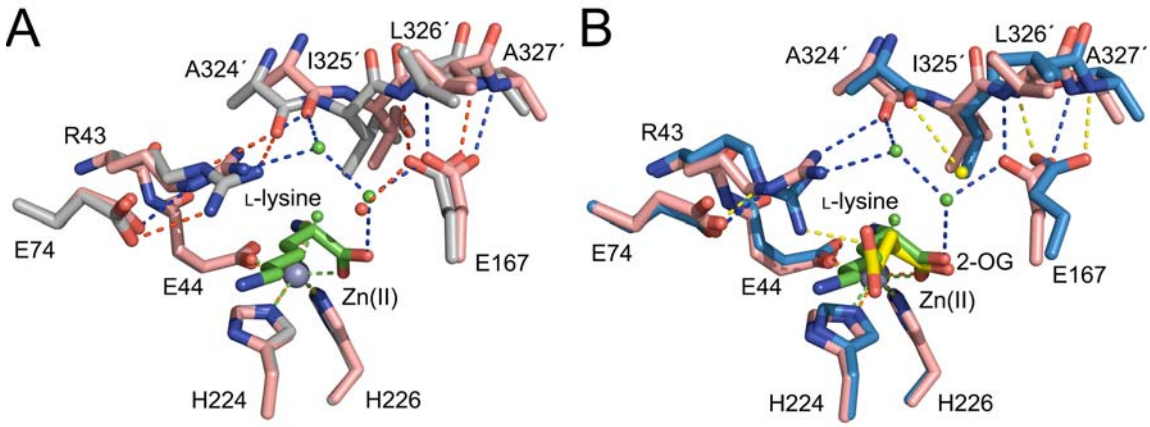

Figure 3.3 Conformational variations in the lid motif among SpHCS structures. (A) Superimposition of the active site and lid motif in the SpHCS/L-lysine complex (pink with L-lysine shown in green carbons and water molecules represented as green spheres) and SpHCS free enzyme (gray with water molecules shown as red spheres). Coordination to the Zn(II) ion (gray) in the SpHCS/L-lysine complex and in free SpHCS is depicted as green and orange dashes, respectively. Hydrogen bonds within the SpHCS/L-lysine complex are shown as blue dashes, whereas they are illustrated as red dashes in the structure of the free enzyme. **(B)** Overlay of the lid motif and active site of the SpHCS/L-lysine complex (colored as described in A) and the SpHCS/2-OG complex (blue with 2-OG shown in yellow carbons and water molecules represented as yellow spheres). Coordination to the Zn(II) ion and hydrogen bonds in the SpHCS/L-lysine complex are colored as depicted in panel A, while in the SpHCS/2-OG complex, these interactions are represented by orange and yellow dashes, respectively.

substrate (Figure 3.3B). This arrangement breaks the hydrogen bonding between Arg43 and Ala324′ allowing the lid motif to shift further away from the active site. These observations imply that the conformation adopted by the lid motif is sensitive to the ligand bound within the active site of the enzyme.

Kinetic Analysis of L-lysine Inhibition of HCS

The structure of the SpHCS/L-lysine complex provides structural evidence that L-lysine binds within the active site and is a competitive inhibitor with 2-OG. To confirm this finding, we analyzing the double reciprocal plots of velocity versus substrate concentration for both 2-OG and AcCoA. The inhibition patterns indicated that L-lysine was a competitive inhibitor with 2-OG and a mixed inhibitor with AcCoA (Figure 3.4). These inhibition pattern are in corroboration with the Bi-Bi sequential mechanism of HCS in which 2-OG binds before AcCoA (18) and are also in agreement with our structural studies which indicate that L-lysine and 2-OG bind within the same site (Figure 3.2A). L-lysine competitively inhibited the binding of 2-OG with a K_i value of 3.56 ± 0.66 μM (Figure 3.4. and Table 3.3). This value is in agreement with K_i values for HCS regulation by lysine in *T. thermophilus* (K_i = 9.4 μM) (9) and *P. chrysogenum* (K_i = 8 μM) (8). We also investigated the inhibition equilibrium constants for L-lysine inhibition a with respect to AcCoA and measured K_i and K_i' values of 63.2 ± 9.1 μM and 191 ± 60 μM, respectively. Finally, we probed the stereospecificity of lysine inhibition of HCS by both D- and L-lysine. Unlike L-lysine, D-lysine did not inhibit SpHCS activity at concentration up to 2 mM (data not shown) demonstrating that HCS specifically recognizes L-lysine. Taken together, the kinetic inhibition pattern of L-lysine versus both substrates along with the structure of SpHCS with L-lysine bound in the same active site pocket as the substrate 2-OG provides strong evidence that L-lysine regulates the activity of SpHCS through active-site inhibition.

***In Vitro* and *In Vivo* Analysis of L-lysine Interacting Residues**

After examining the biochemical basis for inhibition, we sought to investigate the functions of the L-lysine-interacting residues in SpHCS. To understand the biochemical basis for the conformation changes that take place upon L-lysine binding to SpHCS, we

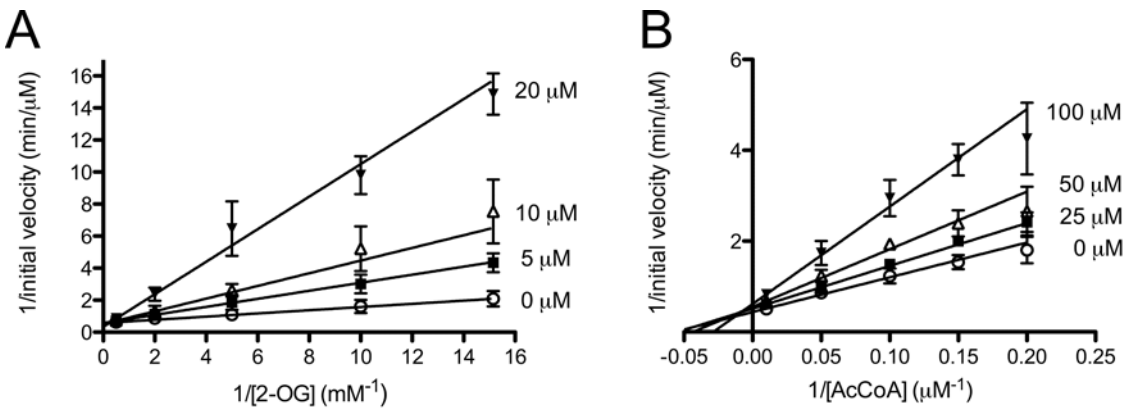

Figure 3.4 Kinetic mechanism of L-lysine inhibition of SpHCS. (A) Double reciprocal plots of initial velocity versus 2-OG concentration at different concentrations of L-lysine and a fixed saturating concentration (100 mM) of AcCoA. **(B)** Double reciprocal plots of initial velocity versus AcCoA concentration at different concentrations of L-lysine and a fixed saturating concentration (2 mM) of 2-OG. Data points are the average of triplicate measurements, and the error bars represent one standard deviation, with the lines representing Lineweaver-Burk fits using the V_{max} and K_M values derived from Michaelis-Menten fits to the untransformed data.

Table 3.3 Kinetic analysis and lysine inhibition studies of WT SpHCS and mutants implicated in lysine inhibition

Mutant	K_M AcCoA (μM)	k_{cat} AcCoA (min^{-1})	k_{cat}/K_M (min^{-1} μM^{-1})	K_M 2-OG (mM)	k_{cat} 2-OG (min^{-1})	k_{cat}/K_M (min^{-1} mM^{-1})	K_i L-lysine (μM)
WT	10.7 ± 0.6[b]	299 ± 7	28.0 ± 1.7	0.159 ± 0.015	308 ± 4	1940 ± 190	3.56 ± 0.66
D123N	13.2 ± 1.7	217 ± 7	16.4 ± 2.1	0.284 ± 0.033	217 ± 7	771 ± 94	>100,000
E222Q	47.7 ± 5.6	215 ± 9	4.51 ± 0.56	9.66 ± 1.46	191 ± 7	19.7 ± 3.2	44,400 ± 9700
R288K	14.0 ± 1.6	194 ± 7	13.9 ± 1.7	0.247 ± 0.032	200 ± 6	809.7 ± 102	558 ± 57
Q364R	15.3 ± 1.2	170 ± 4	11.1 ± 0.9	0.296 ± 0.028	165 ± 4	557.4 ± 58	921± 120

[a]Steady state kinetic parameters for WT SpHCS are previously reported (Chapter 2).
[b]Errors are reported as the error in curve fitting.

first determined the steady state kinetic parameters for conservative mutations of the switch region residues Asp123 and Glu222, which form salt bridges to the ε-ammonium group of L-lysine. Mutagenesis of Asp123 to asparagine (D123N) results in almost WT activity (k_{cat} = 70% WT) with less than a 2-fold affect on the K_M values for both AcCoA and 2-OG (Table 3.3). The E222Q substitution also had a turnover number comparable to the WT enzyme, but exhibited an increased K_M values for 2-OG (60 fold), presumably due to the disruption in a salt bridge interaction between its carboxylate group and the guanidinium group of Arg163, an important residue involved in 2-OG binding (Chapter 2).

We next determined the effect these SpHCS mutations had on L-lysine binding. Double reciprocal plots of initial velocity versus the substrate 2-OG revealed that L-lysine inhibition of the E222Q mutant was severely compromised (K_i = 44.4 mM), whereas the D123N mutation completely abolished lysine inhibition up to a concentration of 100 mM (Table 3.3). With intracellular concentrations of lysine in *S. cerevisiae* ranging from 1-10 mM (19, 20), the high K_i values measured for these mutants suggests that the salt bridge interactions of the ε-amine of lysine to both Asp123 and Glu222 are essential for feedback inhibition of SpHCS by L-lysine and may render mutations of these residues insensitive to feedback regulation *in vivo*.

To evaluate this possibility, we examined the growth of these mutants in a *S. cerevisiae lys20Δ lys21Δ* double deletion strain that was previously generated (Chapter 2). The *lys20Δ lys21Δ* deletion strain exhibits lysine auxotrophy; yet thrives when lysine is present in the media. We transformed the double deletion strain with a plasmid consisting of the LYS20 promoter followed by the mutant *lys4*$^+$ genes to see if they could support growth in lysine-deficient media. The D123N and E222Q mutants were both able to complement the lysine auxotrophy of the double deletion strain (Fig. 3.5). However, the E222Q displayed a weaker growth phenotype, most likely due to its increased K_M value for 2-OG (Table 3.3) that decreased its catalytic efficiency (defined as k_{cat}/K_M). We next tested the response of the D123N and E222Q mutations to lysine inhibition in vivo using AEC, a toxic analog that was previously used to identify ScHCS mutants that are defective in feedback regulation (6). The toxicity of ACE may be due to incorporation

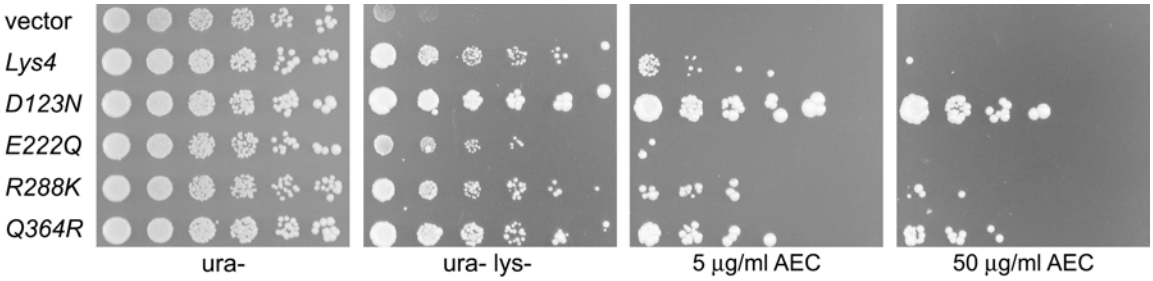

Figure 3.5 Effects of mutations of lysine binding residues *in vivo*. HCS null strain was transformed with empty vector, wild-type *lys4*$^{+}$, and *lys4* mutants engineered at positions D123N, E222Q, R288K and Q364N (pLP 2387-pLP2390, respectively). Growth was compared on medium containing lysine (ura-, to select for the plasmids), on medium lacking lysine to evaluate HCS function (ura- lys-) and on medium (ura- lys-) containing AEC, a toxic lysine analog, at the indicated concentrations. Cell cultures were grown under permissive conditions (ura-), normalized to an A_{600} of 1, and serially diluted five-fold. Plates were incubated at 30˚C for 4 days (ura-, lys-) or 10 days (AEC).

into protein, as an AEC-resistant mutant results in altered lysyl-tRNA synthase activity (21). As expected, the *lys20Δ lys21Δ* strain transformed with WT SpHCS exhibited weak growth at 5 μg/mL AEC that was completely abolished at 50 μg/mL AEC (Figure 3.5). Similar to the WT enzyme, the E222Q mutation could not overcome AEC toxicity at either concentration primarily due to its defect in catalytic efficiency due to its high K_M value for 2-OG (Table 3.3) and reduced growth phenotype on ura- lys- media (Figure 3.5). Conversely, the D123N mutation displayed strong resistance to AEC at concentrations up to 50 μg/mL (Figure 3.5), in agreement with the complete insensitivity of this mutation to L-lysine inhibition *in vitro* (Table 3.3). These findings also suggest that the D123N mutation overproduced lysine *in vivo*, enabling yeast to survive the toxicity of AEC. Together, our *in vitro* and *in vivo* data demonstrate that the salt bridge interactions between the L-lysine e-ammonium group and the Asp123 and Glu222 carboxylate groups in the switch position are critical to feedback regulation.

Location and Function of the Reported L-lysine Insensitive Mutants

In addition to investigating the roles of Asp123 and Glu222 in L-lysine inhibition, we probed the role of lysine-overproducing mutants previously identified in the ScHCS isozymes Lys20 and Lys21. Three point mutations including R276K and S385F in ScHCS Lys20 and Q366R in ScHCS Lys21 were identified to be insensitive to lysine by selecting for resistance to AEC, a toxic analog to lysine (6). A sequence alignment of the C-terminal domains of SpHCS and ScHCS illustrates that Arg276 in ScHCS Lys20 and Q366 in ScHCS Lys21 are conserved in the SpHCS (homologous to residues Arg288 and Gln364), whereas Ser385 of ScHCS Lys20 is not conserved in SpHCS and was not included in our studies (Figure 3.6).

Investigation of the SpHCS crystal structures reveals that these residues are located over 25 Å away from the TIM barrel active site domain where L-lysine binds. Arg288 resides in α10 in the enzyme's N-terminal domain and adopts different conformations in the free enzyme and ligand bound complexes. In the SpHCS/L-lysine complex, the arginine side chain extends towards the end of α13 of the same monomer forming hydrogen bonds to the backbone carbonyl groups of Leu399 and Tyr402 (Figure 3.7A). In the SPHCS/2-OG complex, the side chain of Arg288 is positioned similarly to

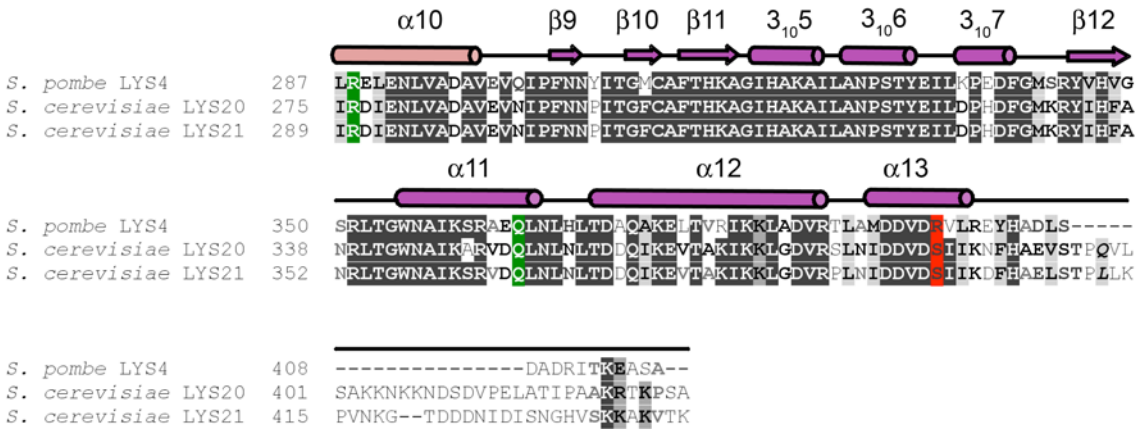

Figure 3.6 Sequence alignment of the C-terminal domain of SpHCS and ScHCS Lys20 and Lys21. The secondary structure of the TIM barrel (pink), and C-terminal subdomain I and II (violet) of the SpHCS/L-lysine complex is depicted above the alignment. Residues implicated in L-lysine binding (ref) that are conserved (green) and non-conserved (red) in SpHCS are highlighted.

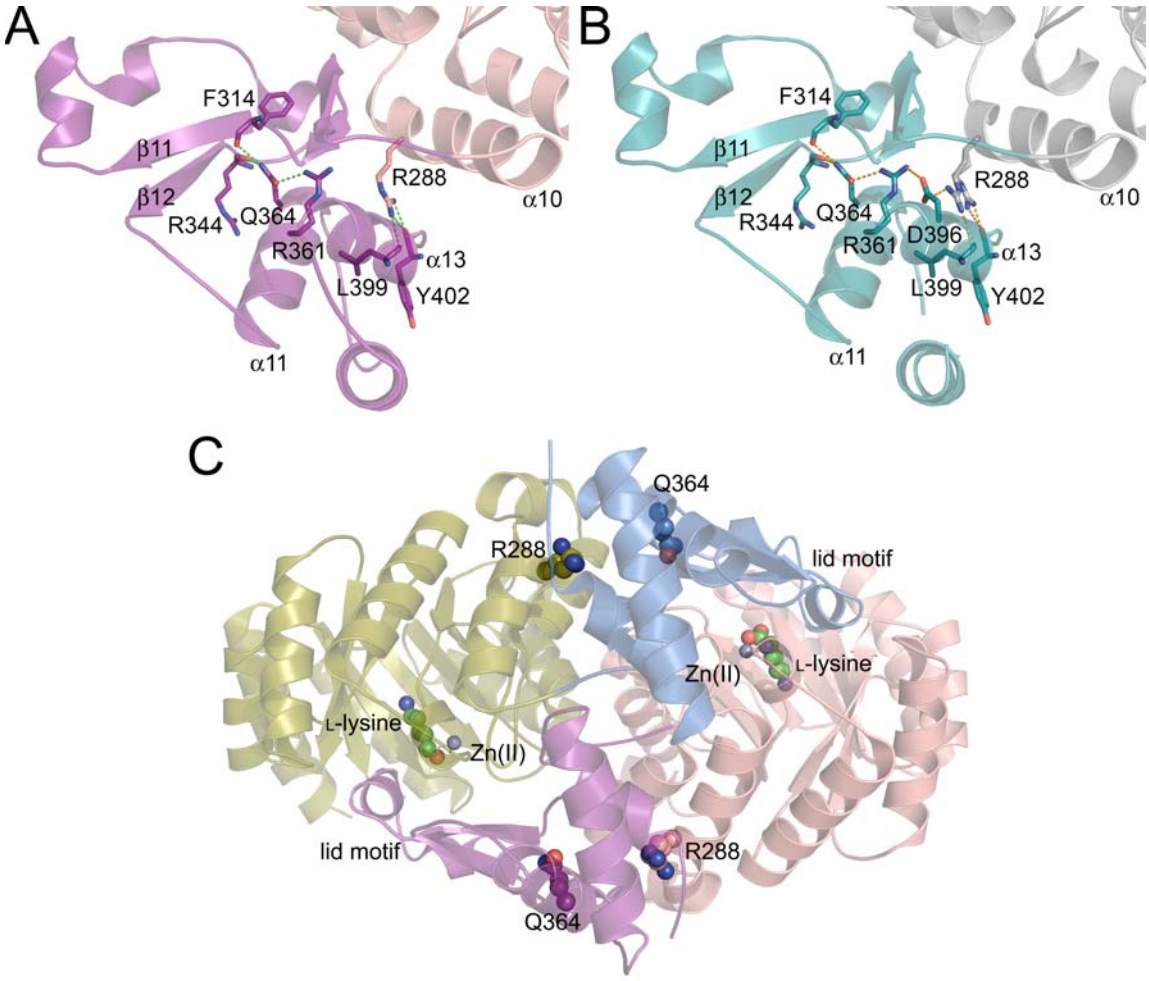

Figure 3.7 Structural locations of the L-lysine insensitive mutations. (A) Ribbon diagram of the N-terminal TIM barrel active site domain (pink) and C-terminal domain (violet) of an SpHCS monomer in complex with L-lysine. Arg288 and Gln364, along with their interacting partners are depicted as sticks with hydrogen bonds depicted as green dashes. **(B)** Ribbon diagram of the N-terminal TIM barrel active site domain (gray) and C-terminal domain (teal) of a monomer of the SpHCS free enzyme. Arg288 and Gln364, along with their interacting partners are depicted as sticks with hydrogen bonds depicted in orange **(C)** Ribbon diagram of an SpHCS/L-lysine dimer depicting the location of Arg288 and Gln364 (rendered as spheres). The N-and C-terminal domain of monomer A is as described in panel (A), whereas they are shown in yellow and blue, respectively in monomer B. L-lysine (green) and the active site Zn(II) (grey) metal ion are represented as spheres.

the L-lysine complex (data not shown). However in the free enzyme, Arg288 adopts two different conformations. One conformation is similar to the ligand bound enzyme, and the alternate conformation is orientated to form a hydrogen bond with the side chain of Asp396 in α13. In contrast, Glu364 is located in the same position in these three structures. It resides in α11 of the C-terminal subdomain II and forms hydrogen bonds with the backbone carbonyl groups of Phe314 and Arg344 in parallel β-strands β11 and β12 and with the guanidinium group of Arg361 (Figure 3.7B). Notably, the Arg288 and Gln364 in each monomer are located at opposite faces in the SpHCS homodimer (Figure 3.7C) and only form interactions within their own SpHCS monomer (Figure 3.7A and 3.7B), implying that these residues do not form a surface that may bind L-lysine, nor do they directly participate in interactions or conformational changes at the subunit interface of the dimer.

To assess the effects of the R288K and Q364R point mutation in feedback regulation, we assayed their activity *in vitro* and *in vivo* (Figure 3.4 and Table 3.3). The R288K and Q364R mutations exhibit near WT K_M values for both AcCoA and 2-OG with 65% and 55% the turnover rate when compared to WT, respectively (Table 3.3). In agreement with the effects of the corresponding ScHCS mutants (6), the SpHCS R288K and Q364R mutations impaired L-lysine inhibition by values of ~150 and ~300 fold, respectively compared to the K_i for competitive inhibition against 2-OG for the WT enzyme. Although these mutants exhibited a substantial decrease in the sensitivity to feedback regulation, their K_i values are >45-fold lower that those determined for the D123N and E222Q mutants. This difference may be due to the fact that the latter mutants form direct interactions with L-lysine (Figure 3.2B and Table 3.2), whereas the R288K and Q364R mutants appear to decrease lysine sensitivity by an indirect mechanism given their distances from the active site.

Additionally, we examined the effects of the SpHCS R288K and Q364R mutations *in vivo*. Both mutations complemented the lysine auxotrophy of the *S. cerevisiae* deletion strain (Figure 3.5). In agreement with previous studies by Feller *et al* (6), both the R288K and Q364R mutants displayed reduced sensitivity to AEC compared to WT SpHCS and the E222Q mutation (Figure 3.5). However, their resistance to AEC was not as strong as that of the D123N mutation, consistent with the

kinetic data demonstrating that this mutation abolished feedback inhibition (Table 3.3). In summary, the L-lysine insensitivity of the SpHCS R288K and Q364R mutants corroborates the prior studies of the homologous mutations found in the ScHCS isozymes.

DISCUSSION

L-lysine Feedback Inhibition of HCS is Competitive with 2-OG

Feedback inhibition of HCS is an important mechanism by which the metabolic flux in the AAA pathway is regulated *in vivo.* Taken together, our structural and functional studies demonstrate L-lysine regulates the activity of SpHCS through competitive inhibition with the substrate 2-OG, in agreement with previous studies of HCS from *P. chrysogenum* (8), *T. thermophilus* (9) and *S. cerevisiae* (7). The flexibility of the enzyme's active site allows differential recognition of 2-OG and L-lysine. This recognition is achieved through conformational changes of the acidic and basic residues in the switch position that form salt bridge interactions and hydrogen bonds to the ε-ammonium group of L-lysine or the C5 carboxylate group of 2-OG, respectively (Figure 3.2). In contrast to the conformal changes between the L-lysine and 2-OG bound complexes, the structures of the SpHCS free enzyme and L-lysine complex are quite similar, especially within the active site (Figure 3.1). This structural similarity implies that the free enzyme may be predisposed to feedback inhibition by L-lysine, providing a molecular explanation for the high affinity of binding of the inhibitor towards the enzyme (Table 3.3). Our findings also show that the salt-bridge interactions between the ε-ammonium group of L-lysine and the carboxylate groups of Asp123 and Glu222 are vital for tight binding, as conservative mutations of these residues completely abolish inhibitor binding *in vitro* and are resistant to AEC *in vivo* (Table 3.3 and Figure 3.5). While this work was under review, coordinates were released for the structure of a TtHCS/L-lysine complex, which also displays competitive binding of L-lysine and 2-OG (22) similar to SpHCS. In summary, our results, along with the *T. thermophilus* structure, provide strong evidence for a competitive model for feedback inhibition of HCS.

Role of the C-terminal L-lysine Insensitive Mutants

Although our results are inconsistent with an allosteric model of inhibition, they do not exclude the possibility of the involvement of residues outside the active site in feedback regulation. Although located in the C-terminal domain ~25 Å away from the active site, the SpHCS R288K and Q364R mutations caused a reduced sensitivity to L-lysine feedback inhibition *in vitro* and *in vivo* (Table 3.3 and Figure 3.5). Because these residues are not involved in stabilization of the dimer interface (Figure 3.7C), it is likely that these residues alter the local conformational dynamics of the enzyme by disrupting hydrogen bonding within the C-terminal domain. These disruptions may affect the equilibrium between the conformation of the free enzyme and L-lysine complex versus the 2-OG complex (Figure 3.1 and 3.2), affecting the binding of L-lysine that preferentially recognizes the conformation adopted by the free enzyme (Figure 3.1). Alternatively, HCS may exhibit half-site reactivity between its two active sites in the homodimer in which L-lysine inhibition of one subunit induces an allosteric signal that results in inhibition of the other subunit. This type of inhibition may not exhibit allosteric kinetics as shown in other homodimeric enzymes, such as prostaglandin endoperoxide H synthases (23-25). Further studies are needed to determine if HCS functions in a similar manner.

Comparison of the Regulatory Mechanisms of HCS and α-IPMS

A comparison of SpHCS and the related enzyme *Mycobacterium tuberculosis* α-IPMS provides insights into the evolution of regulatory mechanisms of these two enzymes. α-IPMS catalyzes a mixed Claisen condensation in the first step in leucine biosynthesis by condensing AcCoA and 2-OIV to form α-isopropylmalate, similar to homocitrate production by HCS (26, 27). The catalytic domains of HCS and α-IPMS are structurally similar TIM barrel folds, and the active site residues involved in metal coordination, substrate binding and catalysis are mostly conserved in the two enzymes. Both enzymes are subjected to feedback inhibition, however their mechanisms are distinct. Unlike SpHCS, α-IPMS possess a C-terminal regulatory domain that functions to allosterically bind the feedback inhibitor L-leucine (27). This regulatory domain consists of two similar βββα folds, with L-leucine binding in a hydrophobic pocket

formed at the interface of the fold that is located ~50 Å away active site of α-IPMS. Upon leucine binding, a loop region that folds over the amino acid becomes more ordered, however the structure of the active site remaining unchanged compared to the α-IPMS/2-OIV complex. Kinetic studies demonstrate that L-leucine exhibits slow-onset noncompetitive inhibition versus the substrate 2-OIV (28). In contrast, L-lysine exhibits rapid competitive inhibition with 2-OG as demonstrated by our structural and functional studies. These differences may reflect distinct physiological requirements for controlling the metabolic flux of the leucine and lysine biosynthetic pathways by feedback regulation.

Insights into Designing HCS Inhibitors for Use as Antifungals

HCS has been proposed as a novel target for antifungal drug design due to its presence in pathogenic fungal species such as *A. fumigatus*, *C. albicans* and *C. neoformans* (29). Our structural and functional characterization of the SpHCS/L-lysine complex yield important insights in designing inhibitors. Notably, our results show that small molecule competitive regulators, like L-lysine, inhibit HCS activity effectively *in vitro* and *in vivo* (Table 3.3 and Figure 3.5). The flexibility of the residues in the switch position (Figure 3.2) may provide opportunities to identify or design small molecule inhibitors that specifically target conformations adopted by the HCS active site. This approach could yield a diverse set of lead compounds in the development of HCS specific inhibitors.

ACKNOWLEDGEMENTS

I would like to thank our collaborators Lorraine Pillus and her graduate student Erin M. Scott for their work on this project. Specifically, I would like to recognize Erin M. Scott for transforming the *S. cerevisiae* double deletion strain with WT SpHCS and mutants and assaying their growth in the absence and presence of AEC. Additionally, I would like to thank Spencer Anderson for his assistance in X-ray data collection at LS-CAT Sector 21.

REFERENCES

1. Xu, H., Andi, B., Qian, J., West, A. H., and Cook, P. F. (2006) The alpha-aminoadipate pathway for lysine biosynthesis in fungi, *Cell Biochem. Biophys. 46*, 43-64.

2. Wolfner, M., Yep, D., Messenguy, F., and Fink, G. R. (1975) Integration of amino acid biosynthesis into the cell cycle of Saccharomyces cerevisiae, *J. Mol. Biol. 96*, 273-290.

3. Ramos, F., Dubois, E., and Pierard, A. (1988) Control of enzyme synthesis in the lysine biosynthetic pathway of Saccharomyces cerevisiae. Evidence for a regulatory role of gene LYS14, *Eur. J. Biochem. 171*, 171-176.

4. Urrestarazu, L. A., Borell, C. W., and Bhattacharjee, J. K. (1985) General and specific controls of lysine biosynthesis in Saccharomyces cerevisiae, *Curr. Genet. 9*, 341-344.

5. Becker, B., Feller, A., el Alami, M., Dubois, E., and Pierard, A. (1998) A nonameric core sequence is required upstream of the LYS genes of Saccharomyces cerevisiae for Lys14p-mediated activation and apparent repression by lysine, *Mol. Microbiol. 29*, 151-163.

6. Feller, A., Ramos, F., Pierard, A., and Dubois, E. (1999) In Saccharomyces cerevisae, feedback inhibition of homocitrate synthase isoenzymes by lysine modulates the activation of LYS gene expression by Lys14p, *Eur. J. Biochem. 261*, 163-170.

7. Andi, B., West, A. H., and Cook, P. F. (2005) Regulatory mechanism of histidine-tagged homocitrate synthase from Saccharomyces cerevisiae. I. Kinetic studies, *The Journal of biological chemistry 280*, 31624-31632.

8. Jaklitsch, W. M., and Kubicek, C. P. (1990) Homocitrate synthase from Penicillium chrysogenum. Localization, purification of the cytosolic isoenzyme, and sensitivity to lysine, *The Biochemical journal 269*, 247-253.

9. Wulandari, A. P., Miyazaki, J., Kobashi, N., Nishiyama, M., Hoshino, T., and Yamane, H. (2002) Characterization of bacterial homocitrate synthase involved in lysine biosynthesis, *FEBS letters 522*, 35-40.

10. Gaillardin, C. M., Poirier, L., and Heslot, H. (1976) A kinetic study of homocitrate synthetase activity in the yeast Saccharomycopsis lipolytica, *Biochim. Biophys. Acta 422*, 390-406.

11. Otwinowski, Z., and Minor, W. (1997) Processing of X-ray Diffraction Data Collected in Oscillation Mode, *Methods Enzymol. 276*, 307-326.

12. Vagin, A. A., Teplyakov, A. (1997) MOLREP: an automated program for molecular replacement., *J. Appl. Crystallogr. 30*, 1022-1025.

13. Emsley, P., and Cowtan, K. (2004) Coot: model-building tools for molecular graphics, *Acta Crystallogr., Sect D: Biol. Crystallogr. 60*, 2126-2132.

14. Murshudov, G. N., Vagin, A. A., and Dodson, E. J. (1997) Refinement of macromolecular structures by the maximum-likelihood method, *Acta Crystallogr., Sect D: Biol. Crystallogr. 53*, 240-255.

15. Davis, I. W., Leaver-Fay, A., Chen, V. B., Block, J. N., Kapral, G. J., Wang, X., Murray, L. W., Arendall, W. B., 3rd, Snoeyink, J., Richardson, J. S., and Richardson, D. C. (2007) MolProbity: all-atom contacts and structure validation for proteins and nucleic acids, *Nucleic Acids Res. 35*, W375-383.

16. Brunger, A. T. (2007) Version 1.2 of the Crystallography and NMR system, *Nat. Protoc. 2*, 2728-2733.

17. Brunger, A. T., Adams, P. D., Clore, G. M., DeLano, W. L., Gros, P., Grosse-Kunstleve, R. W., Jiang, J. S., Kuszewski, J., Nilges, M., Pannu, N. S., Read, R. J., Rice, L. M., Simonson, T., and Warren, G. L. (1998) Crystallography & NMR system: A new software suite for macromolecular structure determination, *Acta Crystallogr., Sect D: Biol. Crystallogr. 54*, 905-921.

18. Andi, B., West, A. H., and Cook, P. F. (2004) Kinetic mechanism of histidine-tagged homocitrate synthase from Saccharomyces cerevisiae, *Biochemistry 43*, 11790-11795.

19. Hans, M. A., Heinzle, E., and Wittmann, C. (2001) Quantification of intracellular amino acids in batch cultures of Saccharomyces cerevisiae, *Appl. Microbiol. Biotechnol. 56*, 776-779.

20. Hans, M. A., Heinzle, E., and Wittmann, C. (2003) Free intracellular amino acid pools during autonomous oscillations in Saccharomyces cerevisiae, *Biotechnol. Bioeng. 82*, 143-151.

21. Zwolshen, J. H., and Bhattacharjee, J. K. (1981) Genetic and biochemical properties of thialysine-resistant mutants of Saccharomyces cerevisiae, *J. Gen. Microbiol. 122*, 281-287.

22. Okada, T., Tomita, T., Wulandari, A. P., Kuzuyama, T., and Nishiyama, M. (2009) Mechanism of substrate recognition and insight into feedback inhibition of homocitrate synthase from thermus thermophilus, *J. Biol. Chem.*

23. Rimon, G., Sidhu, R. S., Lauver, D. A., Lee, J. Y., Sharma, N. P., Yuan, C., Frieler, R. A., Trievel, R. C., Lucchesi, B. R., and Smith, W. L. (2009) Coxibs interfere with the action of aspirin by binding tightly to one monomer of cyclooxygenase-1, *Proc. Natl. Acad. Sci. U.S.A.*

24. Yuan, C., Rieke, C. J., Rimon, G., Wingerd, B. A., and Smith, W. L. (2006) Partnering between monomers of cyclooxygenase-2 homodimers, *Proc. Natl. Acad. Sci. U.S.A. 103*, 6142-6147.

25. Yuan, C., Sidhu, R. S., Kuklev, D. V., Kado, Y., Wada, M., Song, I., and Smith, W. L. (2009) Cyclooxygenase Allosterism, Fatty Acid-mediated Cross-talk between Monomers of Cyclooxygenase Homodimers, *J. Biol. Chem. 284*, 10046-10055.

26. de Carvalho, L. P., and Blanchard, J. S. (2006) Kinetic and chemical mechanism of alpha-isopropylmalate synthase from Mycobacterium tuberculosis, *Biochemistry 45*, 8988-8999.

27. Koon, N., Squire, C. J., and Baker, E. N. (2004) Crystal structure of LeuA from Mycobacterium tuberculosis, a key enzyme in leucine biosynthesis, *Proc. Natl. Acad. Sci. U.S.A. 101*, 8295-8300.

28. de Carvalho, L. P., Argyrou, A., and Blanchard, J. S. (2005) Slow-onset feedback inhibition: inhibition of Mycobacterium tuberculosis alpha-isopropylmalate synthase by L-leucine, *J. Am. Chem. Soc. 127*, 10004-10005.

29. Garrad, R. C., and Bhattacharjee, J. K. (1992) Lysine biosynthesis in selected pathogenic fungi: characterization of lysine auxotrophs and the cloned LYS1 gene of Candida albicans, *J. Bacteriol. 174*, 7379-7384.

CHAPTER 4
HIGH-THROUGHPUT SCREENING FOR SMALL MOLECULE INHIBITORS OF HOMOCITRATE SYNTHASE

Over the last few decades, invasive fungal infections have emerged as a threat to human health. Although these types of infections pose little risk to healthy individuals, they occur frequently and have a high rate of morbidity and mortality in those with compromised immune systems, such as burn patients, recent transplant recipients, individuals undergoing cancer treatments, and those with immunodeficiencies such as HIV and AIDS (1-4). Recently, considerable advances have been made in discovering new fungicides and novel antifungal targets, however current treatments remain unsatisfactory (5-8). For example, existing treatments for infections caused by *Aspergillus* have a cure rate of only 50% (8). In addition, many of the present antifungal treatments have additional shortcomings including serious side effects, numerous drug-drug interactions, or ineffectiveness against resistant infections (5-8). For these reasons, further development of new therapies is needed, especially against novel antifungal targets.

One potential target for the development of new fungal drugs is the AAA pathway of lysine biosynthesis that is utilized in fungi, including the pathogenic species *C. albicans*, *C. neoformans* and *A. fumigatus* (9). Recent studies in *A. fumigatus*, determined the AAA pathway enzymes HAc, SD and HCS to be essential genes and thus possible antifungal targets (10, 11). Although prior work has examined rationally designed inhibitors of HIDH and HAc, the second and third enzyme in this biosynthetic pathway (12, 13), there is still a precedence to further identify and characterize inhibitors to other enzymes in this pathway. In this work, we chose to identify inhibitors of HCS, a divalent metal dependent enzyme that catalyzes the first and committed step in the AAA pathway by condensing 2-OG and AcCoA to form homocitrate. Additionally, HCS plays a critical role in the metabolic flux through the pathway due to its feedback inhibition by the end product L-lysine (14-16). Because of its importance in the AAA pathway, and its

absence in human hosts, HCS represents an attractive target for the development of novel antifungals.

Here we identify inhibitors to SpHCS utilizing an *in vitro* high-throughput screening (HTS) technique. The fluorescent HCS assay (Chapter 2) was optimized for use in a 384-well plate format and the University of Michigan's Center for Chemical Genomics (CCG) library of ~50,000 compounds was screened for their ability to inhibit SpHCS. The initial hits from the first stage of HTS were subjected to confirmation screens and counter screens to eliminate compounds that displayed fluorescence-quenching properties or acted as metal chelators. After completion of the second phase of screening, 341 potential inhibitors remained. We plan to further test these molecules using an *in vivo* yeast growth assay and will confirm the potency of the compound that inhibit growth by dose response curves. We envision that this approach will yield small molecule HCS inhibitors that can be potentially optimized as lead compounds in the development of new antifungal drugs or as molecular probes to study HCS function *in vivo*.

MATERIALS AND METHODS

Materials

The Zn(II)-bound WT SpHCS used in all of the HTS assays. Enzyme from two different 1 L cell pellets were purified by Zn(II) IMAC, and were pooled and purified on a size exclusion column as described in Chapter 2. Nunc brand black 384-well polypropylene microliter plates (Thermo Fisher Scientific) were used for all HTS experiments. A 1 M solution of HEPES buffer (99.5% purity Sigma) was prepared and brought to pH 7.5 with a 5 M solution of potassium hydroxide (Acros Organics) for use in the HTS assays. The 2-OG disodium salt, AcCoA and CoA trilithium salts and Thiostar fluorescent reporter reagent were prepared as described in Chapter 2. MnCl tetrahydrate (Acros Organics) was prepared as a 0.2 M stock for use in the secondary HTS, and anhydrous DMSO (Fluka or Acros Organics) was used in all of the HTS assays.

The library compounds used in the HTS were obtained from the CCG. The library consists of 53,906 compounds from several commercially available screens including a ~16,000 Hit-finder compound collection from Maybridge Chemical, a ~3200 library from Chembridge, the FDA approved MS Spectrum library that contains 2000 compounds and a >20,000 compound library from ChemDiv. A screen of natural products generated in the lab of David Sherman (University of Michigan) was also included in the CCG's library.

Miniaturization of the HCS Fluorescent Assay

The HCS fluorescent assay (Chapter 2) was optimized for use in 384-well format for HTS to test for small molecule inhibitors to SpHCS. Briefly, this assays detects HCS activity by reacting CoA-SH with a thiol-sensitive dye ThioStar to form a fluorescent ThioStar-CoA adduct (see Scheme 2.1) and was used to determine the steady state kinetic parameters and L-lysine inhibition kinetics of WT SpHCS and mutations involved in both catalysis and regulation (Chapters 2 and 3). Controls were performed on Zn(II) purified WT SpHCS using the conditions of the standard HCS fluorescent assay (Chapter 2) to determine if it would be amenable for HTS. First, the stability of the enzyme at room temperature was determined by incubating SpHCS (40 nM) at room temperature for 0-60 min and assaying for activity at saturating substrates. Next, the effect of DMSO on HCS activity was measured using 10 nM WT SpHCS, saturating concentrations of substrates (2 mM 2-OG and 200 μM AcCoA) and 0-2.5% DMSO. Finally, the linearity of the reaction over time at half K_M values for both substrates was examined by measuring HCS activity at various time points up to 20 min using 5.0 or 7.0 nM WT SpHCS, 5.3 μM AcCoA and 80 μM 2-OG.

The HCS High-throughput Screening Protocol

The HCS HTS assay was conducted by adding 20 μl of 100mM HEPES pH 7.5 and 160 μM 2-OG into black polypropylene 384 well microplates (Corning) using an 8-tip multidrop dispenser (Thermo Labsystems). Inhibitor compounds (0.2 μl of 1.2-2 mM stocks) from the CCG's library were added to columns 3-22 of the 384 well plates using the pin-tool application on a Biomek FX (Beckman) liquid handling robot.

At the same time, DMSO was added to the negative (columns 1-2) and positive controls (columns 23-24). A mixture of 100 mM HEPES pH 7.5 and 10.7 μM AcCoA was dispensed into the positive control columns and the assay was initiated with the addition of 20 μl of a mixture of 100 mM HEPES, pH 7.5, 10 nM SpHCS and 10.7 μM AcCoA (columns 1-22) using the 8-tip multidrop dispenser yielding final concentrations of reagents 100 mM HEPES pH 7.5, 80 μM 2-OG, 5.35 μM AcCoA and 5nM SpHCS. The reactions were incubated at room temperature for 20 min and the reaction was stopped with the addition of the reporter reagent (40 μl of 25μM ThioStar in DMSO) to every well using the 8-tip multidrop dispenser. The plates were covered and after a 10 min incubation the fluorescence of the ThioStar-CoA adduct was measured at 460 nm using an excitation wavelength of 380 nm using a PHERAstar (BMG Labs) plate reader.

Counter Screen to Detect ThioStar-CoA Quenching Molecules

A counter screen was performed in triplicate on confirmed hits to ensure that they were not false positives due to quenching of the fluorescence ThioStar-CoA conjugate. This screen was conducted as described for the HTS assay with the following exceptions. Instead of adding a mixture of 100 mM HEPES, pH 7.5, 10 nM SpHCS and 10.7 μM AcCoA to columns 1-22 to initiate the reaction, a solution of 20 μl containing 1 μM CoA (100 mM HEPES, pH 7.5, 1 μM CoA and 10.7 μM AcCoA) was added to mimic the approximate concentration of CoA generated in the negative control reactions. The reporter reagent (40 μl of 25μM ThioStar in DMSO) was immediately added, and the plates were covered and allowed to incubate at room temperature for 10 min before the fluorescence of the ThioStar-CoA adduct was measured.

Secondary Screen to Eliminate Metal Chelators

Analysis of the compound hits revealed that some of them might have metal binding groups. Because the final compound concentration (6-10 μM) is much higher that the enzyme concentration (5 nM) in the HTS assays, compounds that can bind metals may indirectly inhibit HCS by chelating the active site metal. Previous results (Appendix A) illustrate that the active site of SpHCS does not coordinate the metal Mn(II), which was therefore chosen for use in the secondary screen. Control experiments using the

assay conditions of the standard fluorescent HCS assay (Chapter 2) were run in the presence of 0-20 μM Mn(II) and in the presence of 20 μM Mn(II) and 0-20 μM EDTA to examine the activity of the WT SpHCS enzyme in these conditions. To eliminate small molecule metal chelators, a secondary HTS screen was performed in triplicate as described for the HTS with the exception that a mixture of 100 mM HEPES, 160 μM 2-OG and 20 μM MnCl was added in the initial step.

HTS Data Analysis

The HTS assay was validated by analyzing the statistics of the positive and negative control reactions, where a positive control indicates complete inhibition and a negative control represents no inhibition. Negative control reactions were performed in half of a 384-well plate using the HTS assay protocol in the absence of inhibitor compounds and the positive controls (SpHCS was omitted in the reactions) was set up identically in the other half of the 384-well plate. The resulting data was then analyzed by calculating the signal to noise ratio, the Z-factor (Z´) (Eq. 1) (17) and the coefficient of variation (CV) (Eq. 2).

$$\text{Eq 1: } Z' = 1-((3SD_{positive} + 3SD_{negative})/(Mean_{negative} - Mean_{positive}))$$

$$\text{Eq 2: } CV = SD_{negative} / Mean_{negative}$$

Active molecules from the initial screen were determined using two different sets of criteria. Standard deviations of both the negative and sample fluorescent values calculated in the CCG's M-screen database. Percent effect values per plate were also computed, with the average of the negative and positive controls were set at 0% and 100% effective, respectively. Compounds with a standard deviation (SD) > 3 and samples with a percent effect to ≥ 30.0% were defined as active. Promiscuous compounds were defined as having a SD > 3.0 in 10 or more previous screens. Confirmation of the active hits was determined by calculating the median and maximum value for each compound (n=3) using the statistical analysis software JMP (SAS Institute INC.). Confirmed compounds had a median value (% by plate) ≥ 30.0%, whereas general promiscuity in this assay was defined as having ≥ 30.0% activity 10 or more previous screens. To eliminate possible fluorescence quenchers and metal chelators, the percent effect values of the median fluorescent value were calculated by plate for these screens.

Compounds that had values ≥ 30.0% were discarded as quenches in the ThioStar-CoA counter screen, whereas compounds that displayed values < 30.0% were rejected as likely chelators in the Mn(II) secondary screen.

RESULTS

Development and Validation of the HCS Fluorescent Assay for HTS

To determine the feasibility of the fluorescent HCS assay for HTS screening of small molecule inhibitors, we conducted a series of control experiments using the standard assay conditions (Chapter 2). First, we verified that SpHCS is stable for at least 1 hour at room temperature (data not shown). Next, we assayed SpHCS in the presence of DMSO, because the small molecule inhibitors will be added to the assay in DMSO at a final volume of 0.5%. Control assays found that the addition of DMSO to the assay had no effect up to 2.0% (Figure 5.1A). Finally, we established that 5 to 7 nM of SpHCS produced a linear velocity up to 20 min in conditions at half substrate K_M values (80 μM 2-OG and 5.53 μM AcCoA) (Chapter 2) (Figure 4.1B). This result was confirmed using the HTS assay protocol (Table 4.1), where up to 10 nM SpHCS displayed linearity over 20 min (Figure 4.1C). Although 10 nM SpHCS exhibited linearity to 20 min using the HTS protocol, we chose to use a final concentration of 5 nM in the assay because it limits AcCoA consumption to 10% of the initial substrate concentration.

After optimizing the HCS fluorescent assay *in vitro* HTS, we validated the assay protocol (Table 4.1) by determining Z´, CV and signal to control ratio values by performing an equal number of positive and negative control reactions in a single 384-well microplate with the positive controls defined as complete inhibition (SpHCS was omitted from the reaction) and negative controls defined as no inhibition (DMSO control reactions). Analysis of the data yields a Z´ and CV values of 0.7, representing an excellent assay where there is a large separation between the sample signal variation and the control signal variation (17). A CV value of 8.5 % and signal to noise ratio of 11.7 are also exceptional statistical control values for an HTS assay.

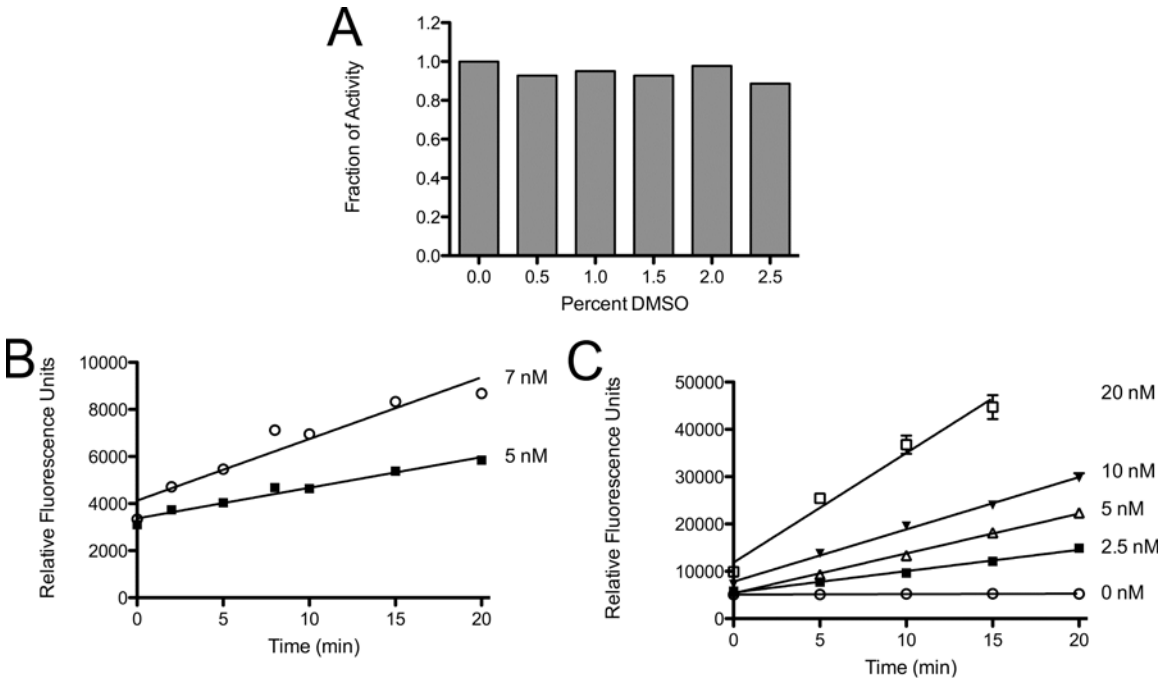

Figure 4.1 Optimization of the fluorescent HCS assay for *in vitro* HTS. **(A)** Fraction of activity relative to no DMSO for WT SpHCS in the presence of increasing concentrations of DMSO. Data represents the average of two replicates. **(B)** Linearity of WT SpHCS in the standard assay conditions (Chapter 2). Linear regressions were fit to the data points that were measured in duplicate. **(C)** Linearity of WT SpHCS using the conditions for the optimized HTS assay (Table 5.1). Linear regressions were fit to the data points (n=8) are with error bars indicating one standard deviation.

Table 4.1 Homocitrate synthase HTS assay protocol.

Step	Paramater	Value	Description
1	Plate 2-OG substrate	20 μL	100 mM HEPES, pH 7.5, 160 μM 2-OG
2	Library compounds	0.2 μL	6 μM to 10 μM in DMSO
3	AcCoA controls	20 μL	100 mM HEPES, pH 7.5, 10.7 μM AcCoA
4	Assay initiation	20 μL	100 mM HEPES, pH 7.5, 10.7 μM AcCoA, 10 nM *S. pombe* HCS
5	Incubation time	20 min	room temperature
6	Reporter reagent	40 μL	25μM ThioStar in DMSO
7	Incubation time	10 min	room temperature
8	Assay readout	380 nM and 460 nM	PHERAstar (BMG Labs) plate reader, fluorescent mode

Step	Notes
1	384-well black polypropoleyne plates (Nunc), 8 tip multidrop 384 dispenser (Thermo Labsystems), added to all columns
2	Pintool transfer with Biomek FX liquid handling robot, DMSO controls were added to control columns 1-2 and 23-24
3	8 tip multidrop 384 dispenser (Thermo Labsystems), added to columns 23-24
4	8 tip multidrop 384 dispenser (Thermo Labsystems), added to columns 1-22
5	
6	8 tip multidrop 384 dispenser (Thermo Labsystems), added to all columns
7	Plates covered with opaque (tinfoil) cover
8	

HTS Primary and Confirmation Screens of CCG's Compound Library

After confirming the reproducibility of the HCS HTS fluorescent assay, we screened the CCG's 53,906 compound library for small molecule inhibitors of HCS. Each test compound was assayed at a single concentration ranging from 6-10 μM with positive and negative controls (n=32) being included in each plate for analysis of the inhibition and to detect any irregularities in the assay (Table 4.1). The scatter plot screening the MS Spectrum 2000 Library (Figure 4.2) is shown as a representation of the HTS results. The Z´ value was calculated by plate and falls with the range of 0.7-0.9 demonstrating the quality of these assays. Following screening of the entire CCG library, a total of 4083 hit compounds were identified as actives by having a SD $\geq$ 3 or a percent effectiveness $\geq$ 30.0 % (Table 4.2). Additional triage was completed to exclude promiscuous compounds, cytotoxic molecules and those containing maleimide groups, which would compete with ThioStar reporter agent for conjugation to CoA. We also eliminated any positive hits that were natural products do to the limited characterization and availability of these compounds. After triage, a total of 1399 compounds were selected for confirmation assays that were performed in triplicate for each molecule. An analysis of data from this screen confirmed 595 actives, defined as having a median percent effect value (% by plate) $\geq$30.0%. Molecules from this set that exhibited general promiscuity or were large compounds with a topological polar surface area value exceeding 140 $Å^2$ were also eliminated (Table 4.2). The number of positive hits remaining after confirmation screening was 514, representing ~1% of the total number of compounds assayed.

ThioStar-CoA Quenching Counter Screen

Inspection of the chemical structures of the positive hits in the HTS confirmation revealed that several of the compounds have large conjugated aromatic systems that may act to quench the ThioStar-CoA adduct formed in the HCS assay. To eliminate false positives due to fluorescence quenching, we conducted an HTS counter screen on 496 of the confirmed actives (eighteen of the confirmed compounds were not screened due to availability concerns) (Table 4.2) by including 1 μM CoA to the initiation step in the assay in place of the SpHCS enzyme (Table 4.1). This concentration of CoA was used to mimic the approximate amount of CoA generated in the negative control reactions.

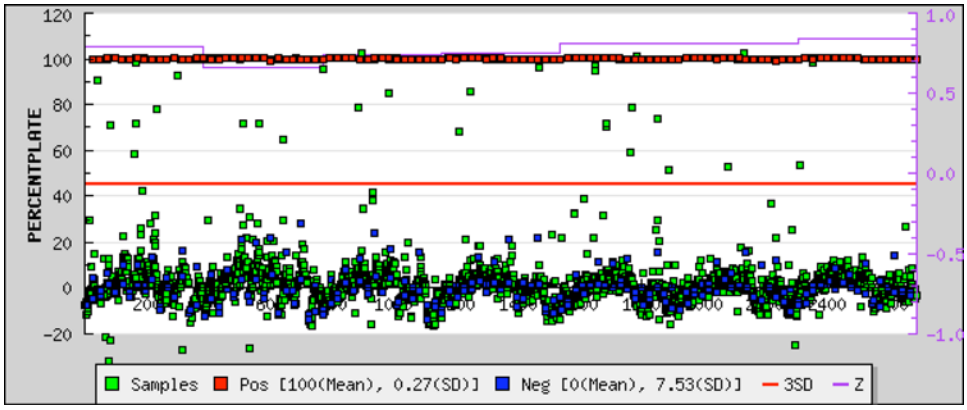

Figure 4.2 Representation of the HTS screening results using the MS Spectrum 2000 compound library. The x-axis corresponds to the compounds screened (green squares) and the positive (red squares) and negative control assays (blue squares). The left y-axis represents percent effectiveness per plate, whereas the right y-axis reports the Z´ value for each plate (purple line). The red line represents 3 SD as calculated from the negative control and samples.

Table 4.2 Results of HTS for inhibitors of HCS.

Compound Category	# of Compounds
Total compounds in primary screen	53,906
Total actives (SD ≥ 3 or % effectiveness ≥ 30.0 %)	4803
Promiscuous compounds (SD ≥ 3 in 10 or more previous assays)	27
Known cytotoxic compounds	216
Maleimide containing compounds	23
Natural Products	3138
Total compounds in confirmation screen	1399
Total actives (median % effectiveness ≥ 30.0 %)	595
Generally promiscuous compounds (% effectiveness ≥ 30.0 % in 10 or more previous assays)	67
Large compounds (TPSA ≥140 $Å^2$)	14
Compounds with limited availability	18
Total compounds in counter and secondary screens	496
ThioStar-CoA quenching compounds (% effectiveness ≥ 30.0 %)	54
Metal chelating compounds (% effectiveness ≤ 30.0 %)	81
Remaining Active Compounds	361
8-hydroxyquinoline containing compounds	20
Compounds to use in follow-up studies	341

Analysis of the ThioStar-CoA counter screen data resulted in the elimination of 54 likely quenchers as defined as having a median percent effect of ≥30.0% (Table 4.2).

Metal Chelator Secondary Screen

Several of the small molecule hits contain heterocyclic rings systems or multiple polar groups, which may function to bind metals. Because HCS requires a divalent metal ion for catalysis and exhibits little activity after removal of the active site metal (Appendix A), it was necessary to eliminate false positives due to metal chelation. Our previous results indicated that SpHCS does not bind the metal Mn(II) (Appendix A), therefore we chose to use this metal in the secondary screen. Before completion of the HTS secondary screen, we first determined the activity of SpHCS in the presence of up to 50 μM $MnCl_2$ and if the addition of the metal could effectively block inhibition by the metal chelator EDTA. Our results indicated that the addition of 20 μM $MnCl_2$ (twice the inhibitor concentration in the HTS assay) caused a modest (~17%) decrease in activity compared to SpHCS assayed with no Mn(II) (Figure 4.3A). Additionally, we found that the addition of Mn(II) effectively blocked metal chelation by EDTA at concentrations equal to or less than half the concentration of Mn(II) (Figure 4.3B). To eliminate potential metal chelators, the secondary screen was performed on 496 of the confirmed actives using the HTS assay protocol (Table 4.1) with the exception that 20 μM $MnCl_2$ was added to the initial step of the assay. Analysis of the data resulted in the exclusion of 81 likely chelators, which exhibited a median percent effect of < 30.0% leaving a total of 361 inhibitor compounds for additional follow up (Table 4.2).

Characteristics of the Compounds which Inhibit HCS

An analysis of the remaining confirmed hits revealed several classes of structurally related compounds, with one of these classes including 20 members that contain an 8-hydroxyquinoline functional group (Figure 4.4), which is a known chelator that can bind a variety of biologically relevant divalent metals (18). Therefore, these compounds will be excluded in further studies leaving a total 341 to be assayed in follow up studies (Table 4.2). Surprisingly, these compounds were not eliminated during the

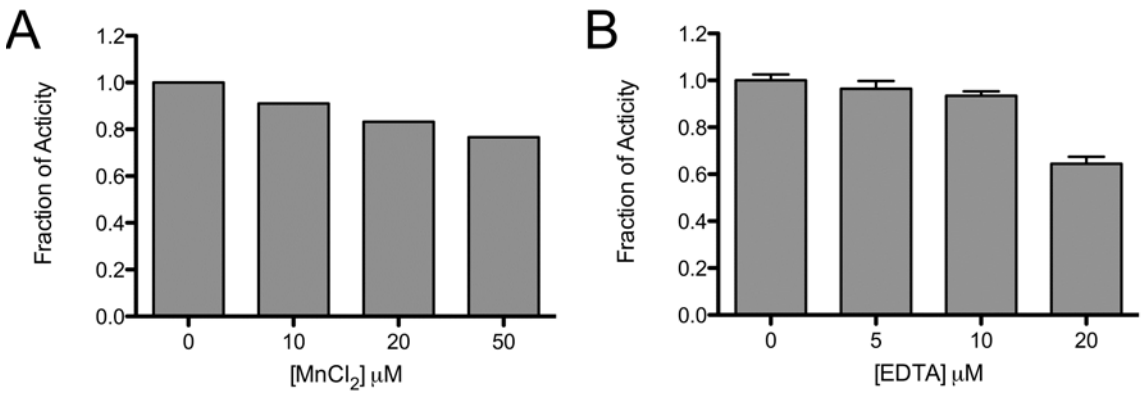

Figure 4.3 HCS control assays for the HTS secondary screen to eliminate metal chelators. (A) The fraction of activity (relative to 0 μM $MnCl_2$) for WT SpHCS in the presence of increasing concentrations of $MnCl_2$. Data are the average of duplicate measurements. **(B)** The fraction of activity (relative to 0 μM EDTA) for WT SpHCS in the presence of 20 μM $MnCl_2$ and increasing concentrations of EDTA. Measurements were performed in triplicate at each data point. Error bars in both graphs indicate one standard deviation.

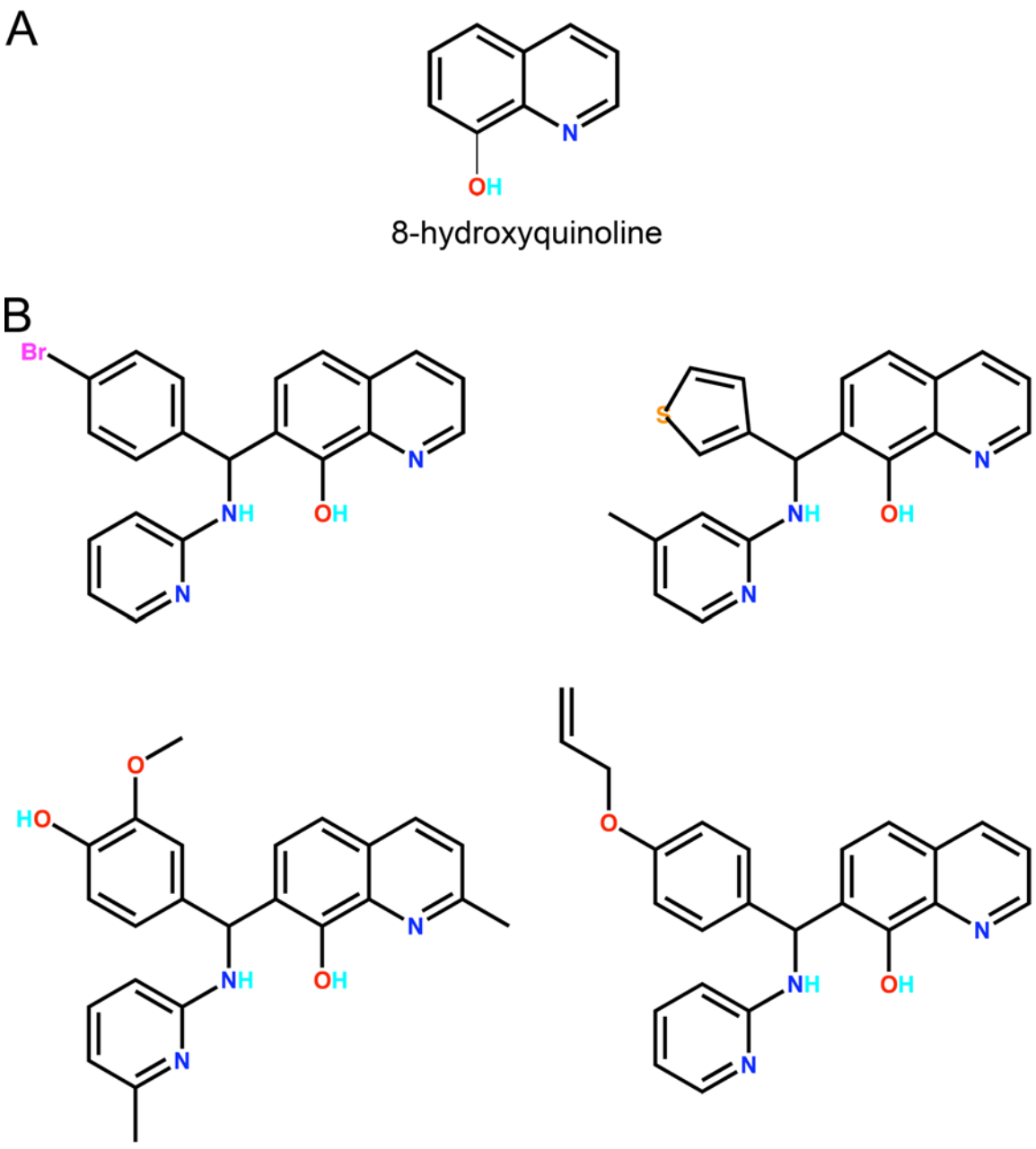

Figure 4.4 Compounds containing an 8-hydroxyquinoline moiety. (A) Structure of 8-hydroxyquinoline. **(B)** Examples of confirmed hits containing this functional group.

Mn(II) counter screen, perhaps because they have a low affinity for Mn(II). The remaining hits included compounds that could be categorized into two structurally similar classes. Class 1 includes 23 compounds (~7% for the total hits) that contain a core three-member ring scaffold with various substitutions on the piperidine and phenol rings (Figure 4.5), whereas Class 2 is made up of 5 members containing a conserved five-member ring scaffold (Figure 4.6). The remaining small molecule inhibitors exhibit greater structural divergence and could not be assigned to a structurally related class. In summary, a diverse set of small molecule inhibitors of SpHCS were detected through HTS including a large set of compounds containing an core three-ring scaffold, which may represent a novel class of HCS inhibitors.

DISCUSSION

HCS is a potential target for antifungal drug design because it is absent in humans, catalyzes the first step in the AAA biosynthetic pathway and controls the metabolic flux of the pathway through L-lysine feedback inhibition. (14-16). In this work, we describe the development of a HTS assay for small molecule inhibitors of SpHCS that was used to effectively screen the CCG's 53,906 compound library. Following conformation screening, 514 inhibitors displayed inhibition towards HCS. These compounds were further reduced to 361 by performing a ThioStar-CoA counter screen and a metal chelation secondary screen. Although the secondary screen removed many compounds containing groups that might act as metal binders, a family of compounds containing the metal binding 8-hydroxyquinoline group escaped elimination (Figure 4.4). This group has been reported to bind Mn(II) at pH 7.0, at a 10:1 ratio of reagent to metal (18), however its binding affinity may to be low to effectively chelate Mn(II) under the conditions of the HTS assay. Alternatively, the substituents attached to the 8-hydroxyquinoline group may decrease the ability of these compounds to chelate all metals resulting in inhibition of SpHCS via an alternative mechanism. Nonetheless, these compounds will be removed from future assays to avoid the possibility that they inactivate SpHCS through chelation of the active site metal. A subset of the 341 remaining compounds belong to two classes of structurally conserved molecules that

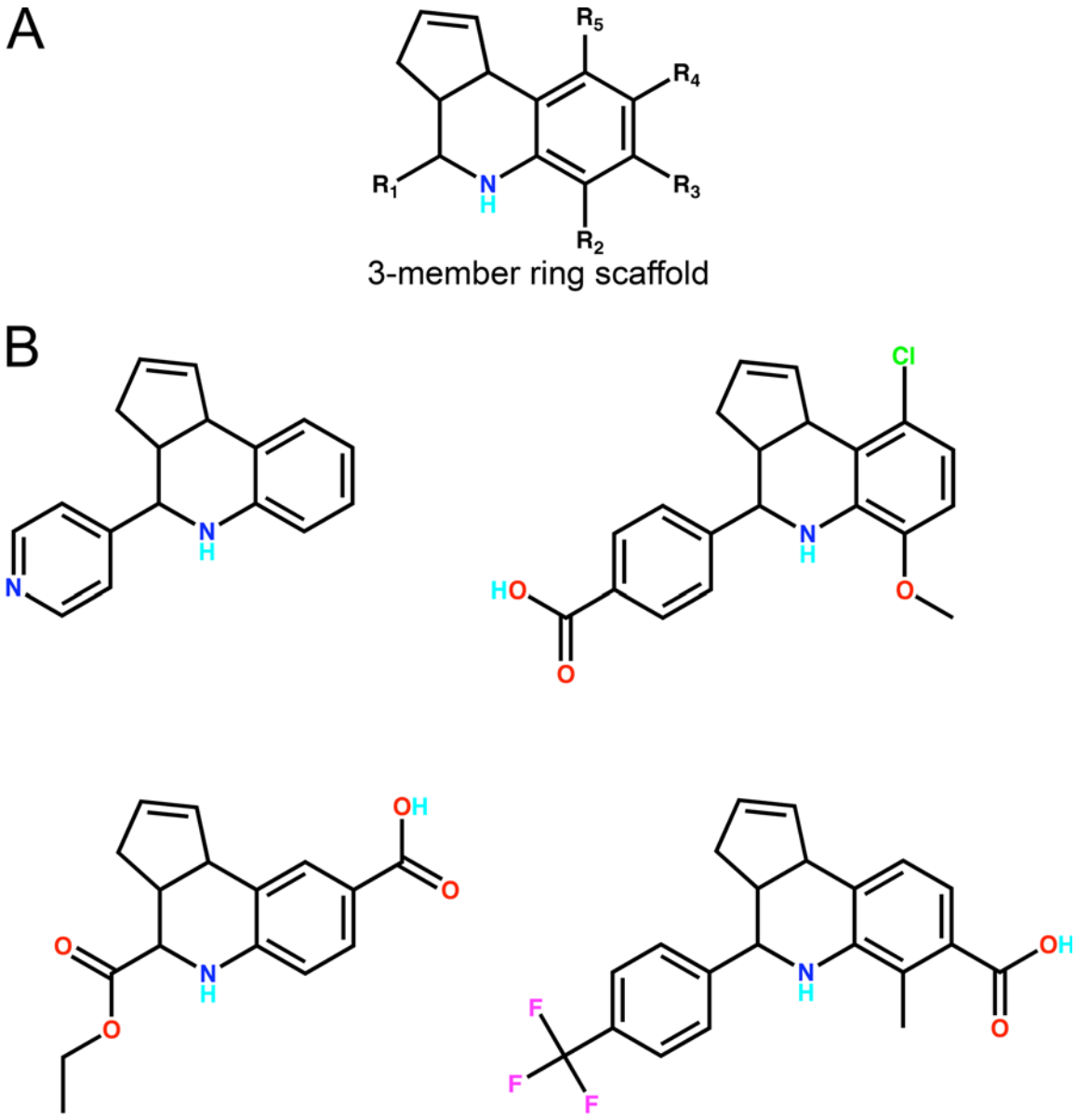

Figure 4.5 Class 1 structurally related compound hits. (A) Conserved scaffold of compounds from Class 1, where R_1 –R_5 denote substituent groups. **(B)** Examples of active hits against HCS with the Class 1 scaffold.

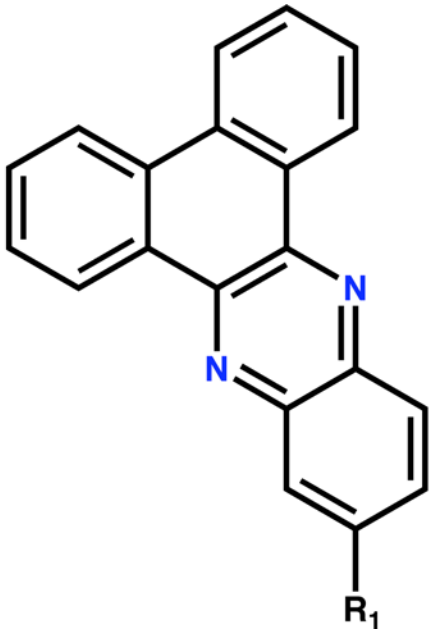

Figure 4.6 Class 2 structurally related compound hits. Conserved 5-member ring scaffold of compounds from Class 2, where R_1 represents various amine-linked substitutions.

might represent novel HCS inhibitors. However, additional studies are still needed to finalize the characterization of these remaining inhibitors. To complete these studies we plan to first screen these compounds *in vivo* for their ability to inhibit the growth of yeast. A counter screen will also be performed to identify compounds that are not specific to SpHCS *in vivo*, but are generally cytotoxic. Finally, the potency of the *in vivo* inhibitors will then be tested *in vitro* and *in vivo* by performing dose response curves. We are optimistic that these additional screens will result in identifying a handful of potent small molecule inhibitors to SpHCS that can be used as lead compounds in developing antifungal drugs.

In addition, our results provide proof-of concept for this HTS strategy that can also be applied to discover inhibitors of HCS from fungal pathogens, including *C. albicans, C. neoformans* and *A. fumigatus* (9). Indeed, the CCG has recently expanded their compound library to ~150,000 small molecule compounds that can be screened for their ability to inhibit HCS from these pathogenic species, using the HTS protocol outlined here. A comparison of inhibitors for each of these species will establish whether these inhibitors are broad-spectrum antifungals or species-specific antifungal agents.

ACKNOWLEDGEMENTS

I would like to kindly thank the staff at the University of Michigan's Center of Chemical Genomics, especially Martha Larsen, Tom McQuade and Paul Kirchoff, for their help on this project. I wish to acknowledge Tom McQuade for his insights into optimizing the HCS assay for HTS, assistance in conducting the HTS assays and helpful discussions. I would like to recognize Paul Kirchoff for assistance in performing the compound triage and Martha Larsen for useful discussion throughout the screening process.

REFERENCES

1. Branski, L. K., Al-Mousawi, A., Rivero, H., Jeschke, M. G., Sanford, A. P., and Herndon, D. N. (2009) Emerging infections in burns, *Surg. Infect. (Larchmt) 10*, 389-397.

2. Kaplan, J. E., Benson, C., Holmes, K. H., Brooks, J. T., Pau, A., and Masur, H. (2009) Guidelines for prevention and treatment of opportunistic infections in HIV-infected adults and adolescents: recommendations from CDC, the National Institutes of Health, and the HIV Medicine Association of the Infectious Diseases Society of America, *MMWR Recomm. Rep. 58*, 1-207; quiz CE201-204.

3. Mofenson, L. M., Brady, M. T., Danner, S. P., Dominguez, K. L., Hazra, R., Handelsman, E., Havens, P., Nesheim, S., Read, J. S., Serchuck, L., and Van Dyke, R. (2009) Guidelines for the Prevention and Treatment of Opportunistic Infections among HIV-exposed and HIV-infected children: recommendations from CDC, the National Institutes of Health, the HIV Medicine Association of the Infectious Diseases Society of America, the Pediatric Infectious Diseases Society, and the American Academy of Pediatrics, *MMWR Recomm. Rep. 58*, 1-166.

4. Walsh, T. J., and Groll, A. H. (1999) Emerging fungal pathogens: evolving challenges to immunocompromised patients for the twenty-first century, *Transpl. Infect. Dis. 1*, 247-261.

5. Enoch, D. A., Ludlam, H. A., and Brown, N. M. (2006) Invasive fungal infections: a review of epidemiology and management options, *J. Med. Microbiol. 55*, 809-818.

6. Mathew, B. P., and Nath, M. (2009) Recent approaches to antifungal therapy for invasive mycoses, *ChemMedChem 4*, 310-323.

7. Peman, J., Canton, E., and Espinel-Ingroff, A. (2009) Antifungal drug resistance mechanisms, *Expert Rev. Anti. Infect. Ther. 7*, 453-460.

8. Rogers, T. R., and Frost, S. (2009) Newer antifungal agents for invasive fungal infections in patients with haematological malignancy, *Br. J. Haematol. 144*, 629-641.

9. Garrad, R. C., and Bhattacharjee, J. K. (1992) Lysine biosynthesis in selected pathogenic fungi: characterization of lysine auxotrophs and the cloned LYS1 gene of Candida albicans, *J. Bacteriol. 174*, 7379-7384.

10. Hu, W., Sillaots, S., Lemieux, S., Davison, J., Kauffman, S., Breton, A., Linteau, A., Xin, C., Bowman, J., Becker, J., Jiang, B., and Roemer, T. (2007) Essential gene identification and drug target prioritization in Aspergillus fumigatus, *PLoS Pathog. 3*, e24.

11. Thykaer, J., Andersen, M. R., and Baker, S. E. (2009) Essential pathway identification: from in silico analysis to potential antifungal targets in Aspergillus fumigatus, *Med. Mycol. 47 Suppl 1*, S80-87.

12. Palmer, D. R., Balogh, H., Ma, G., Zhou, X., Marko, M., and Kaminskyj, S. G. (2004) Synthesis and antifungal properties of compounds which target the alpha-aminoadipate pathway, *Pharmazie 59*, 93-98.

13. Yamamoto, T., and Eguchi, T. (2008) Thiahomoisocitrate: a highly potent inhibitor of homoisocitrate dehydrogenase involved in the alpha-aminoadipate pathway, *Bioorg. Med. Chem. 16*, 3372-3376.

14. Bhattacharjee, J. K. (1985) alpha-Aminoadipate pathway for the biosynthesis of lysine in lower eukaryotes, *Crit. Rev. Microbiol. 12*, 131-151.

15. Xu, H., Andi, B., Qian, J., West, A. H., and Cook, P. F. (2006) The alpha-aminoadipate pathway for lysine biosynthesis in fungi, *Cell Biochem. Biophys. 46*, 43-64.

16. Zabriskie, T. M., and Jackson, M. D. (2000) Lysine biosynthesis and metabolism in fungi, *Nat. Prod. Rep. 17*, 85-97.

17. Zhang, J. H., Chung, T. D., and Oldenburg, K. R. (1999) A Simple Statistical Parameter for Use in Evaluation and Validation of High Throughput Screening Assays, *J Biomol Screen 4*, 67-73.

18. Albert, A., and Gledhill, W. S. (1947) The choice of a chelating agent for inactivating trace metals: I. A survey of commercially available chelating agents, *Biochem. J. 41*, 529-533.

CHAPTER 5
SUMMARY, CONCLUSIONS AND FUTURE DIRECTIONS

Significant progress has been made over the past few decades in understanding the fundamental biochemistry of HCS. Specifically, work on HCS Lys20 from *S. cerevisiae* has provided insights into the kinetic and catalytic mechanism of this enzyme (1-3). Additionally, kinetic studies on ScHCS, PcHCS and TtHCS show that L-lysine feedback regulation is kinetically competitive with the substrate 2-OG (4-7). However, prior to this work the mechanism by which L-lysine is recognized remained unknown. The work presented here focuses on using structural and biochemical studies to elucidate the mechanistic details of catalysis and regulation of HCS. In addition, these studies have furnished the basis to develop a HTS assay to identify small molecule inhibitors to this enzyme, which may serve as lead compounds in the development of antifungal drugs.

Substrate Binding and Catalytic Mechanism of HCS

While a general acid-base Claisen condensation chemical mechanism has been proposed for HCS (3), the mechanistic details, including the residues that may act as the catalytic acid and base, remained speculative in part due to a lack of a structure of a HCS enzyme. In Chapter 2, the structures of SpHCS and two different SpHCS/2-OG complexes are described. Because these are the first HCS structures to be reported, they provide invaluable insights into the identity of the residues involved in substrate recognition and catalysis. The structures illustrate that HCS forms a homodimer that is stabilized by domain swapping between the N and C-terminal domains of each monomer. The N-terminal catalytic domain is composed of a $(\alpha/\beta)_8$ TIM barrel fold in which 2-OG binds via hydrogen bonds and coordination to the active site divalent metal ion. Biochemical studies performed in Chapter 2 reveal that nearly all of the tested 2-OG binding mutations either impaired or abolished activity, illustrating that interactions to

both the C1 and C5 carboxylate groups of 2-OG are vital for proper substrate binding within the active site.

The structural studies on HCS described in Chapter 2 also provide some unexpected findings. For example, in the free enzyme structure and one of the 2-OG complexes, a lid motif in the C-terminal domain covers the entrance of the active of the neighboring monomer, whereas in the second 2-OG complex the lid motif is disordered. When closed, the lid motif forms two 3_{10} helices that completely occlude 2-OG and AcCoA binding, implying that it regulates substrate access to the active site through its apparent plasticity. The flexibility of this conserved region (Figure 2.10) is also observed in the TtHCS structures (6). The lid motif in the TtHCS/L-lysine complex has a similar location to the lid motif seen in the closed SpHCS/2-OG and L-lysine complexes (Figure 6.1A, 6.1B and 6.1C), however an alternative conformation in this motif is observed in the TtHCS/2-OG complexes. Instead of forming a 3_{10} helix that occludes the entrance to the active site of the neighboring monomer, the lid motif rearranges into a longer α-helix followed by a 3_{10} helix that does not cover the active site of the neighboring monomer (Figure 6.1D).

Additionally, this conformational change causes a rearrangement of residues implicated in base catalysis. Based on the sequence homology to α-IPMS, mutagenesis and biochemical studies on conserved ScHCS Lys20 active site residues suggested that a glutamate-histidine dyad acts as the general base in deprotonation of the methyl group of AcCoA to form an enol (or enolate) (2, 8). Although our structural and biochemical studies of SpHCS support a role for the glutamate residue (Glu167) in catalysis, the corresponding histidine (His321′), which is located in the lid motif, is located too far away from Glu167 to form a functional catalytic dyad. However, it is possible that upon AcCoA binding a conformational change could take place to bring the histidine residue within a distance to act in base catalysis. Indeed, the recently published structures TtHCS illustrates that the lid motif adopts a conformation that orients the histidine so that it may function as the glutamate-histidine dyad (Glu137-His292′) in base catalysis (6) (Figure 6.1D). The conservation of this dyad in α-IPMS and TtHCS but not in SpHCS may either indicate that the structure of SpHCS is not in a catalytically active form, or there may be evolutionally differences in catalysis in HCS from archaebacteria and fungi. Future

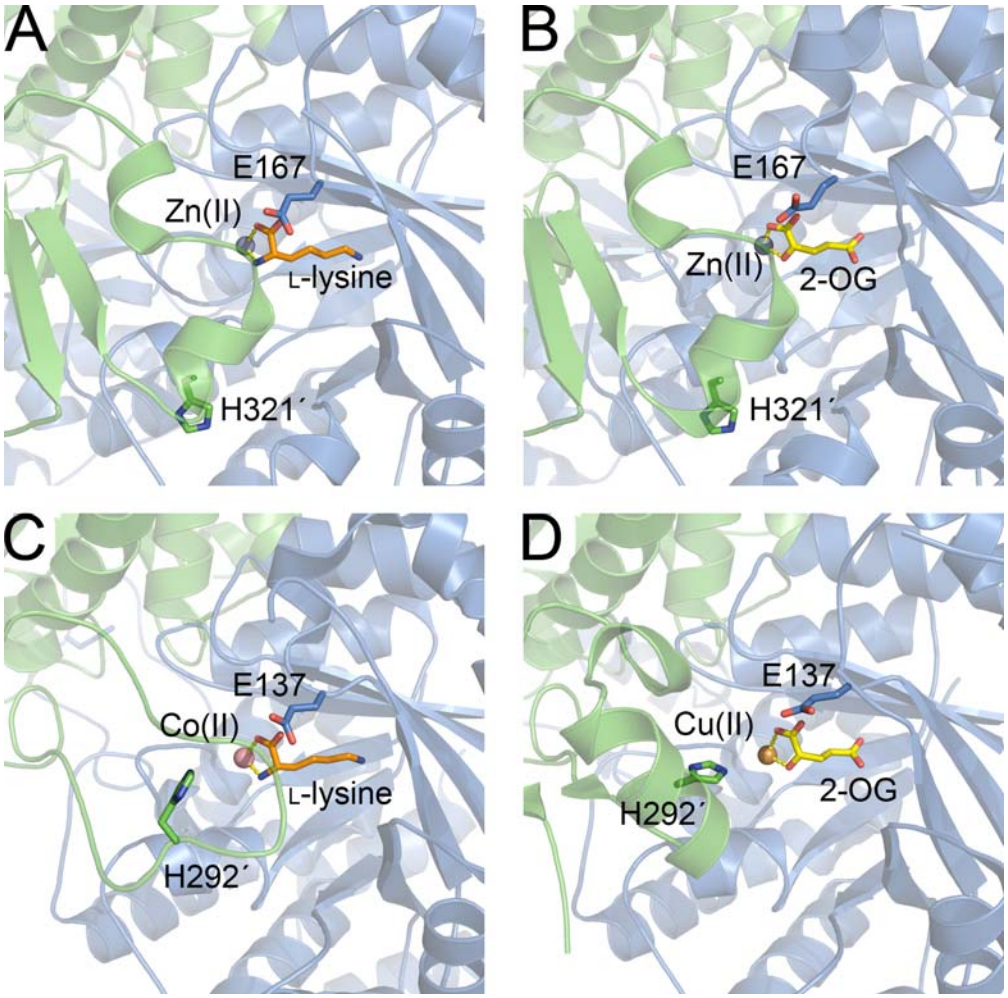

Figure 6.1 Arrangements of the lid motif in SpHCS and TtHCS. (A, B) SpHCS in complex with L-lysine (orange) (A) and 2-OG (yellow) (B). Monomer A and B are colored blue and green respectively, whereas the Zn(II) metal ions (grey) are shown as spheres. In theses structures the lid motif forms the two 3_{10} helices. **(C)** TtHCS/L-lysine complex (PDB 3A9I) with monomer A, monomer B and L-lysine colored as described in panel (A). The Co(II) ion is depicted as a pink sphere. **(D)** TtHCS (monomer A and B colored blue and green, respectively) in complex with 2-OG (yellow) (PDB 2ZTJ). In this structure the lid motif forms a longer α-helix followed by a short 3_{10} helix.

studies are needed to determine if a similar arrangement of the lid motif, and thus the movement of the histidine residue implicated in catalysis occurs in SpHCS and other fungal HCS homologs.

Although this work furnishes a greater understanding of the substrate specificity and catalytic mechanism of HCS, several important mechanistic questions regarding the binding of AcCoA remain. For example, we do not fully understand the conformational changes that take place in the lid motif to accommodate AcCoA binding, nor do we know the interactions between AcCoA and the protein that occur to orient the substrates for catalysis. Solving a ternary complex of SpHCS would provide invaluable information towards answering these types of questions. We were unable to obtain a structure of a ternary complex using WT SpHCS in the presence of 2-OG and either CoA or acetonyl-CoA, a non-reactive analog of AcCoA, nor from the addition of 2-OG and AcCoA to the catalytically inactive E167Q SpHCS mutant (Chapter 2). However, future studies in which SpHCS is crystallized with non-hydrolysable homocitryl-CoA analogs may yield a ternary complex that can then be functionally characterized to determine the residues that are important for AcCoA binding and catalysis. Alternatively, perhaps another HCS homolog would be more amenable for crystallization in a ternary complex. Solving a binary complex of HCS with homocitryl-CoA analogs will not only provide further insights into the mechanism, but may also serve as a starting point for structure-based design of potent HCS-specific inhibitors that may be developed into antifungal modulators.

Regulation of HCS by L-lysine

Another distinctive finding that arose from our structural and biochemical work on SpHCS is the discovery that the substrate 2-OG and the feedback inhibitor L-lysine bind competitively in the same $(\alpha/\beta)_8$ TIM barrel active site (Chapter 3). Although feedback inhibition can be kinetically competitive, in most of these cases the inhibitor binds to an alternative binding site which causes an allosteric change in the protein which no longer allows the substrate to bind (9). This is not surprising considering the structural differences between the inhibiting intermediate or end product in the pathway and enzyme's substrate. In fact, competitive binding of a feedback inhibition to the same site

as the substrate appears to be quite rare. However it does occur in some enzymes including glutamate synthase, with structural and biochemical studies demonstrating that the L-serine, L-alanine and glycine are competitive inhibitors with the enzyme's substrate L-glutamate (10). In HCS, differential recognition of the substrate and inhibitor is achieved via a switch position within the active site of the enzyme that can distinguish between the C5 carboxylate group of 2-OG and the ε-ammonium group of L-lysine. Mutagenesis of the residues in the switch region that form hydrogen bonds to the ε-ammonium moiety of L-lysine completely abolish feedback inhibition *in vitro* and *in vivo*, indicating their importance in the regulation of HCS. Recently, the structure of a TtHCS/L-lysine complex was also reported. This enzyme has an inhibitor-binding mode that is essentially identical to that of SpHCS, illustrating conservation of the feedback regulatory mechanism of HCS (Figure 5.1C and 5.1D).

Our structural and biochemical results indicate that L-lysine is a competitive inhibitor toward 2-OG. However, in agreement with finding in ScHCS (11), two mutations in the C-terminal domain of SpHCS also decrease the enzymes sensitive to inhibition. These mutations are too far away from the active site to have a direct effect on L-lysine binding, but may change the enzyme's conformational dynamics to favor substrate binding. Alternatively, the enzyme may exhibit half-site reactivity, where binding of L-lysine to inhibit one monomer transmits a conformational change that inhibits the other monomer, with these C-terminal residues being part of the network that relays this allosteric signal. Similar to work reported on prostaglandin endoperoxide H synthase (12), future studies are needed to investigate the function a heterodimer of WT SpHCS and the L-lysine insensitive D123N mutation to determine if HCS exhibits allosteric feedback inhibition through half-site reactivity.

Identification of small molecule inhibitors of HCS

Although the enzymes in the AAA pathway have long been considered targets for antifungal drug design (13), Chapter 4 is the first reported study to identify inhibitors of HCS, the first enzyme in this pathway. In this work, we developed an HTS protocol to identify small molecule inhibitors of HCS by modifying the fluorescent assay used for the biochemical characterization of HCS presented in Chapters 2 and 3. This assay was

used to screen the CCG's library of 53,906 compounds that resulted in the preliminary identification of 341 compounds that inhibit SpHCS. These compounds may represent novel classes of HCS inhibitors, however further studies are needed to finalize the characterization of these molecules. To complete these studies, we plan to first screen these compounds *in vivo* for their ability to inhibit growth in the *lys4*$^{+}$ transformed *S. cerevisiae lys20Δ lys21Δ* deletion strain (Chapter 2) containing an additional *PDR5* gene deletion. The *PDR5* gene encodes a major pleiotropic ABC drug transporter, which causes the efflux of many drugs resulting in acquired drug resistance (14). This deletion strain will provide a convenient model strain that will negate the effects of multidrug transport while assaying SpHCS inhibitor compounds for *in vivo* potency and cell permeability. To identify compounds that are not specific to SpHCS *in vivo*, we will also perform a counter screen in which the cells are grown in media supplemented with L-lysine to identify generally cytotoxic compounds. The potency of the inhibitors confirmed in the *in vivo* screen will then be tested *in vitro* and *in vivo* by performing dose response curves in triplicate. We are optimistic that these additional screens will identify potent small molecule inhibitors to SpHCS, which can be used as lead compounds for antifungal therapies and to serve as molecular probes to further characterize HCS's function *in vivo.*

The results from this HTS assay not only demonstrate the feasibility of this approach but also provide a foundation for discovering inhibitors of HCS from fungal pathogens including *C. albicans, C. neoformans* and *A. fumigatus.* Indeed, *C. albicans* (CaHCS) Lys212 gene was obtained from the Pillus lab, cloned into a bacterial expression vector and purified using Co(II) IMAC and size exclusion chromatography as reported for SpHCS as described in Appendix B (Figure B.1). The steady state kinetic parameters of CaHCS Lys212 were also determined and found to be similar to the values for Co(II)-SpHCS (Appendix B and Table A.2). These preliminary studies on CaHCS Lys212 indicated that this enzyme is amenable to HTS using the CCG's expanded 150,000 compound library. It will be interesting to see if the inhibitors to SpHCS and CaHCS are similar or species specific.

Additionally, inhibitors identified through HTS may also serve as a probe to further investigate the function of HCS *in vitro* and *in vivo*. Solving HCS/inhibitor

complexes would provide insights into the mechanism of regulation by these inhibitors. These structural studies in conjunction with functional studies to determine the kinetic mechanism of regulation by these HCS inhibitors, will allow for the structure based design and synthesis of additional lead compounds that could be used to develop novel antifungal modulators. Not only will these antifungals have the potential to treat human fungal infections, but they could also be used to fight fungi such as the *Aspergillus* that threaten several agricultural crops including corn, cotton and peanuts (15, 16).

REFERENCES

1. Andi, B., West, A. H., and Cook, P. F. (2004) Kinetic mechanism of histidine-tagged homocitrate synthase from Saccharomyces cerevisiae, *Biochemistry 43*, 11790-11795.

2. Qian, J., Khandogin, J., West, A. H., and Cook, P. F. (2008) Evidence for a catalytic dyad in the active site of homocitrate synthase from Saccharomyces cerevisiae, *Biochemistry 47*, 6851-6858.

3. Qian, J., West, A. H., and Cook, P. F. (2006) Acid-base chemical mechanism of homocitrate synthase from Saccharomyces cerevisiae, *Biochemistry 45*, 12136-12143.

4. Andi, B., West, A. H., and Cook, P. F. (2005) Regulatory mechanism of histidine-tagged homocitrate synthase from Saccharomyces cerevisiae. I. Kinetic studies, *J. Biol. Chem. 280*, 31624-31632.

5. Jaklitsch, W. M., and Kubicek, C. P. (1990) Homocitrate synthase from Penicillium chrysogenum. Localization, purification of the cytosolic isoenzyme, and sensitivity to lysine, *Biochem. J. 269*, 247-253.

6. Okada, T., Tomita, T., Wulandari, A. P., Kuzuyama, T., and Nishiyama, M. (2009) Mechanism of substrate recognition and insight into feedback inhibition of homocitrate synthase from thermus thermophilus, *J. Biol. Chem.*

7. Wulandari, A. P., Miyazaki, J., Kobashi, N., Nishiyama, M., Hoshino, T., and Yamane, H. (2002) Characterization of bacterial homocitrate synthase involved in lysine biosynthesis, *FEBS Lett. 522*, 35-40.

8. Koon, N., Squire, C. J., and Baker, E. N. (2004) Crystal structure of LeuA from Mycobacterium tuberculosis, a key enzyme in leucine biosynthesis, *Proc. Natl. Acad. Sci. U.S.A. 101*, 8295-8300.

9. Gerhart, J. C., and Pardee, A. B. (1962) The enzymology of control by feedback inhibition, *J. Biol. Chem. 237*, 891-896.

10. Liaw, S. H., Pan, C., and Eisenberg, D. (1993) Feedback inhibition of fully unadenylylated glutamine synthetase from Salmonella typhimurium by glycine, alanine, and serine, *Proc. Natl. Acad. Sci. U.S.A. 90*, 4996-5000.

11. Feller, A., Ramos, F., Pierard, A., and Dubois, E. (1999) In Saccharomyces cerevisae, feedback inhibition of homocitrate synthase isoenzymes by lysine modulates the activation of LYS gene expression by Lys14p, *Eur. J. Biochem. 261*, 163-170.

12. Yuan, C., Rieke, C. J., Rimon, G., Wingerd, B. A., and Smith, W. L. (2006) Partnering between monomers of cyclooxygenase-2 homodimers, *Proc. Natl. Acad. Sci. U.S.A. 103*, 6142-6147.

13. Garrad, R. C., and Bhattacharjee, J. K. (1992) Lysine biosynthesis in selected pathogenic fungi: characterization of lysine auxotrophs and the cloned LYS1 gene of Candida albicans, *J. Bacteriol. 174*, 7379-7384.

14. Sipos, G., and Kuchler, K. (2006) Fungal ATP-binding cassette (ABC) transporters in drug resistance & detoxification, *Curr Drug Targets 7*, 471-481.

15. Yu, J., Cleveland, T. E., Nierman, W. C., and Bennett, J. W. (2005) Aspergillus flavus genomics: gateway to human and animal health, food safety, and crop resistance to diseases, *Rev Iberoam Micol 22*, 194-202.

16. De Lucca, A. J. (2007) Harmful fungi in both agriculture and medicine, *Rev Iberoam Micol 24*, 3-13.

APPENDIX A
DIVALENT METAL ION SPECIFICITY FOR THE ACTIVITY AND FEEDBACK INHIBITION OF HOMOCITRATE SYNTHASE

HCS belongs to a group of enzymes that includes citrate synthase (1-3), malate synthase (4, 5) and α-IPMS (6, 7) that catalyze similar Claisen condensations reactions utilizing AcCoA as a carboxlymethyl donor to a 2-oxo acid substrate. Although these enzymes catalyze similar reactions, their structures and divalent metal specificities are different. The active site of citrate synthase does not contain a divalent metal (3), whereas the 2-oxo acid substrates of malate synthase and α-IPMS coordinate to an active site metal with the proposed metal being Mg(II) in malate synthase and Zn(II) in α-IPMS based on structural studies (5, 7). However, a recent biochemical study on the effects of divalent metals on α-IPMS activity indicates that the enzyme has a broad specificity with Mg(II) and Mn(II) causing the highest activation (8).

Analogous to malate synthase and α-IPMS, HCS possesses a divalent metal that is coordinated by to two histidines, a glutamate residue and a water molecule within the TIM barrel active site of the enzyme. Upon 2-OG binding, the C1 carboxylate and 2-oxo moiety of the substrate also coordinate the active site metal, whereas the α-amine and carboxylate groups of L-lysine coordinate to the metal in feedback inhibition (Figure 3.2) (Chapter 2 and 3). Although this metal is essential for catalysis and L-lysine feedback inhibition, few studies have looked at the metal specificity of HCS. ICP-HRMS analysis of ScHCS determined that the enzyme is most likely Zn(II)-dependent. However, ScHCS treated with a metal chelator can be reactivated with the addition of Mn(II) or Zn(II) (9). Additionally, recent crystal structures of TtHCS have been reported with Mg(II), Cu(II) and Co(II) bound in the active site. Furthermore, the addition of Mg(II), and Mn(II) to EDTA treated TtHCS results in the highest activity of *in vitro*, suggesting one of these may be biologically relevant (10). Collectively, these results suggest a diverse divalent

metal specificity for HCS, yet the biologically relevant metal for this enzyme remains unresolved.

Here we characterize the activity and L-lysine feedback regulation of SpHCS containing a variety of divalent metals. SpHCS purified on IMAC columns charged with Zn(II), Co(II) and Ni(II) incorporated each metal into its active site, whereas SpHCS could only be partially reconstituted with Cu(II). *In vitro* kinetic analysis of these metal-bound forms of the enzymes reveal that both activity and feedback inhibition are metal-dependent, with Zn(II)-SpHCS exhibiting the highest activity and lowest K_i for L-lysine. Additionally, we found that Zn(II) was the dominant metal incorporated *in vivo* in SpHCS recombinantly expressed in *E. coli*, although at 9-18% abundance Together these results suggest that HCS has a broad metal specificity, but *in vivo* HCS may function predominantly as a Zn(II) dependent enzyme.

MATERIALS AND METHODS

Materials

Primers used for the exchange of the 6xHis tag for the Strep-tag II sequence were purchased from Integrated DNA technologies. The divalent metal ions (manganese chloride and copper chloride, zinc sulfate and magnesium chloride) used in the reconstitution of SpHCS and metal inhibition studies were purchased from Sigma. Reagents used in the kinetic studies were prepared as described in Chapters 2 and 3.

Generation of a Strep-tag II SpHCS/pHIS2 Expression Vector

The site-directed, ligase-independent mutagenesis (SLIM) technique (11) was used to remove the 6xHIS tag from SpHCS/pHIS2 and simultaneously insert a Strep-tag II sequence (WSHPQFEK). A set of four primers were designed consisting of: two forward primers that contain the 3' end sequence after the 6xHIS tag with one primer containing a 5' Strep-tag II sequence to replace the 6xHIS tag and two reverse compliment primers of the 5' end before the 6xHIS tag with one primer containing the Strep-tag II sequence (Table A.1). PCR amplification reactions (50 μL) were mixed containing 100 ng SpHCS/pHIS2 DNA, 1 μM of each primer, 1 mM dNTPs (Invitrogen),

Table A.1 Primers used to exchange the 6xHIS tag in SpHCS/pHIS2 for a Strep-II tag.

Primer	Sequence
FORWARD	5’-GATTACGATATCCCAACGACCG-3’
FORWARD STREP	5’-**TGGAGCCACCCGCAGTTCGAAAAG**GATTACGATATCCCAACGACCG-3’
REVERSE	5’-GTAGTACGACATATGTATATCTCC-3’
REVERSE STREP	5’-**CTTTTCGAACTGCGGGTGGCTCCA**GTAGTACGACATATGTATATCTCC -3’

The sequence of the Strep-tag II is bolded.

2 μM $MgSO_4$ (Invitrogen), 1x *Pfx* Amplification buffer, 1x PCRx Enhancer solution, and 3.75 U Platinum® *Pfx* DNA Polymerase (Invitrogen). PCR reactions were denatured for 2 minutes at 95 ^oC followed by 18 rounds of 30 seconds at 95 ^oC, 30 seconds at 50 ^oC, and 11 minutes at 65 ^oC in a thermocycler. Amplification reactions were digested in 1X buffer 4 (1X concentration = 20 mM Tris, pH 7.4, 5 mM $MgCl_2$, 50 mM KCl) with 20 U *Dpn* 1 (Invitrogen) for 1 hour at 37 ^oC. The reaction was quenched with an equal volume of 2X SLIM buffer (50 mM Tris pH 8.8, 300 mM NaCl, 20 mM EDTA) and PCR products were denatured and hybridized by denaturing at 95 ^oC for 2 minutes followed by cooling to 25 ^oC at a rate of 0.2 ^oC/s. Hybridized PCR products were transformed into *E. coli* DH5α cells, plated on LB agar plates containing 100 μg/mL AMP and grown overnight at 37 ^oC. DNA from the resulting colonies was isolated utilizing a QIAprep Spin Miniprep kit (Qiagen) and dideoxynucleotide sequencing was performed (University of Michigan DNA Sequencing Core) to verify the sequence exchange.

Expression and Purification of Strep-tag II SpHCS

Expression of Strep-tag II SpHCS was preformed as described for SpHCS/pHIS2 in Chapter 2, with the exception that in one case, 100 μM Zn acetate (ZnAc) was added to the cells during growth. Cell pellets were thawed and lysed with the addition of 5 mg lysozyme and rocking at room temperature for 1 hour, followed by either sonication in a glass beaker (Prep 1 and 2) or by three freeze cycles with homogenization (Prep 3 and ZnAc prep). After the addition of 30 ml of 50 mM sodium phosphate, pH 7.0, and 5 mM βme; and the insoluble material was separated form the soluble enzyme by centrifugation at 15,000 rpm for 20 minutes in a Sorvall SS-34 rotor. The soluble enzyme was loaded onto a Strep•Tactin® superflow™ Agarose column (Novagen) that had been regenerated with 1X regeneration buffer (100 mM Tris-HCl pH 8.0, 150 mM NaCl, 1 mM EDTA, and 1 mM hydroxy-azophenyl-benzoic acid (HABA)) and pre-equilibrated with 50 mM sodium phosphate, pH 7.0, 250 mM NaCl, and 5 mM βme. Strep-tag II SpHCS was eluted with a step gradient of 50 mM sodium phosphate pH 7.0, 250 mM NaCl, 2.5 mM desthiobiotin, and 5 mM βme, and the peak fractions were pooled and the Strep tag II sequence was removed by TEV protease during dialysis overnight in 50 mM sodium phosphate pH 8.0, 150 mM NaCl and 5 mM β-me. Cleaved SpHCS was further purified

by loading onto a Superdex 200 (Amersham Biosciences) gel filtration column and isocratically eluting with 25 mM Tris pH 9.0, 50 mM NaCl, and 1 mM TCEP. Peak fractions were judged to be essentially pure by SDS-PAGE and were concentrated to 30-60 mg/mL. Concentrated SpHCS was flash frozen and stored at -80 ^{o}C.

Incorporation of Divalent Metals into the Active Site of SpHCS

To incorporate several different divalent cation metals, including Co(II), Ni(II), Zn(II), Mn(II) and Cu(II) into SpHCS we either purified SpHCS on different metal affinity columns or reconstituted apo-enzyme with the appropriate metal. The Talon (Clonetech) Co(II) resin, Ni(II) sepharose™ high performance (GE Healthcare) resin and Zn(II) charged IMAC sepharose (GE Healthcare) resin columns were used to purify SpHCS to incorporate Co(II), Ni(II) and Zn(II), respectively. Because SpHCS could not be purified on Mn(II) or Cu(II) charged IMAC sepharose, we had to incorporate Mn(II) and Cu(II) into the active site of SpHCS after the first steps of purification. SpHCS was purified on either Talon Co(II) resin or Zn(II) IMAC resin followed TEV cleavage and removal of the 6xHIS tag via batch binding as previously described (Chapter 2). The enzyme was treated with 10 mM EDTA for 10 minutes followed by dialysis in 50 mM HEPES pH 8.0, 50 mM NaCl, 10 mM EDTA, 1 mM dipicilinic acid, and 0.05% (w/v) Chelex® 100 resin (Bio-rad) for 2 hours at 4 ^{o}C to remove any traces of metal. The enzyme was then dialyzed two times in 4 L of re-equilibration buffer (50 mM HEPES pH 8.0 and 50 mM NaCl) for 3 hours each at 4 ^{o}C to remove the metal chelating agents. SpHCS was then incubated with either 2 mM $MnCl_2$ or $CuCl_2$ for 15 minutes and concentrated to 2 mL using an 30k Amicon Ultra centrifugal Filter Device (Millipore). SpHCS reconstituted with each of the different divalent metals was further purified on a Superdex 200 (Amersham Biosciences) gel filtration column, concentrated to 30-60 mg/ml, flash-frozen and stored as described in Chapter 2.

Inductively Coupled Plasma-High Resolution Mass Spectroscopy

WT SpHCS purified on Zn(II), Co(II) (Talon) and Ni(II) charged IMAC sepharose resin, SpHCS reconstituted with Mn(II) or Cu(II) and SpHCS purified on Strep•Tactin® superflow™ Agarose were diluted to 20 μM in 50 mM HEPES, pH 7.5.

Metal content was analyzed using ICP-HRMS (University of Michigan, Department of Geology,) with the protein buffer used as a control as described in Chapter 2.

Kinetic Studies

Steady state kinetic parameters were determined for WT Strep-tag II purified SpHCS and SpHCS incorporated with the various divalent metal ions as described using a fluorescent HCS assay for the Zn(II)-purified WT SpHCS (Chapter 2). Briefly, HCS assays were carried out in triplicate at room temperature in 100mM HEPES, pH 7.5 using 10-30 nM enzyme and variable concentrations of 2-OG and AcCoA, up to 5 mM and 200 μM, respectively. The equilibrium inhibition constant (K_i) values for SpHCS incorporated with Co(II), Ni(II) and Cu(II) versus the substrate 2-OG were calculated using that same fluorescent HCS assay as described in Chapter 3. Briefly, initial velocities were measured in triplicate at 2-OG concentrations of 0.66-2.0 mM at various fixed concentrations of L-lysine 0-150 μM for with AcCoA held constant at 100 μM. Using Prism (Graphpad Software), data was fit to the non-linear Michaelis-Menten regressions in for a competitive inhibitor to calculate K_i values.

RESULTS

Metal Content of SpHCS Incorporated with Different Divalent Metal Ions

During our structural studies, we discovered that SpHCS free enzyme crystallized with Co(II), which was presumably introduced during the Co(II) IMAC purification steps (Chapter 2). To the metal specificity of this enzyme, SpHCS containing a 6xHIS tag was recombinantly expressed in *E. coli* and purified using three different IMAC columns charged with Zn(II), Co(II) or Ni(II). The metal content of the purified protein was then determined by ICP-HRMS. Analysis of this data illustrates that the Zn(II)-purified SpHCS contained 86% Zn(II) with trace amounts of Cu(II), Mn(II) and Fe(II), the Co(II)-purified SpHCS was incorporated with 84% Cu(II) and 5% Zn(II) and the Ni(II)-purified SpHCS possessed 72% Ni(II) and 4% Zn(II) (Table A.2). Because the Zn(II)-purified enzyme contained trace amounts of Mn(II) and Cu(II), we sought to incorporate SpHCS with these metals, but were unable to accomplish this addition using

Table A.2 *In vitro* metal content of IMAC purified and reconstituted SpHCS and *in vivo* metal content of Strep-tag II purified SpHCS expressed recombinantly in *E. coli*.

	Purification Column									
	Zn(II)	**Co(II)**	**Ni(II)**	**Metal Free**	**Cu(II) RC**	**Mn(II) RC**	**Strep-tag 1**	**Strep-tag 2**	**Strep-tag 3**	**Strep-tag ZnAc[a]**
Metal Content (%)[b]										
Mn(II)	0.1[c]	0	0	0	0	0.6	0.1	0.2	0	0
Fe(II)	1.3 ± 0.1	1.1	0	0	0	0	0	0.1	0.4	0
Co(II)	0	84.0 ± 4.0	0	0	0.7	0.5 ± 0.1	0.1 ± 0.1	0	0	0
Ni(II)	0	0	72.3 ± 1.3	0.5 ± 0.1	0	0	0.4	0.7 ± 0.1	0.5 ± 0.1	1.2 ± 0.1
Cu(II)	0.4	1.3	0.3 ± 0.1	1.3± 0.`	53.3 ± 2.4	0	1.5 ± 0.1	0.8	2.5 ± 0.1	1.1 ± 0.1
Zn(II)	84.1± 4.3	5.3 ± 0.3	4.3 ± 0.5	2.8 ± 0.2	0	1.8 ± 0.1	16.1 ± 0.8	7.1± 0.2	9.9 ± 0.5	11.6 ± 0.6
Total Metal Bound	85.9 ± 4.3	91.7± 4.3	76.9 ± 1.4	4.6 ± 0.2	54.0 ± 2.4	2.9 ± 0.2	18.2 ± 0.8	8.9 ± 0.2	13.3 ± 0.5	13.9 ± 0.6

[a] 100 μM Zn acetate was added to cells during growth.
[b] Metal content is expressed as a percentage of mol metal/mol SpHCS monomer after subtracting trace amounts of metal in the buffer.
[c] Errors were not reported if they were <0.05%.

conventional IMAC columns. Therefore, Mn(II) and Cu(II) were incorporated into SpHCS after the first steps of IMAC purification and removal of the metal bound during purification. ICP-HRMS analysis of SpHCS treated with chelating agents demonstrated that only a small amount of remaining metal remained (totaling 4.6%) indicating that this protocol effectively eliminates the metal incorporated during IMAC purification (Table A.2). SpHCS reconstituted with Cu(II) contained 54% Cu(II) with a trace amount of Co(II), whereas SpHCS was unable to bind Mn(II) according to our ICP-HRMS results. Consistent with our structural data (Chapter 2 and 3), which illustrates one active site divalent metal per SpHCS monomer, incorporation of divalent metals into SpHCS during IMAC purification resulted in approximately the same 1:1 ratio for the Zn(II), Ni(II) and Cu(II) purified enzymes. However, full reconstitution of SpHCS with Cu(II) could not be achieved, which may indicate that the metal binding site has a low affinity that cannot be fully incorporated during non-column reconstitution. In summary, our results reveal that SpHCS has the ability to bind several different divalent metals *in vitro.*

Kinetic Analysis of SpHCS Incorporated with Various Divalent Metals

We next tested the effect different divalent metals have on the steady state kinetics parameters and equilibrium inhibition constant (K_i) for the each of the metal-SpHCS complexes. SpHCS reconstituted with Zn(II), Co(II), Ni(II) and Cu(II) exhibited similar K_M values for both 2-OG and AcCoA which ranged from 120-209 mM and 5.0-10.7 μM, respectively (Figure A.1A, A.1B and Table A.3). However, the turnover rate of SpHCS appears to be dependent on the metal content with the observed trend in k_{cat} values as follows: Zn(II) > Cu(II) >Co(II) > Ni(II). Although the k_{cat} value for Co(II) was modestly higher than the k_{cat} value for Cu(II), we predict that a larger incorporation of Cu(II) into the reconstituted enzyme would result in an increased turnover rate. Additionally, the incorporation of Ni(II) into SpHCS was modestly lower than that of Zn(II) and Cu(II) indicating that it may also have a higher expected k_{cat} value. Alternatively, Ni(II)-SpHCS may actually be inactive as this enzyme retained 4.3% Zn(II) and exhibited similar activity to metal free SpHCS, which contains 4.6% metal (Table A.2 and Table A.3).

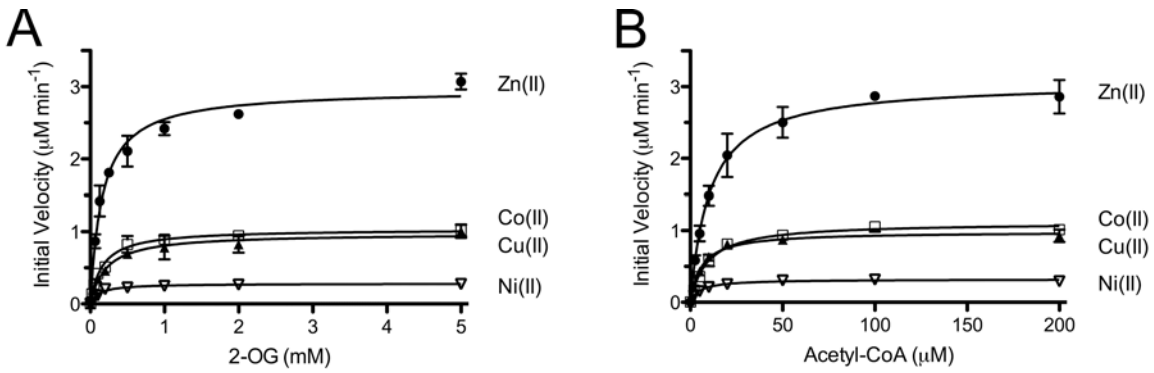

Figure A.1 *In vitro* activity of the metal-SpHCS complexes. (A and B) Michaelis-Menten plot of the initial velocity versus 2-OG concentration **(A)** and AcCoA concentration **(B)** for the formation of homocitrate catalyzed by metal-SpHCS complexes. Data points are the average of triplicate measurements, and the error bars represent one standard deviation.

Table A.3 Kinetic analysis of Strep-II tag purified and metal substituted HCS.

	K_M 2-OG	K_M AcCoA	k_{cat}[a]	K_i L-lysine vs. 2-OG
	mM	μM	min^{-1}	μM
Zn(II)[b]	159 ± 15	10.7 ± 0.6	303 ± 4	3.6 ± 0.7
Co(II)	155 ± 18	9.2 ± 1.0	107 ± 2	62.7 ± 7.1
Ni(II)	120 ± 2.4	5.0 ± 0.5	30.2 ± 0.8	14.3 ± 1.5
Cu(II)	209 ± 31	6.0 ± 0.5	98.0 ± 2.2	6.0 ± 0.5
Metal Free	N.D	N.D	33.1 ± 1.8[c]	N.D
Strep 1	486 ± 112	7.0 ± 0.7	180 ± 6	N.D
Strep 2	173 ± 17	11.0 ± 1.0	95.0 ± 2	N.D
Strep 3	366 ± 53	7.8 ± 0.67	111 ± 3	N.D
Strep ZnAc	385 ± 52	8.8 ± 1.0	115 ± 3	N.D

[a] Average of the individual k_{cat} values determined for each substrate.
[b] Steady state kinetic parameters and inhibition constant are previously reported (Chapters 2 and 3).
[c] Estimated form initial velocity using 100 nM SpHCs and saturating substrate concentrations.
N.D. not determined.

To examine whether the different metals affect L-lysine feedback inhibition, we determined K_i values for the Zn(II), Co(II), Ni(II) and Cu(II) incorporated forms of SpHCS by measuring the initial velocity of the reactions for L-lysine inhibition versus 2-OG. As expected, the double reciprocal plots of velocity versus substrate concentration illustrate that L-lysine is a competitive inhibitor versus 2-OG for each metal complex (Chapter 3) (Figure A.2). L-lysine completely inhibited each Me(II)-SpHCS complex with measured K_i values corresponded to the following trend: Zn(II)- and Cu(II)-SpHCS bound with the highest affinities (3.6 ± 0.7 μM and 6.0 ± 0.5 μM, respectively), followed by Ni(II)-SpHCS (14.3 ± 1.5) and Co(II)-SpHCS (62.7 ± 7.1) (Table A.3). The K_i value for Co(II)-SpHCS is >17-fold higher that that of Zn(II)-SpHCS, indicating a difference in the active site environment or unfavorable coordination of L-lysine to Co(II).

Identification and Functional Analysis of the *in vivo* Metal Content of SpHCS

Our *in vitro* results suggest that SpHCS may bind and utilize different divalent metal ions *in vivo* during catalysis. To investigate this possibility, we determined the metal content of SpHCS expressed recombinantly in *E. coli*, using a Strep-tag II/SpHCS vector that was engineered to avoid incorporation of metals during purification of a 6xHis tagged SpHCS construct during the IMAC purification steps. ICP-HRMS analysis of four different Strep-tag II SpHCS purifications revealed that *in vivo* metal content varied between purifications and consisted of a heterogeneous mixture of transition state metals, including Zn(II), Cu(II), Ni(II) and trace amounts of Co(II), Mn(II) and Fe(II) (Table A.2). In all four purifications, Zn(II) was the most abundant metal followed by Cu(II). Additionally, the inclusion of Zn(II) acetate during cell growth did not increase the Zn(II) content in the purified SpHCS. This result is not surprising considering that the balance between Zn(II) uptake and efflux has a small tolerance range in *E. coli* (12), suggesting that no pool of free zinc exists in the cytosol under normal growth conditions. In contrast to the relatively high percentage of metal incorporation into SpHCS *in vitro,* the percentage of metal bound to the Strep-tag II SpHCS monomer ranged form 9-18% (Table A.2). Lower incorporation levels may be caused by the high level of expression of the recombinant SpHCS in *E. coli*, in conjunction with a high metal binding constant and a limited amount of free zinc or potentially other metals in the cells.

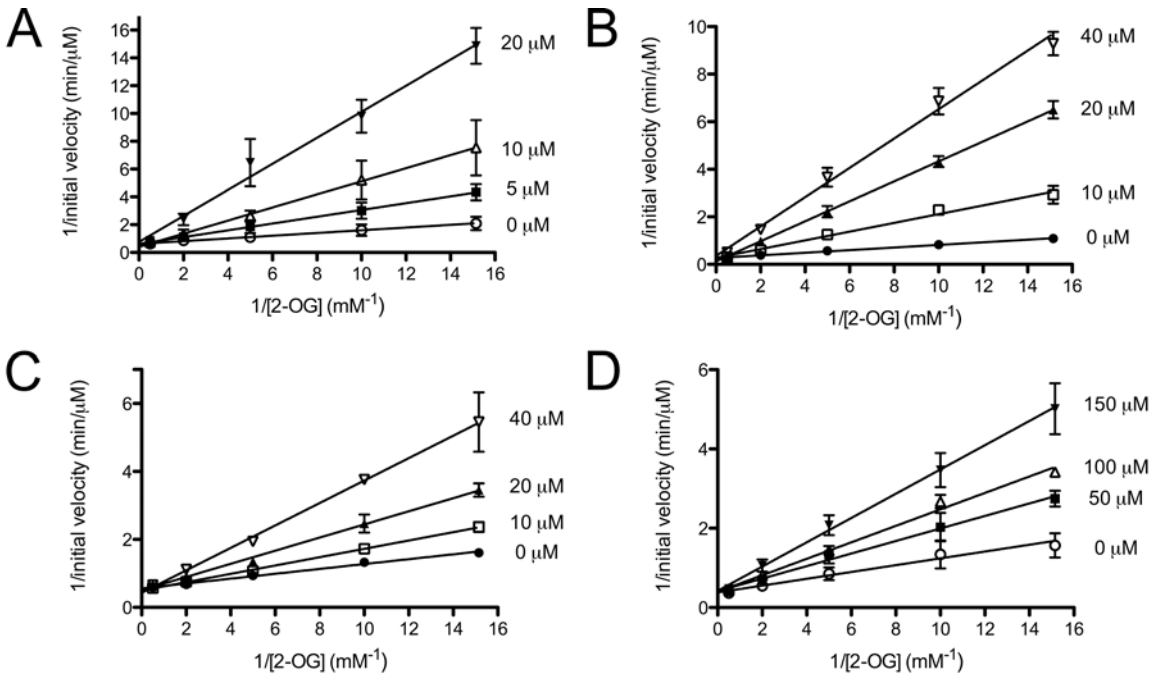

Figure A.2 L-lysine inhibition of SpHCS metal complexes. Double reciprocal plots of initial velocity versus 2-OG concentration at different concentrations of L-lysine and a fixed saturating concentration of AcCoA for Zn(II)-SpHCS **(A)**, Cu(II)-SpHCS **(B)**, Ni(II)-SpHCS **(C)** and Co(II)-SpHCS **(D)**. Data points are the average of triplicate measurements, and the error bars represent one standard deviation.

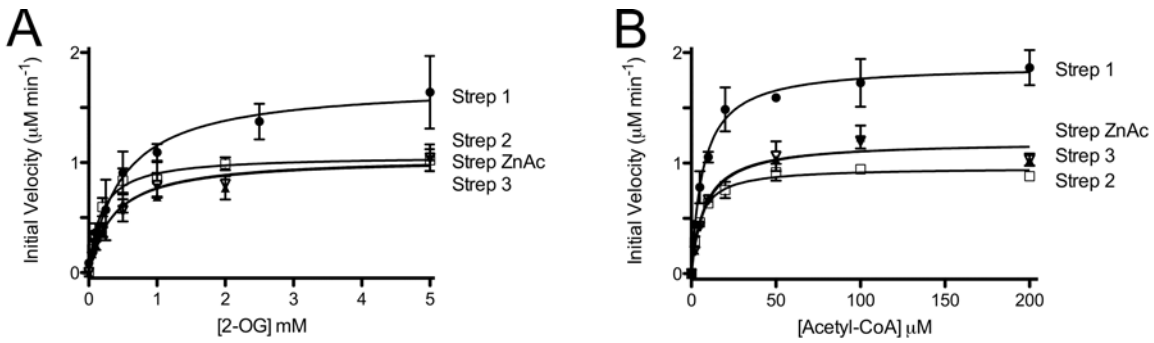

Figure A.3 *In vitro* activity of Strep-tag II purified SpHCS. (A and B) Michaelis-Menten plot of the initial velocity versus 2-OG concentration **(A)** and AcCoA concentration **(B)** for the formation of homocitrate catalyzed by Strep-II tag purified enzyme. Data points are the average of triplicate measurements, and the error bars represent one standard deviation.

After determining the *in vivo* metal content of SpHCS expressed in *E. coli*, we next investigated the activity of the enzyme by measuring the steady state parameters of each Strep-II tag purification (Figure A.2A and A.2B). The K_M values for 2-OG and AcCoA form these purifications ranged from 173-528 mM and 6.9-11.0 μM, respectively, and are similar to the SpHCS reconstituted with different divalent metals (Table A.3). In addition, the k_{cat} values for the four Strep-II tag SpHCS purifications ranged from 95-184 min^{-1} with the rates being proportional to the total metal content of the enzyme (Table 4.1 and Table 4.3). Interestingly, the Strep-II tag SpHCS exhibited a disproportionately high turnover rate (k_{cat} =184 min^{-1} for 18.2% metal incorporation) compared to the almost fully incorporated Zn(II)-IMAC purified enzyme (k_{cat} =303 min^{-1} for 86% metal incorporation) (Table A.1and A.3). This discrepancy might be explained by the different purification protocols where exposure of SpHCS to the IMAC column may alter the enzyme's activity. Further studies are needed to determine if this is the case. In summary, SpHCS expressed recombinantly in *E. coli* contains a variety of metals, the majority of which is Zn(II), with the turnover rate of the enzyme being proportional to the metal content.

DISCUSSION

Divalent Metal Specificity on the Activity and Regulation of SpHCS

Although HCS has been shown to be a metalloenzyme through biochemical and crystallographic studies (9, 10), little is known about the metal ion requirement for HCS activity. Additionally, no detailed studies have looked at the *in vivo* metal content or the dependence of HCS regulation in relation to bound divalent metal. In this work, our biochemical studies indicate that SpHCS can bind and utilize a variety of divalent metal ions, with Zn(II)-SpHCS displaying the highest turnover rate followed by Cu(II), Co(II) and Ni(II) (Table A.3), indicating that Zn(II) may be the biologically relevant metal cofactor. This result is in agreement with the assignment of Zn(II) in ScHCS (9), but contrast with the results found for the TtHCS enzyme (10). Okada *et al* found that the addition of Mg(II) and Mn(II) to TtHCS caused the greatest activation of this enzyme with reported specific activities of 41.5 and 39.5 mU/mg protein. However, when

converted to k_{cat} values, these specific activities correspond to only ~4 % of the k_{cat} of TtHCS purified on a Ni(II)-IMAC column, suggesting the metals tested may not have been fully incorporated during the assays. We also observed this phenomenon when assaying metal free SpHCS in the addition of divalent metals (data not shown), but were able to circumvent this problem by nearly fully incorporating each divalent metal during IMAC purification. Our findings also show that Zn(II)-SpHCS exhibited the highest affinity towards the feedback inhibitor L-lysine closely followed by Cu(II) and Ni(II). The K_i value for Co(II)-SpHCS was moderately higher that those for the other metals. However, the variation in the K_i values among the different metal-bound enzymes is relatively modest when compared to the substantial increase in K_i values and insensitivity to AEC seen for SpHCS L-lysine interacting mutants, particularly for the D123N mutant (Chapter 3). This suggests that *in vivo*, the active site divalent metal identity may only have a small effect on the regulation of the metabolic flux through the AAA pathway.

In vivo metal content of SpHCS expressed in *E. coli*

An analysis of the metal content and catalytic activity of Strep-tag II purified SpHCS which was recombinantly overexpressed in *E. coli* provides insights into the metal dependence of SpHCS *in vivo*. Consistent with our *in vitro* results, Zn(II) was the dominant metal bound to SpHCS, suggesting that this may be the biologically relevant metal that this ion. However, because the overall incorporation of metal was quite low it may also be possible that this enzyme binds and utilizes another metal ion such as Fe(II). Many Fe(II) dependent enzymes, including peptide deformylase (13), γ-carbonic anhydrase (14), S-Ribosylhomocysteinase LuxS (15) and the histone deacetylase HDAC8 (16) were originally characterized as Zn(II) metalloenzymes because of the oxidation of Fe(II) to Fe(III) and metal exchange during aerobic purification. Future studies are needed to determine if HCS can also bind and utilize Fe(II).

Comparison of the Divalent Metal Specificity of HCS to α-IPMS and Malate Synthase

Although the active sites of HCS and α-IPMS are structurally similar and have nearly identical metal binding configurations (Chapter 2 see Figure 2.4), the divalent

metal specificities of these two enzymes appear to be different. These differences are in part due to the identity of the active site ligands that coordinate the metal ion. Based on size and charges, metal are classified as “hard”, “soft” or “borderline” (17) (Table A.4). Additionally, metals considered “hard” or “soft” tend to strongly prefer “hard” or “soft” ligands respectively, with borderline metals coordinating to both classes of ligands (18, 19) (Table A.4). For example, the catalytic core of malate synthase contains all “hard” ligands including the carboxylate oxygen of an aspartate and a glutamate, two water molecules and the C1 and 2-oxo group of its substrate glyoxylate that forms an octahedral coordination to a “hard” Mg(II) ion (Figure 1.3B) (5). Similar to malate synthase, biochemical studies on metal free α-IPMS free indicate that addition a “hard” metal, either Mg(II) and Mn(II) ion the produce the highest activation of the enzyme *in vitro* (8). This result is somewhat surprising considering that two of the coordinating ligands in α-IPMS are “soft” nitrogen atoms in the imidazole rings of a histidine residues (Figure 2.4B) that do not tend to coordinate the “hard” Mg(II) and Mn(II) ions. Although, in certain cases Mn(II) has been reported to bind the nitrogen atoms of histidine imidazole groups (20), and thus this may be the biologically relevant metal in α-IPMS. In contrast with these findings, we were unable to reconstitute SpHCS, with the “hard” metal Mn(II), but found that the enzyme readily incorporated with the “borderline” metals, Co(II), Cu(II), Ni(II) and Zn(II). These metals tend to coordinate to both hard and soft ligands. In addition, assignment of a “borderline” metal to the active site of HCS is consistent with the finding that the substrate 2-OG and inhibitor L-lysine both coordinate to the metal, despite the differences in their coordination groups (Figure 3.2). In summary, although HCS, α-IPMS and malate synthase catalyze analogous Claisen condensation reactions, the divergence in their structures and metal dependence provide insights into the evolution of catalysis and regulation of these enzymes.

Importance of the Metal in Identifying Antifungal Inhibitors to HCS

HCS has been proposed as an antifungal target because it is absent in humans and is an important part of the AAA pathway as the committed step in the pathway and is highly regulated through L-lysine feedback inhibition. Our characterization of the divalent metal specificity of SpHCS reveals that the enzyme can bind and utilize a variety

Table A.4 Classification of hard and soft metals and ligands.

METALS[a]		
Hard	**Borderline**	**Soft**
Ca(II)	Co(II)	Cd(II)
Mg(II)	Cu(II)	Pt(II)
Mn(II)	Fe(II)	
	Ni(II)	
	Zn(II)	

PROTEIN LIGANDS[b]	
Hard	**Soft**
Aspartate carboxylate oxygen	Histidine imidazole nitrogen
Glutamate carboxylate oxygen	Cysteine sulfur
Asparagine carboxamide oxygen	
Glutamine carboxamide oxygen	
Solvent	

[a]From reference 17.
[b]From references 18 and 19.

of metals, and that the identity of the metal can contribute to the affinity of inhibitor binding, with L-lysine binding more weakly to Co(II)-SpHCS. Knowledge of the divalent metal that is bound to HCS *in vivo* may allow for a more accurate prediction of the potency of small molecule inhibitors which inactivate SpHCS through interaction with the active site metal.

FUTURE DIRECTIONS

Although informative, the metal specificity studies in Chapter 4 only begin to elucidate the metal requirements of HCS. Our studies indicate that Zn(II) might be the biological divalent metal, however it is also possible that HCS is a Fe(II) dependent enzyme. ICP-HRMS analysis of Strep-tag II SpHCS purified anaerobically is needed to determine if Fe(II) is also bound to SpHCS *in vivo*. Additionally, it proved difficult to reconstitute metal free SpHCS with divalent metals before assaying for activity, indicating that SpHCS may have a low affinity for metal binding. To examine this possibility, metal binding studies are needed to determine the affinity of SpHCS for different divalent metal ions. Furthermore, while designing a secondary HTS to eliminate small metal chelators (Chapter 4), we found that excess Mn(II) inhibits SpHCS activity. Based on the crystal structure of the free enzyme, where a Mg(II) ion is coordinated to a glutamate residue and five water molecules (Figure 3.1C), we can speculate that the mechanism of metal inhibition may occur through this binding position. However future studies are still needed to determine if other divalent metals inhibit SpHCS, and if this is the mechanism of inhibition. Finally, experiments are still needed to establish the metal content of HCS from yeast under normal and stressed growing conditions. Not only will these experiment allow for the determination of the true biological metal, but they may also provide insights into whether HCS undergoes metal switching *in vivo*, similar to the proposed mechanism of HDAC8 and LpxC (16, 21). If metal switching does occur in HCS, this mechanism may further regulate the enzymes function and thus the metabolic flux through the AAA pathway.

ACKNOWLEDGEMENTS

I wish to thank Ted Huston for performing the ICP-HRMS analysis.

REFERENCES

1. Karpusas, M., Branchaud, B., and Remington, S. J. (1990) Proposed mechanism for the condensation reaction of citrate synthase: 1.9-A structure of the ternary complex with oxaloacetate and carboxymethyl coenzyme A, *Biochemistry 29*, 2213-2219.

2. Wiegand, G., Remington, S., Deisenhofer, J., and Huber, R. (1984) Crystal structure analysis and molecular model of a complex of citrate synthase with oxaloacetate and S-acetonyl-coenzyme A, *J. Mol. Biol. 174*, 205-219.

3. Wiegand, G., and Remington, S. J. (1986) Citrate synthase: structure, control, and mechanism, *Annu. Rev. Biophys. Biophys. Chem. 15*, 97-117.

4. Anstrom, D. M., Kallio, K., and Remington, S. J. (2003) Structure of the Escherichia coli malate synthase G:pyruvate:acetyl-coenzyme A abortive ternary complex at 1.95 A resolution, *Protein Sci. 12*, 1822-1832.

5. Howard, B. R., Endrizzi, J. A., and Remington, S. J. (2000) Crystal structure of Escherichia coli malate synthase G complexed with magnesium and glyoxylate at 2.0 A resolution: mechanistic implications, *Biochemistry 39*, 3156-3168.

6. de Carvalho, L. P., and Blanchard, J. S. (2006) Kinetic and chemical mechanism of alpha-isopropylmalate synthase from Mycobacterium tuberculosis, *Biochemistry 45*, 8988-8999.

7. Koon, N., Squire, C. J., and Baker, E. N. (2004) Crystal structure of LeuA from Mycobacterium tuberculosis, a key enzyme in leucine biosynthesis, *Proc. Natl. Acad. Sci. U.S.A. 101*, 8295-8300.

8. de Carvalho, L. P., and Blanchard, J. S. (2006) Kinetic analysis of the effects of monovalent cations and divalent metals on the activity of Mycobacterium tuberculosis alpha-isopropylmalate synthase, *Arch. Biochem. Biophys. 451*, 141-148.

9. Qian, J., West, A. H., and Cook, P. F. (2006) Acid-base chemical mechanism of homocitrate synthase from Saccharomyces cerevisiae, *Biochemistry 45*, 12136-12143.

10. Okada, T., Tomita, T., Wulandari, A. P., Kuzuyama, T., and Nishiyama, M. (2009) Mechanism of substrate recognition and insight into feedback inhibition of homocitrate synthase from thermus thermophilus, *J. Biol. Chem.*

11. Chiu, J., March, P. E., Lee, R., and Tillett, D. (2004) Site-directed, Ligase-Independent Mutagenesis (SLIM): a single-tube methodology approaching 100% efficiency in 4 h, *Nucleic Acids Res. 32*, e174.

12. Outten, C. E., and O'Halloran, T. V. (2001) Femtomolar sensitivity of metalloregulatory proteins controlling zinc homeostasis, *Science 292*, 2488-2492.

13. Rajagopalan, P. T., and Pei, D. (1998) Oxygen-mediated inactivation of peptide deformylase, *J. Biol. Chem. 273*, 22305-22310.

14. Tripp, B. C., Bell, C. B., 3rd, Cruz, F., Krebs, C., and Ferry, J. G. (2004) A role for iron in an ancient carbonic anhydrase, *J. Biol. Chem. 279*, 6683-6687.

15. Zhu, J., Dizin, E., Hu, X., Wavreille, A. S., Park, J., and Pei, D. (2003) S-Ribosylhomocysteinase (LuxS) is a mononuclear iron protein, *Biochemistry 42*, 4717-4726.

16. Gantt, S. L., Gattis, S. G., and Fierke, C. A. (2006) Catalytic activity and inhibition of human histone deacetylase 8 is dependent on the identity of the active site metal ion, *Biochemistry 45*, 6170-6178.

17. Pearson, R. G. (1963) Human Factors Aspects of Lightplane Safety. Rep 63-35, *Rep Civ Aeromed Res Inst US*, 1-13.

18. Glusker, J. P. (1991) Structural aspects of metal liganding to functional groups in proteins, *Adv Protein Chem 42*, 1-76.

19. Christianson, D. W., and Cox, J. D. (1999) Catalysis by metal-activated hydroxide in zinc and manganese metalloenzymes, *Annu Rev Biochem 68*, 33-57.

20. Christianson, D. W. (1997) Structural chemistry and biology of manganese metalloenzymes, *Prog Biophys Mol Biol 67*, 217-252.

21. Hernick, M., and Fierke, C. A. (2006) Molecular recognition by Escherichia coli UDP-3-O-(R-3-hydroxymyristoyl)-N-acetylglucosamine deacetylase is modulated by bound metal ions, *Biochemistry 45*, 14573-14581.

APPENDIX B
PURIFICATION OF *CANDIDA ALBICANS* HCS LYS212

Candida albicans HCS (CaHCS) was cloned, overexpressed and purified on a Co(II) Talon IMAC column as described for SpHCS (Chapter 2) (Figure B.1). We also determined the steady state kinetic parameters of CaHCS Lys212 ($K_{m(2\text{-}OG)}$ = 99 ± 19 μM, $K_{m(AcCoA)}$ = 3.6 ± 0.5 μM and k_{cat} =124 ± 2.8) and found them to be similar to Co(II)-SpHCS (Table A.2).

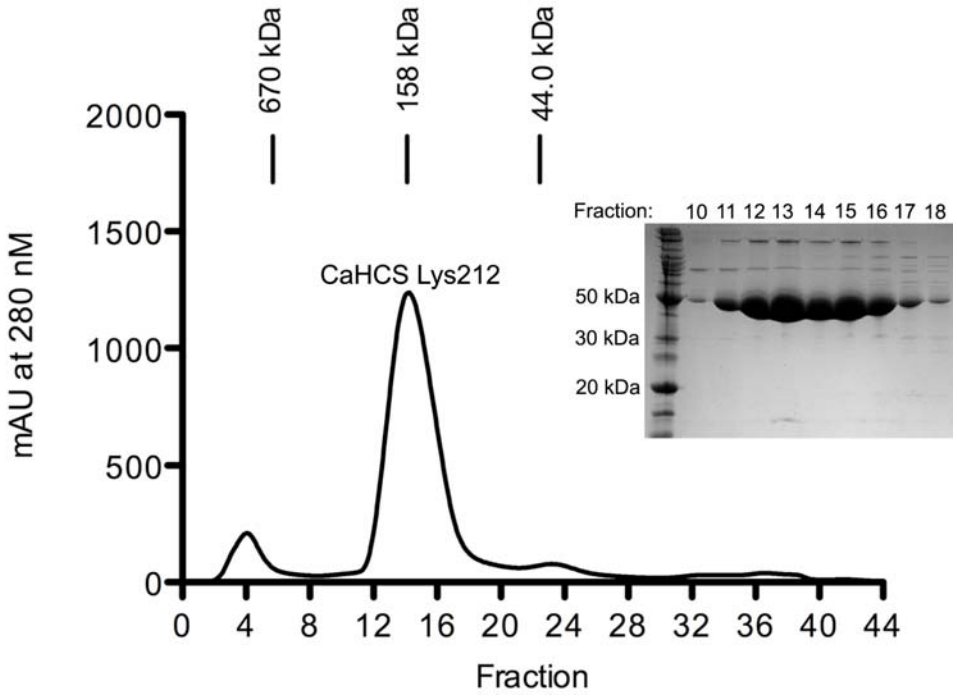

Figure 6.2 Gel filtration purification of CaHCS Lys212. A chromatogram depicting the elution profile of the enzyme on a Superdex 200 gel filtration column with molecular weight standards shown above the chromatogram. The inset panel illustrates the Coomassie staining of an SDS-PAGE gel of the peak fractions from this purification.